A Tunable High-Static-Low-Dynamic-Stiffness Isolator

And

A Fuzzy-Neural Network Based Active Control Isolator

By

Naibiao Zhou

A thesis presented to Lakehead University in partial fulfillment of the requirement

for the degree of Master of Science

in

Control Engineering

Thunder Bay, Ontario, Canada, 2009

Abstract

Excessive vibration can be detrimental to a wide variety of structures and machines. Vibration isolation is an effective means to suppress vibration. This study focuses on development of some new techniques to improve performance of vibration isolators. The thesis consists of two parts. In the first part, a novel vibration isolator is developed. In the second part, an adaptive fuzzy-neural network (FNN) controller is applied to active isolators.

The developed isolator possesses the characteristics of high-static-low-dynamic stiffness (HSLDS) and can act passively or semi-actively. The HSLDS property of the proposed isolator is obtained by connecting a mechanical spring, in parallel with a negative spring which is produced by a pair of electromagnets (EM) and a permanent magnet (PM) in attracting configuration. The isolator spring is composed of three parts: mechanical spring, the PM spring, and the EM spring. The characterization study intends to determine the stiffness of each of these springs. Due to the highly nonlinearity of the system, an experimental approach is taken. The mechanical spring used is a steel beam that demonstrates a nonlinear hardening effect. Both the PM spring and EM spring possess negative stiffness. The PM stiffness can be varied by adjusting the gap distance between the PM and the EMs while the EM stiffness can be varied by tuning the current to the EMs. With the determined stiffness relationships, the study explores how a combination of the mechanical spring and the PM spring can reduce the hardening effect, thus the natural frequency of the isolator. The study demonstrates that adding both the PM and EM springs to the isolator can result in a quasi-zero-stiffness (QZS). A computer simulation is conducted to find the displacement transmissibility of the isolator and the jump frequencies for different settings.

A commercial software package, Comsol Multiphysis, is employed to characterize the isolator as well. First, single physics simulations are conducted to determine the stiffness for each spring. Then, multi-physics simulations are conducted to determine the stiffness for the combined system. Finally, a base excitation is simulated to determine the displacement transmissibility of the isolator.

Experimental studies are conducted to investigate the effectiveness of the isolator. First the natural frequencies of the isolator are determined for different configurations. Then the relationship of the displacement transmissibility vs. the exciting frequency is measured against different setups. Finally, the on-line tuning capability of the isolator is investigated.

The proposed electromagnetic isolator can be used as an active isolator by properly choosing the polarities of the two electromagnets. To control such a system that is highly nonlinear and has unknown parameters, an adaptive fuzzy-neural network (FNN) control algorithm is used. First some background information is reviewed. Then the adaptive FNN controller design procedure is presented. Finally, numerical simulations are employed to compare the adaptive FNN controller with the three other controllers: Proportional-Plus-Derivative, Backstepping, and Adaptive Backstepping.

Acknowledgements

Contents

List of Figures

vii

List of Tables

List of Symbols and Abbreviations

ER	Electrorheological
EM	Electromagnet with steel core inside
FNN	Fuzzy-neural network
HSLDS	High-static-low-dynamic-stiffness
MR	Magnetorheological
PM	Permanent magnet
QZS	Quasi-zero stiffness
r.m.s	Root-mean-square
SDOF	Single-degree-of-freedom
T.R.	Transmissibility ratio
$\cdot$	Differentiation with respect to time
$\cdot\cdot$	Second order differentiation with respect to time
α	Coefficient in the equation to calculate the interaction force between the PM and the steel core
γ	Ratio of the total flux to the gap flux
μ_0	Permeability of free space
μ_r	The relative permeability of the steel core
σ	Surface pole density
ω_b	Excitation frequency

ω_n	Natural frequency of the isolator
ζ	Damping ratio
a	Radius of a single current loop
A	Area of the PM surface
B_d	Magnetic flux density on the central axis at d distance from the PM face
c	Damping coefficient
C	Magnetic permeability of the medium
C_m	Coefficient in the Coulomb's law
d	Distance between two objects
D	Gap distance between the two steel cores
F_b	Restoring force generated by the beam
F_{pc}	Interaction force between the PM and the steel core
F_{pe}	Sum of the interaction force between the PM and the steel core, and the interaction force between the PM and the electromagnet coil.
F_{pf}	Interaction force between the electromagnet coil and the PM
F_r	Restoring force acting on the PM
h	Thickness of the permanent magnet
J_0	Magnitude of the current density
k	Stiffness of the isolator
k_{pc}	Stiffness of the permanent magnet spring
k_{pe}	Stiffness of the electromagnet spring

K_d	Derivative gain
K_p	Proportional gain
l	Length of the permanent magnet
l_{em}	Length of the electromagnet coils
l_s	Length of the steel core
m	Mass
M	Magnetization of the PM
N	Turns of the coils
p	Pole strength of a magnet
r_1	Inner radius of the electromagnetic coils
r_2	Outer radius of the electromagnet coils
R	Resistance of the coil
r	Frequency ratio
w	Width of the permanent magnet
x	Absolute displacement of the PM
x_r	Reference signal
y	Base motion
z	Displacement of the PM relative to the base
z_1	Tracking error
z_2	Difference between relative velocity of the PM and the virtual control input
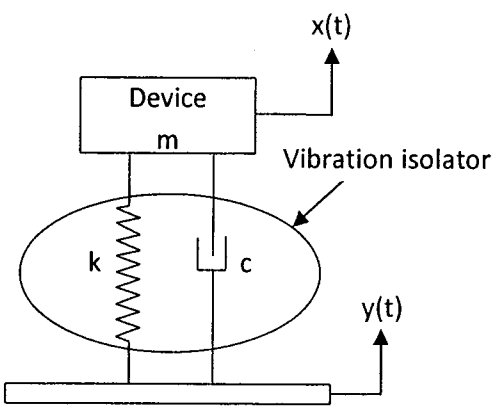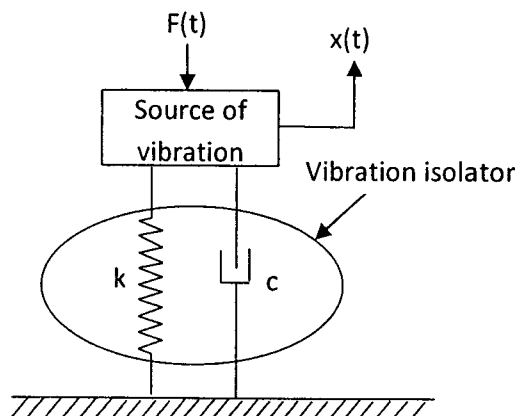
Chapter 1. Introduction

1.1 Background

Vibration is a physical phenomenon of oscillation of objects with respect to an equilibrium position [1]. Vibrations can be desirable in everyday life and industrial environment. People depend on sound vibration to communicate; a powder vibrating sieve uses vibration to separate the fine from the coarse particles. Vibration can also be undesirable. The extreme example is earthquake. Certainly, the undesired vibration should be suppressed. Scientists and engineers have worked on the vibration suppression for a long time and a vast amount of applied technology relating to vibration control has emerged over the last thirsty years or so [2].

Vibration isolation is one of the most effective methods of suppressing vibration [3]. In the simplest vibration isolation model, the isolator consists of a spring and a damper. The spring is used to support the mass. This kind of isolator can handle two different isolation problems. In the first case, the vibration of the mass is transmitted from a base excitation. In the second case, the ground subjects to the vibration which is generated by a vibration source. For the two isolation problems, two methods are used to evaluate the isolator performance. In the first case, how much the displacement from the base excitation transmits to the mass is concerned. The transmissibility ratio is defined as the ratio of the steady state response amplitude of the mass to the base excitation amplitude. The second case concerns the force transmitted from the mass vibration. Thus, the transmissibility ratio is defined as the ratio of the transmitted force amplitude to the applied force amplitude. The frequency ratio r is defined as the ratio of the excitation frequency ω_b to the system natural frequency ω_n, namely $r = \omega_b/\omega_n$, and the damping ratio is defined as $\zeta = c/(2\sqrt{km})$. It is found that the transmissibility ratio T.R. is a function of frequency ratio r and damping ratio ζ. Table 1.1 summarizes the two isolation problems. The table indicates that the two transmissibility ratio functions are identical. It should be noted that the two functions describe different isolation problems, even though they have the same format.

1

Table 1.1   Vibration Isolation Transmissibility Formulas [1].

Displacement Transmissibility	Force Transmissibility
Vibration source modeled as base motion	Vibration source mounted on isolator
$y(t) = Y sin\omega_b t$	$F(t) = F_0 sin\omega t$
$\dfrac{X}{Y} = \left[\dfrac{1 + (2\zeta r)^2}{(1 - r^2)^2 + (2\zeta r)^2}\right]^{1/2}$	$\dfrac{F_T}{F_0} = \left[\dfrac{1 + (2\zeta r)^2}{(1 - r^2)^2 + (2\zeta r)^2}\right]^{1/2}$
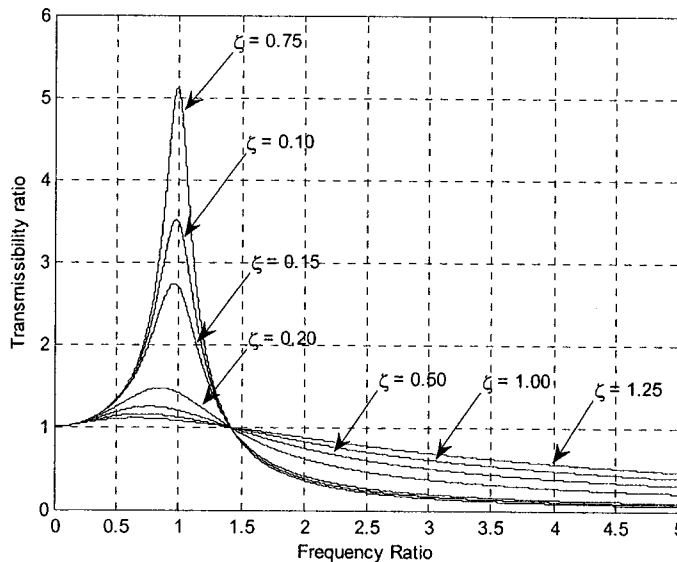
Figure 1.1   Transmissibility ratio as a function of the frequency ratio for different damping ratios.

Figure 1.1 is a plot of the transmissibility ratio function for several values of the damping ratio ζ. It is noted that the transmissibility ratio becomes less than one when the frequency ratio is greater than $\sqrt{2}$. This observation indicates that, in a certain region, the amplitude of the steady

state response is less than the amplitude of the base excitation, and therefore vibration isolation occurs. The region is defined as the isolation region. In the isolation region, the transmissibility ratio decreases with an increase of the frequency ratio. The damping ratio also has an effect on the transmissibility ratio. A larger damping ratio corresponds to a larger transmissibility ratio and therefore causes a worse isolation. In order to make an isolator work in different operating conditions, an isolator should have a smaller damping ratio and wider isolation region.

However, a smaller damping ratio results in bigger amplitude of the steady state response at resonance. A practical method to increase the width of the isolation region is to decrease the natural frequency of the isolation system. The mass has been usually determined before the isolator design, thus the reduction of the isolator stiffness is an effective way to decrease the natural frequency of the system. A decrease of stiffness also increases the damping ratio, and therefore decreases the amplitude at the resonance. On the other side, a lower stiffness of the isolator causes a larger static deflection which is impractical in some industrial applications.

Therefore, the ideal isolator should have high static stiffness to support the load and a low dynamic stiffness to increase the width of the isolation region. This is the principle of the high-static-low-dynamic stiffness (HSLDS). In this thesis, a mechanical spring is used to support the mass to the equilibrium position, and then a negative spring is added to the system to reduce the dynamic stiffness of the system.

1.2 Literature Review

Vibrations of structure caused by external excitations are very common in engineering, ranging from high-rise buildings to piping systems. Suppression of such vibrations is becoming more and more pressing issue nowadays. Many vibration suppression techniques emerge and one of the most effective methods is vibration isolation. The first part of this thesis is to concern with passive isolation systems and tunable isolation systems which belong to the family of semi-active control devices. In fact, also active isolators, which are investigated in the second part, play a major role in the field of vibration isolation.

1.2.1 Passive vibration isolation

One of the simplest isolation models is the single-degree-of-freedom (SDOF) system that is modelled as an elastic spring in parallel with a viscous damper [4]. This kind of isolator, named as a passive isolator, is extensively used in engineering applications because the isolator does not require any external power source or computer control and hence is not expensive.

In practise, the function of the spring and the function of the damper may be performed by a single element such as natural or synthetic rubber. For a given amount of elasticity, deflection capacity, energy storage, and dissipation, the rubber isolator requires less space and less weight, and therefore it is usually cheap. However, due to the viscoelastic nature of the material, the behaviour of the rubber isolator is complex and it is usually studied on a case-by-case basis. The characterizations of rubber isolators have been widely studied in [5, 6].

Through the different combinations of springs and dampers, several types of isolators are obtained. The model with an elastic spring in parallel with a viscous damper is generally called the Voigt model. The model in which a purely elastic spring and a purely viscous damper are connected in series is named as the Maxwell model. Figure 1.1 indicates that an increase of damping ratio decreases the peak amplitude of the response at expense of the performance detriment in the isolation region. It has therefore been suggested that elastically connecting the spring may offer some potential benefits. The model with the parallel combination of a spring and an elastically supported damper is defined as the Zener model. [7, 8] present a consistent and concise analysis of the Zener model. Table 1.2 summarizes the three models.

Table 1.2   Vibration Isolation models.

Voigt model	Maxwell model	Zener model

4
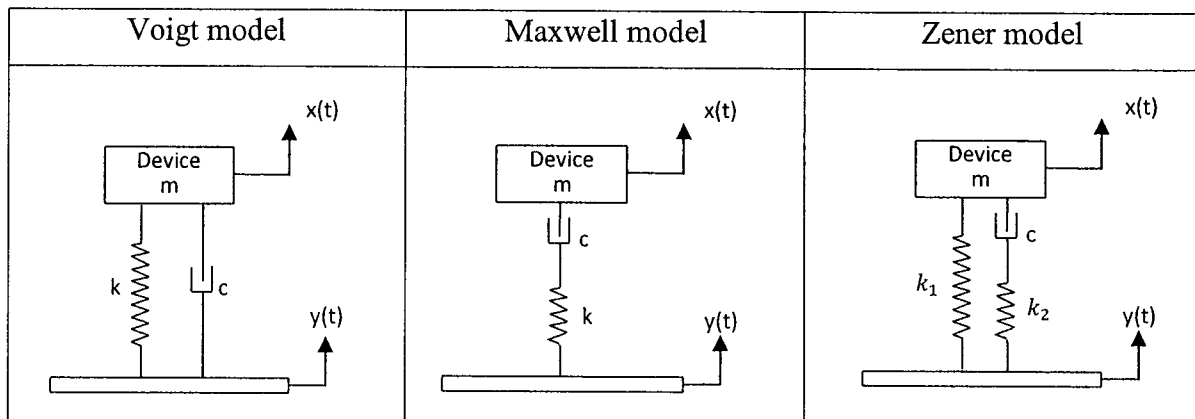
Figure 1.1 implies that a lower natural frequency of the isolator possesses a wider isolation region and that a lower damping ratio of the system has a better performance in the isolation region. In most cases, the lower natural frequency of the system comes from the lower static stiffness of the spring which results in a larger deflection and thus is impractical in many industrial applications. A desirable isolator should have a high static stiffness to support the load and a low dynamic stiffness to widen the isolation region [9].

A number of ways have been developed to obtain the desirable isolator. One is to add oblique springs as a negative spring in order to obtain a high-static–low-dynamic stiffness [10]. Kovacic et al. [3] introduce how both geometrical and physical nonlinearity in the oblique springs offers some benefits. Carrella et al. [11] established their isolator by using a linear mechanical spring connected to a magnet spring in parallel. The isolator developed in this thesis is to connect a nonlinear mechanical spring in parallel with a negative stiffness spring. Two kinds of the mechanical springs are concerned in this study. One has high nonlinearity and the other has low nonlinearity. The negative spring is produced by a permanent magnet and a pair of electromagnets arranged in attracting configuration. The notable feature is that the stiffness of the negative spring can achieve on-line tuning such that the isolation region can be increased whenever it is needed.

1.2.2 Active vibration isolation

Figure 1.1 indicates that the steady state response of the mass is amplified when the frequency ratio is less than $\sqrt{2}$. Especially, the amplitude of the response reaches the peak value at the resonance or $r = 1$. The amplification of the base excitation is certainly not desirable. An external control force can be used to cancel the vibration when the isolator does not work in the isolation region. In addition, the force can provide additional attenuation of the response when the isolator works in the isolation region. The isolator with this mechanism is named as active vibration isolator. The active vibration isolation has become prevalent in the last few decades due to the development of real-time simulation systems [12].

There are two fundamental approaches towards developing an active vibration isolation system: feedforward control and feedback control [13]. A system with feedforward controller measures the disturbance and then generates a control signal to drive actuators in order to cancel

5

the disturbance. When a model of a system is well known and a signal that is well correlated with the disturbance input is available to the controller, the feedforward controller can be used to improve the performance of a control system. On the other hand, a system with feedback controller measures the difference between the reference signal and the actual output signal and then produces a control signal to drive actuators to attenuate the system response. Feedback control is generally used for a system that has time varying disturbances and/or parameters. It is also used when the feedforward controller does not meet the design specifications. Since the base excitation is uncertain and hence is unpredictable in the most cases [14], feedback control is widely used in isolating delicate equipment or structure from the base vibration.

Figure 1.2 [12] demonstrates a traditional active vibration isolation model with an output feedback controller. This kind of vibration isolation mode is widely used by researcher [15]. It consists of a passive isolator and an actuator system. In addition to support the load, the passive isolator is also used to isolate the vibration transmitted from the base excitation when the frequency ratio is in the isolation region. One or more sensors measure the responses of the system. These responses are passed to the control system and are compared to the reference signal, which should be zero for vibration isolation case. The control system generates the control force on the basis of the difference between the reference signal and the actual response. The control force is applied to the load to attenuate the difference. This is the principle of the active vibration isolation by using feedback approach.
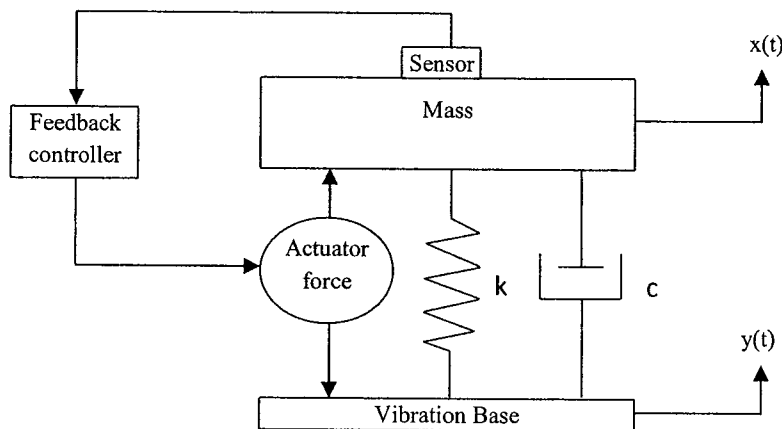
Figure 1.2   Schematic diagram of a traditional active vibration isolation model.

6

In practise, different kinds of sensors are used to measure the response of the system and then the responses are fed into the control system. The typical approach is to use accelerometers and relative position sensors to measure the responses of the system [16]. [17, 18] measure the absolute velocity of the system. Benassi and Ellilot [19] designed an effective controller by using the displacement signal of the load as input. A unique vibration isolation system using zero-power magnetic suspension [20-23] also belongs to the family of the active vibration isolation. A zero-power system generates infinite stiffness against disturbance on the isolation table.

In addition, different control design strategies can be used to design the controller. Some novel control design techniques are used in active vibration isolation [24, 25]. In this thesis, an adaptive fuzzy-neural network controller which is constructed through the backstepping technique is used.

1.2.3 Semi-active vibration isolation

Passive isolators can effectively reduce the vibration transmitted from the base excitation when the frequency ratio is in the isolation region. When a change of system characteristics occurs or the system shifts to the amplification region, the passive isolator is not effective. Active vibration isolators overcome the drawbacks of passive systems and achieve high performances in vibration isolation. However, traditional active vibration isolation systems need high-performance sensors, real-time control system and external power supply to generate the control force. As a result, the systems become rather costlier than the passive isolator, and therefore, restrict the application fields of them. Semi-active vibration isolators, in which the systems mechanical properties can be adjusted in real time, possess the advantages of both passive and active control isolators. Semi-active vibration isolators can maintain the reliability of passive isolator using a small amount of energy to tune the system, provide the versatility, adaptability and higher performance of fully active systems [26].

In a semi-active isolator, the isolation is produced by passive elements, but their properties such as stiffness or damping can be changed with time to retain optimal isolation performance. Figure 1.3 demonstrates traditional semi-active vibration isolation. Unlike active control systems, the semi-active isolators do not need to generate control forces to suppress the vibrations, and therefore consume only a small amount of energy. One widespread way to adjust

the isolator properties is to change the damping of the isolator. Electrorheological (ER) and magnetorheological (MR) fluids, discovered in the late 1940's, can change their viscosity when immersed in an electrical or magnetic field. Therefore, ER or MR has the ability to alter the dynamic behaviour of the system [27]. On basis of the phenomenon of eddy current, Liu et al. [28] developed an electromagnetic damper that the damping coefficient was related to the current in the electromagnet. Four semi-active damping control strategies are described in [26]. Stiffness of the isolators is the other property that can be adjusted. Liu et al. [29] developed a tunable vibration absorber whose stiffness could be varied on-line. Jin et al. [30] briefly reviewed the basic theoretical concepts for semi-active vibration control design and implementation, and surveyed recent developments and control techniques for these semi-active vibration control systems.
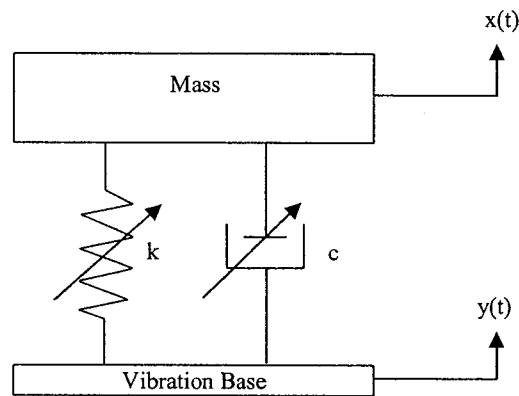
Figure 1.3   Schematic diagram of a traditional semi-active vibration isolation model.

A tunable vibration isolator with HSLDS belongs to the family of semi-active control isolator. The passive vibration isolators with HSLDS are an effective means to suppress the steady-state vibration transmitted from a harmonic base excitation. When the characteristics of the system have been changed or the frequency of the base excitation becomes extremely low, the passive vibration isolator with HSLDS may not work effectively. Tunable vibration isolators can overcome the limitations of the passive HSLDS isolators. The ability of on-line tuning can also make the isolators quickly adapt to the operating conditions and work in the optimal performance.

8

1.3 Objectives and Contributions

A traditional passive vibration isolator, which consists of a mechanical spring and a damper, is effective when the frequency of the base excitation is high. A high-static-low-dynamic stiffness isolator (HSLDS) is developed to overcome the limitation of the traditional passive isolators. Carrella et al. [11] investigated an HSLDS isolator using two linear mechanical springs and one permanent magnet spring. The trade-off between the maximum stiffness and available desired region without the system becoming unstable restricts the application of the isolator.

In practice, many mechanical springs such as beam-like springs are not linear. Such the springs exhibit a hardening effect, i.e., the larger the deformation, the stiffer the spring. When a mechanical spring with the hardening effect is used in an isolator, it becomes more challenging to realize the HSLDS property. Plus, the stability problem limits the isolation region of the nonlinear isolators. On the other hand, in order to actively control a nonlinear isolator, a more effective control algorithm is needed.

In order to overcome the restrictions and the shortcomings of the existing vibration isolators, this study aims at developing more effective isolators. Two major goals are set for the research. First, the study intends to develop a tunable HSLDS isolator consisting partly of a highly nonlinear mechanical spring. Second, the study intends to apply a control algorithm that suits for active control of isolators with nonlinearity and parameter uncertainty.

For the first goal, an electromagnetic isolator is proposed. The proposed isolator possesses the HSLDS property and can act passively or semi-actively. The study focuses on the characterization of the isolator in order to optimize its design. The specific objectives in this regard are as follows:

(1)   To establish a magnetic force model and negative spring model;

(2)   To investigate the characteristics of the proposed HSLDS isolator in different configurations;

(3)   To characterize the proposed isolator using Comsol Multiphsics simulation;

(4)   To test the performances of the proposed HSLDS isolator for different configurations.

For the second goal, an adaptive fuzzy-neural network (FNN) controller proposed in [31, 32] is applied. The specific objectives in this regard are as follows:

(1)   To test the effectiveness of the controller in handling an active isolator that is highly nonlinear and uncertain in its parameters;

(2)   To compare the controller with other controllers such as Proportional-Plus-Derivative, Backstepping, and Adaptive Backstepping;

(3)   To develop an electromagnetic active isolator.

From the first part of the study, the following contributions are accomplished:

(1)   A novel HSLDS isolator is developed. The isolator can provide a high static stiffness through a steel beam under tension. The isolator possesses a low dynamic stiffness due to the effect of negative stiffness produced by interaction between the electromagnets and a permanent magnet;

(2)   The magnetic force equations are established.

(3)   An optimisation analysis of the isolator is conducted to maximise the desired isolation region without exceeding a desired low stiffness;

(4)   A computer software package, Comsol Multiphsics, is used to verify the magnetic force equation, study the factors that affect the stiffness of the isolator, and evaluate the isolator performance;

(5)   The dynamics of the nonlinear isolator subject to a base excitation is simulated. The displacement transmissibility is found. The jump frequencies of the isolator under different configurations are identified;

(6)   A lab-scale apparatus is built. Various experiments are conducted to test the performances of the isolator under different configurations. An on-line tuning strategy is developed to maximize the potential of the isolator.

From the second part of the study, the following contributions are accomplished:

(1) The FNN controller design procedure is fully investigated. The controller is applied to the nonlinear isolator. A computer simulation is conducted to compare its performance against three other controllers;

(2) An active isolator based on the electromagnetism is proposed. A preliminary testing is conducted.

1.4 Thesis Outline

The thesis is divided into two parts. Chapters 2 to 5 cover the first part while Chapters 6 to 8 cover the second part.

In Chapter 2, the characterization of the proposed electromagnetic isolator is conducted through experimental and curve-fitting methods. First, the magnetic force is modelled by proper measurement of the actual system. Then, a novel method to identify the magnetic force equation is developed. After identifying the magnetic force equation, the two negative springs and two positive springs are studied. Four different configurations of the isolator are obtained by using these springs. Finally, the performance of all the four isolator configurations is evaluated and compared.

In Chapter 3, Comsol Multiphsics is used to characterize the isolator. First, how the magnetic force is affected by the permeability of the steel core is investigated and how the EM current changes the permeability of the steel core is determined. And then, a simulation is executed to verify the magnetic force model identified in Chapter 2. Finally, dynamic characteristics of the isolator with HSLDS are evaluated in terms of transmissibility ratio.

In Chapter 4, experiment studies are presented. The isolator system is excited by a harmonic motion of the base and its transmissibility is determined for different configurations.

In Chapter 5, the results of Part one are summarized and future works are recommended.

In Chapter 6, a brief review on fuzzy neural networks is presented and the FNN controller is introduced.

In Chapter 7, a computer simulation is conducted to study the effectiveness of the FNN controller and compare it with the three different controllers.

In Chapter 8, the results of Part two are summarized and future works are recommended.

Part I

A Tunable High-Static-Low-Dynamic-Stiffness Isolator

Chapter 2.   A Tunable HSLDS Isolator

In this chapter, the concepts of negative stiffness and tunable stiffness are introduced and discussed. The behaviours of the proposed HSLDS isolator are investigated. The chapter is organized as follows. Sections 2.1 and 2.2 introduce the proposed tunable HSLLDS isolator. Section 2.3 studies the permanent magnet spring. Section 2.4 examines the electromagnet spring. Sections 2.5 and 2.6 investigate two types of mechanical springs. And finally, Section 2.7 characterizes the isolator with different configurations.

2.1 Introduction

It has been argued that a passive isolator with a lower natural frequency is effective. Apparently the natural frequency of a linear isolator is limited by the required enough mount stiffness to support a static load. An ideal vibration isolator should possess the characteristic of HSLDS. This can be achieved by non-linear springs. One way to reduce the dynamic stiffness without paying the penalty of a low static stiffness is to use a parallel combination of positive and negative stiffness elements. The direct benefit of a HSLDS mount is a wider frequency isolation region. There may also be another advantage. The damping ratio ζ of an isolator is

$$\zeta = \frac{c}{2\sqrt{km}} \qquad (2.1)$$

where c is the damping coefficient; k is the stiffness and m is the mass. With the constant value of damping coefficient c of the isolator, the damping ratio ζ will increase with a decrease of the stiffness k and therefore the transmissibility peak will decrease. As a high damping ratio may be detrimental to the isolation performance, the damping coefficient should be adjusted accordingly when the detriment is too serious.

In [11], a HSLDS mount was developed. It comprises two linear mechanical springs and three PMs. The middle PM is considered to be the mass whose vibration is to be isolated. The three PMs are arranged so that the middle one is attracted by the other PMs. Thus, the combination of the three PMs acts as a negative stiffness counteracting the positive stiffness provided by the mechanical springs. In industrial applications, mechanical springs tend to be

13

nonlinear. In addition, working conditions such as base excitation frequency may vary from time to time. Thus, the isolators should have a capability of dealing with uncertain disturbances. It is desirable that the characteristics of the isolators can be easily adjusted so that the isolators can adapt to different working conditions. In this thesis, a tunable HSLDS isolator was proposed.

2.2 Illustration of the Tunable HSLDS Isolator

Figure 2.1 shows a schematic of the proposed tunable HSLDS isolator. A steel beam (1) is used to support a PM (2) which acts as the isolated mass. The PM-beam assembly is placed between a pair of EMs (3). The beam acts a positive hardening mechanical spring. The interaction between the PM and the EMs results in two magnetic springs: the PM spring and the EM spring. The PM spring is due to the attraction between the PM and cores of the EMs. The PM spring has a negative stiffness. The EM spring is due to the interaction between the PM and EMs. The EM spring can have a negative or positive stiffness, depending on the polarity of the current in the EMs. The parameters of the apparatus are listed in Table 2.1.
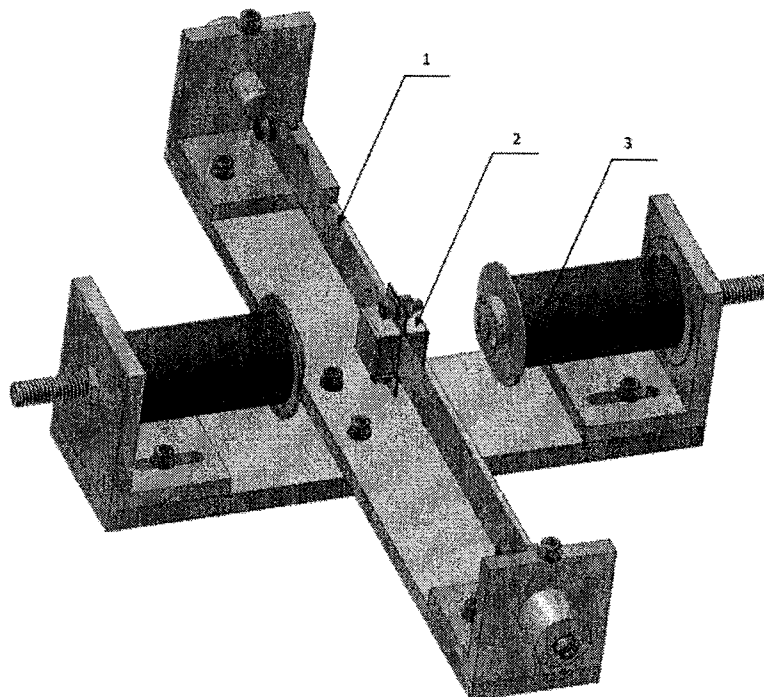
Figure 2.1   An schematic of the proposed tunable HSLDS isolator.

14

Table 2.1   System parameters.

Symbol	Description	Value
r_1	Inner radius of the electromagnetic coils	6.5 mm
r_2	Outer radius of the electromagnet coils	23.3 mm
l_{em}	Length of the electromagnet coils	88 mm
l_s	Length of the steel core	150 mm
N	Turns of the coils	3565
μ_0	Permeability of free space	$4\pi \times 10^{-7}$ H/m
l	Length of the permanent magnet	25.4 mm
w	Width of the permanent magnet	25.4 mm
h	Thickness of the permanent magnet	29.0 mm
M	Magnetization of the permanent magnet	786.23 kAm^{-1}
R	Resistance of the coil	13.0 Ω
d_{22}	Diameter of Gauge 22 copper wire	0.69 mm
L_{em}	Inductance of the coil	150 mH

2.3   The Permanent Magnet (PM) Spring

2.3.1 The PM spring with a fixed gap of the cores

First, the magnetic stiffness of the PM placed between the two steel cores is studied. The gap distance of the cores is fixed. When the PM is displaced relative to the cores, a net force results (see Figure 2.5). The net force acting on the PM produces the PM spring with negative stiffness. Before going into the details of the PM spring, it is necessary to study the interaction force between the PM and the steel core.

Considering an orthorhombic PM illustrated in Figure 2.2, the magnet with a dimension of $l \times w \times h$ can be represented by two rectangles of surface pole density $\sigma = \pm M$, where M is the magnetization of the PM [33]. Magnetization, defined as the quantity of magnetic moment per

15

volume, is a property of some materials (e.g. magnets) that describes to what extent they are affected by magnetic fields, and also determines the magnetic field that the material itself creates.
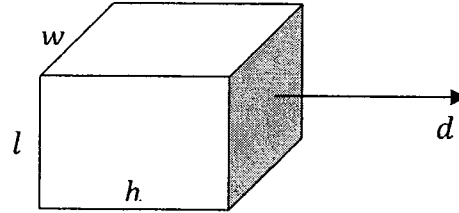
Figure 2.2   A PM block.

The magnetic flux density on the central axis at d distance from the surface of the PM can be found by [33]:

$$B_d = \frac{\mu_0 M}{\pi}\left[\sin^{-1}\frac{lw}{\sqrt{(l^2+4d^2)(w^2+4d^2)}} - \sin^{-1}\frac{lw}{\sqrt{(l^2+4(d+h)^2)(w^2+4(d+h)^2)}}\right] \qquad (2.2)$$

Thus, given the magnetic flux density, the magnetization can be calculated by equation (2.2).

The Magnetic Materials Producer Association allows up to 10% variation in magnetic energy from its nominal value because many factors in production of PM have an influence on its properties. For this reason, properties of the permanent magnet used in this thesis are determined through an experiment. In this experiment, a DC magnetometer (AlphaLab Inc., Model: DCM) is used to measure the magnetic flux density along the centerline of the PM. The experiment shows that the magnetic flux density measured from each side of the PM differs from each other. The density at the south side, denoted as negative value is slightly stronger than the one at the north side. Figure 2.3 illustrates the relationship between the distance and absolute value of the magnetic flux density at the north side and south side.

Without loss of generality, it is assumed that the magnetic flux density at both the north and south side has the same distribution in the air. Thus, at different distance to the surface of the north or south side, an average axial flux density is obtained. Using equation (2.2), the magnetization of the PM can be calculated for different distances. A Matlab program computes the average magnetization for different distances. In order to achieve more accurate magnetization of the PM, the least squares method and golden section search method are employed. It is found that the best estimate of the magnetization is $M = 7.8623 \times 10^5$ Am^{-1}.

16

Figure 2.4 shows a comparison of the experiment results and the computed ones using equation (2.2).
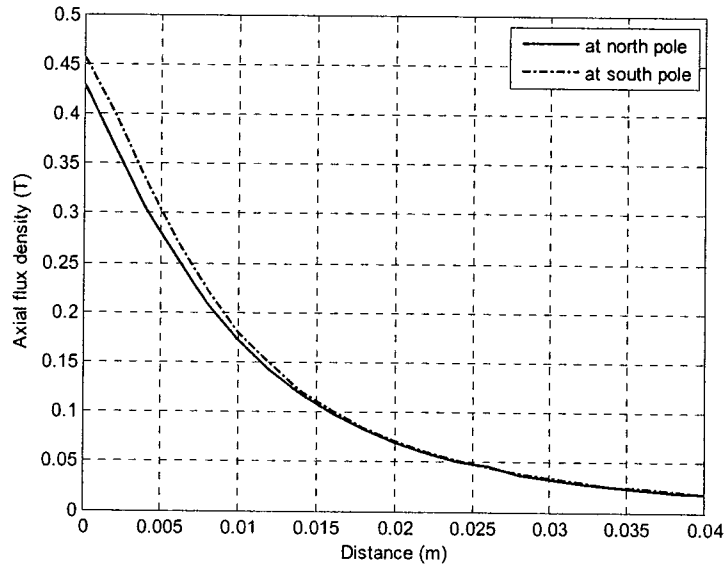
Figure 2.3 Magnetic flux density along the centerline of the PM with the origin located at the center of the pole face.
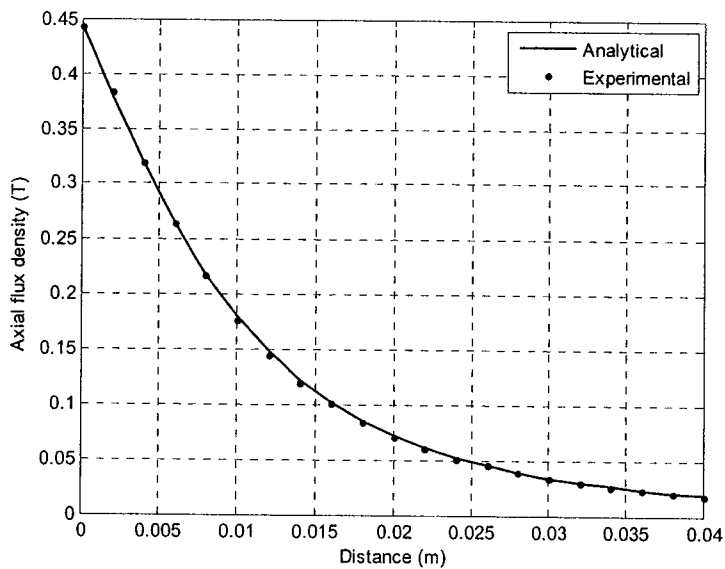
Figure 2.4 Comparison of the results from analytical computation and the experiment.

The interaction force between the PM and the steel core is approximated as [4]

$$F_{pc} = \alpha B_d^2 A \qquad (2.3)$$

17

where α is a constant to be determined, A is the area of the PM surface, and B_d is the flux density at the surface of the steel core. The free body diagram of the PM in middle of two steel cores is shown in Figure 2.5.
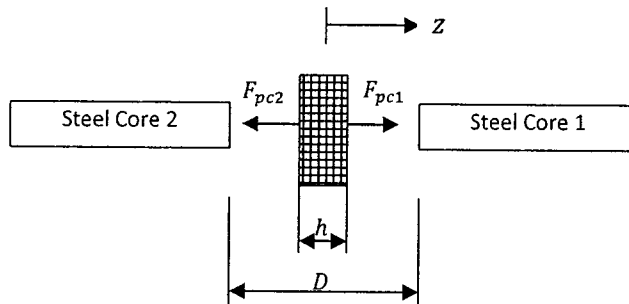
Figure 2.5   The free body diagram of the PM in middle of the two steel cores.

The net force acting on the PM is given by

$$\Delta F_{pc} = F_{pc1} - F_{pc2} = \alpha A (B_{d1}^2 - B_{d2}^2) \tag{2.4}$$

where B_{d1} and B_{d2} are the flux density at the right and left face of the steel core, respectively. Thus, given the net force, the constant value α can be calculated through equation (2.4). In order to find the value of α, an experiment was set up to determine the relationship of the net force acting on the PM and the displacement of the PM. The gap distance between the two steel cores was 0.070 m in this experiment. Figure 2.6 illustrates the setup that determines the net magnetic force. The force gauge (Rapala, 50Lbs) was used to measure the net force acting on the PM when the PM was displaced relative to the center of the gap.
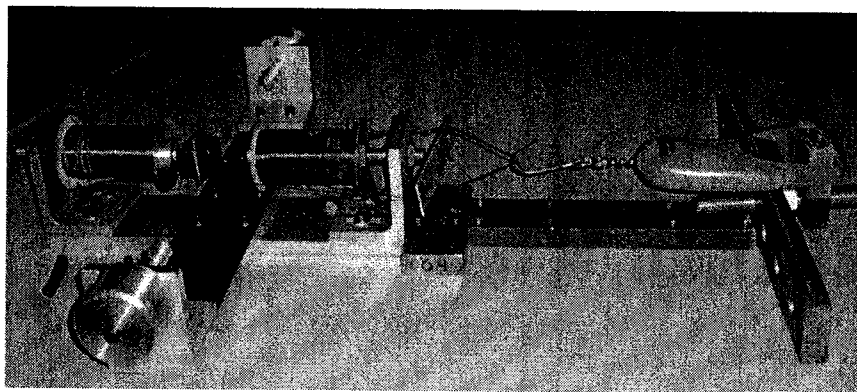
Figure 2.6   A setup to measure the net magnetic force acting on the PM

Applying the least squares and golden section search methods, the constant α is found to be $6.6661 \times 10^5\ mH^{-1}$. Equation (2.4) indicates that the net magnetic force is a function of gap

distance between the faces of the steel cores. It was found that the constant α varies with the change of the gap distance. This is a drawback of using equation (2.3) to compute the magnetic force between the PM and the steel core. Figure 2.7 compares the experiment results and the ones obtained using equation (2.4). It is noted that the stiffness of the PM spring is negative and the setup possesses the characteristics of a softening spring, i.e., the greater the spring deflection, the less the stiffness.
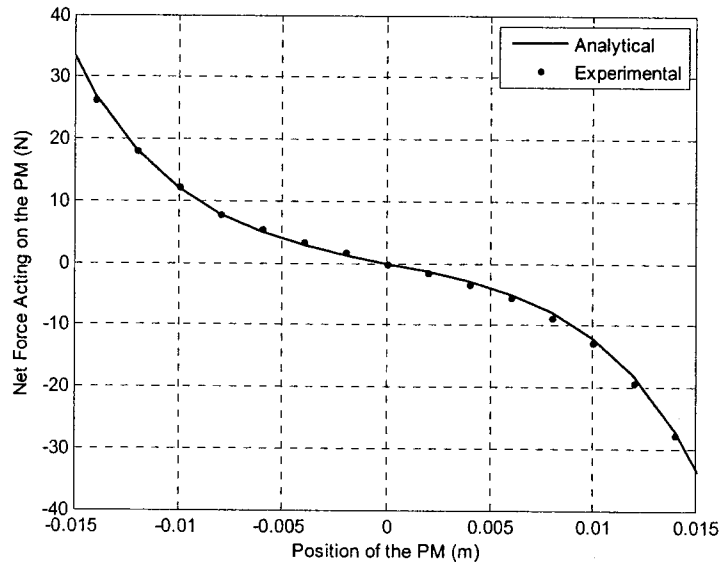
Figure 2.7   Comparison of the net magnetic force between analytical results and experimental results.

2.3.2 The PM spring with variable gap distance

Equations (2.2) and (2.3) are used to calculate the magnetic force between the PM and steel cores, but they are in a complicated form. Furthermore, even using the two equations, the parameters α and M still should be determined from experiment results. Therefore, in order to simplify the calculation of the magnetic force, it is better to draw an equation from the experiment results directly.

Coulomb's law states that the attracting or repelling force between two magnets is inversely proportional to the square of the distance [34]:

$$F_p = \frac{C_m}{d^2} \tag{2.5}$$

19

where the constant $C_m = Cp_1p_2$ with C being the magnetic permeability of the medium and the scalars p_1 and p_2 are the pole strengths of the magnets; d is the distance between the two magnets. What is of interest here is to determine the interaction force between the PM and the steel core. An experiment setup shown in Figure 2.8 was used to measure the magnetic force for different distances between the PM and the steel core. The experiment results are shown in Figure 2.9.
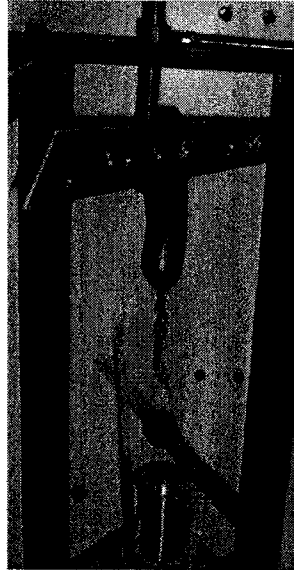
Figure 2.8   A setup to measure the attracting magnetic force between the PM and the steel core
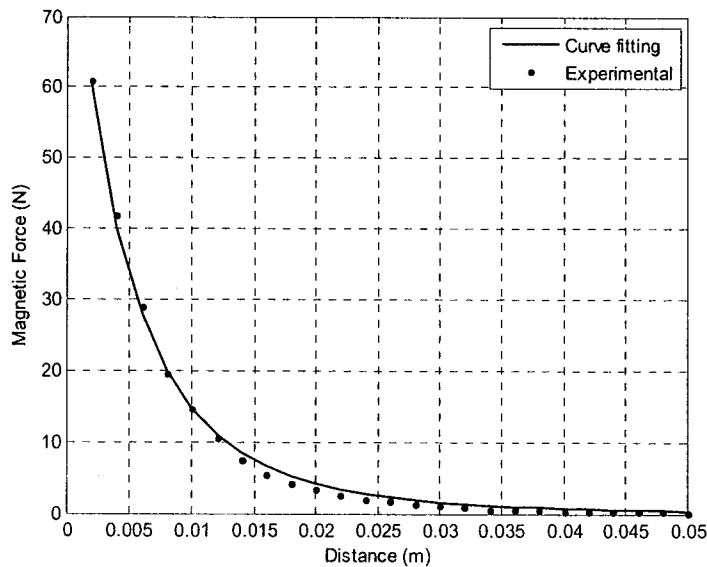
Figure 2.9   Comparison of the magnetic force between curve fitting and experimental results.

Inspired by Coulomb's law [35], an analytical model for F_{pc} is assumed to be of the form:

$$F_{pc} = \frac{a_1}{(d+a_2)^4} \tag{2.6}$$

where d is the distance between the PM and the steel core, a_1 and a_2 are constants to be determined. A nonlinear optimization was carried out to find the best estimated values for a_1 and a_2 such that the sum of the squared errors between the measured values and the values computed by equation (2.6) is minimized. Figure 2.9 compares the experiment results and the computed results from equation (2.6) with the optimum values of $a_1^* = 7.7114 \times 10^{-6}$ and $a_2^* = 1.6919 \times 10^{-2}$.

When the PM placed between the electromagnets that are not energized displaces a distance z as shown in Figure 2.5, the attracting forces acting on each side of the PM can be respectively represented as:

$$F_{pc1} = \frac{a_1}{(d_1+a_2)^4} \tag{2.7}$$

$$F_{pc2} = \frac{a_1}{(d_2+a_2)^4} \tag{2.8}$$

where

$$d_1 = \frac{D-h}{2} - z \text{ and } d_2 = \frac{D-h}{2} + z \tag{2.9a, b}$$

With equations (2.7) and (2.8), the net attracting force acting on the PM is given as

$$\Delta F_{pc} = F_{pc2} - F_{pc1} = \frac{a_1}{(q_1+z)^4} - \frac{a_1}{(q_1-z)^4} = -8a_1 q_1 \frac{z(q_1^2+z^2)}{(q_1^2-z^2)^4} \tag{2.10}$$

where $q_1 = \frac{D-h}{2} + a_2$. Figure 2.10 compares the experimental results and the results computed by equation (2.10) for a gap distance of $D = 0.0700$ m. It can be seen that a good agreement is obtained. The stiffness of the magnetic spring can be obtained by differentiating equation (2.10) with respect to z

$$k_{pc} = -8a_1 q_1 \frac{5z^4+10q_1^2 z^2+q_1^4}{(q_1^2-z^2)^5} \tag{2.11}$$
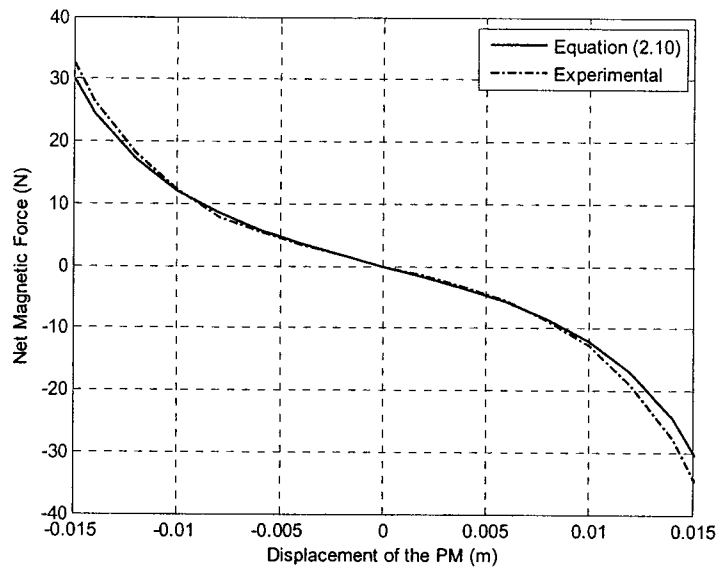
Figure 2.10   Comparison of the magnetic force computed by equation (2.10) and experiment results.

Figure 2.11 presents the stiffness of the system vs. the displacement of the PM for four gap distances. It can be seen that the softening effect of the PM spring increases with a decrease of the gap distance. In addition, an increase of the gap distance results in an increase of the PM spring stiffness. Therefore, given a positive stiffness, a better HSLDS can be achieved by adjusting the gap distance between the two steel cores.
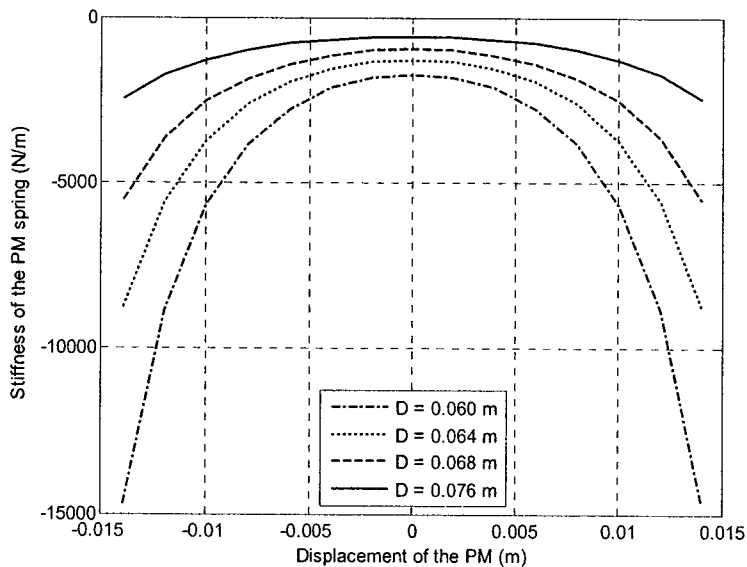
Figure 2.11   Stiffness of magnet spring with different gap distances.

22

2.4 The Electromagnet Spring

2.4.1 The magnetic flux density of the EM

The force acting on the PM caused by the EM depends on the magnetic flux density of the EM, the magnetic flux density of the PM, and the permeability of the EM core. A single current loop can be considered to be a basic element of an EM. Figure 2.12 demonstrates the loop with a radius "a" and current "i".
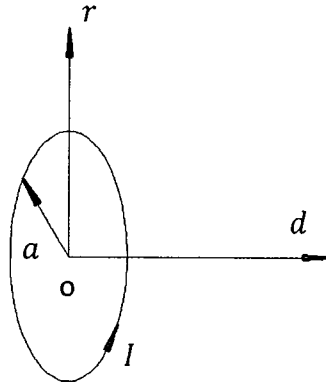
Figure 2.12 A single circular loop [36].

The Bio-Savart law relates magnetic fields to the electric currents which are their sources. According to the Bio-Savart law, the magnetic flux density B_{lr} in the radial direction and the magnetic flux density B_{ld} in the axial direction can be determined by [33]:

$$B_{lr} = \frac{u_0 I d}{2\pi r[(a+r)^2+d^2]^{\frac{1}{2}}} \left[E_2 \frac{a^2+r^2+d^2}{(a-r)^2+d^2} - E_1 \right] \qquad (2.12)$$

$$B_{ld} = \frac{u_0 I}{2\pi [(a+r)^2+d^2]^{\frac{1}{2}}} \left[E_2 \frac{a^2-r^2-d^2}{(a-r)^2+d^2} + E_1 \right] \qquad (2.13)$$

where

$$E_1 = \int_0^{\frac{\pi}{2}} \left[1 - \frac{4ar}{(a+r)^2+d^2} \sin^2 \theta \right]^{-\frac{1}{2}} d\theta \qquad (2.14)$$

$$E_2 = \int_0^{\frac{\pi}{2}} \left[1 - \frac{4ar}{(a+r)^2+d^2} \sin^2 \theta \right]^{\frac{1}{2}} d\theta \qquad (2.15)$$

23

The superposition of contributions of individual loops yields the total flux densities of the coils. By integrating equations (2.12) and (2.13) in both the radial and axial directions, the total magnetic flux densities B_{sr} in radial direction and total magnetic flux densities B_{sd} in axial direction can be computed by:

$$B_{sr} = \int_{r_1}^{r_2} \int_0^{l_{em}} B_{lr}(a, r, d + \lambda)\, d\lambda\, da \qquad (2.16)$$

$$B_{sd} = \int_{r_1}^{r_2} \int_0^{l_{em}} B_{ld}(a, r, d + \lambda)\, d\lambda\, da \qquad (2.17)$$

It is noted that the loop current I should be calculated as:

$$I = \frac{Ni}{(r_2 - r_1)L} \qquad (2.18)$$

where i is the coil current. The total flux density B_{sr} in the radial direction and the total magnetic flux density B_{sd} in the axial direction can be found by the superposition of the flux densities from two EMs.

Adding a steel core inside the electronic coil can significantly enhance the magnetic field produced by the coil alone. Liu et al. [36] used a coefficient to correct equations (2.16) and (2.17). The coefficient, denoted as C_e, is defined as:

$$C_e = \frac{u_r}{\gamma} \qquad (2.19)$$

where u_r is the relative permeability of the steel core and γ is the ratio of the total flux to the gap flux. Many factors, such as, specific experimental setup, temperature, terminal current, material property, and system geometry [37], have effects on the value of C_e, The coefficient usually is determined experimentally. A DC magnetometer (AlphaLab Inc., Model: DCM) is used to measure the axial magnetic flux density at the points along the centerline of the EM. The value C_e was determined in the following way: a modified computed axial flux density was found by multiplying a trial value C_e to the computed B_{sd}; then, the squared error between the measured axial flux density and the modified computed axial flux density was found; by varying the values of C_e, the squared error was minimized [36]. The coefficient C_e is found to be a function of the current in the EM, as shown in Figure 2.13. It can be seen that the coefficient is almost

proportional to the EM current. Figure 2.14 shows a comparison of the measured value and the computed value for the axial flux density along the centerline from the EM.
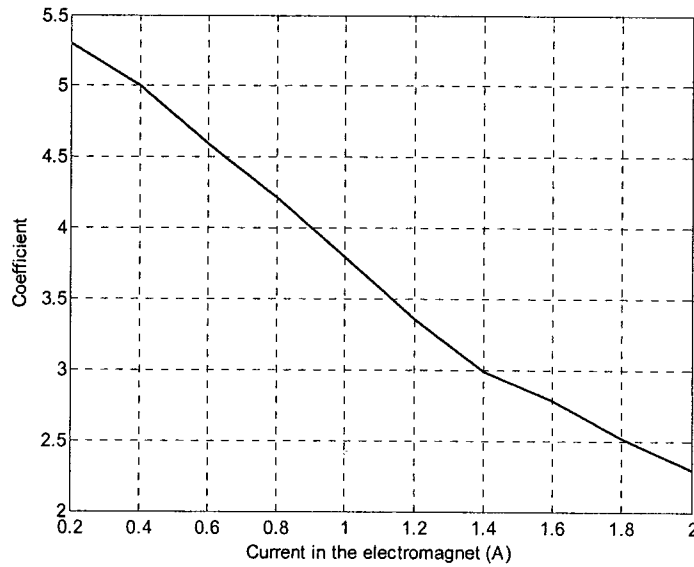
Figure 2.13 The coefficient varies with the change of current in EM.
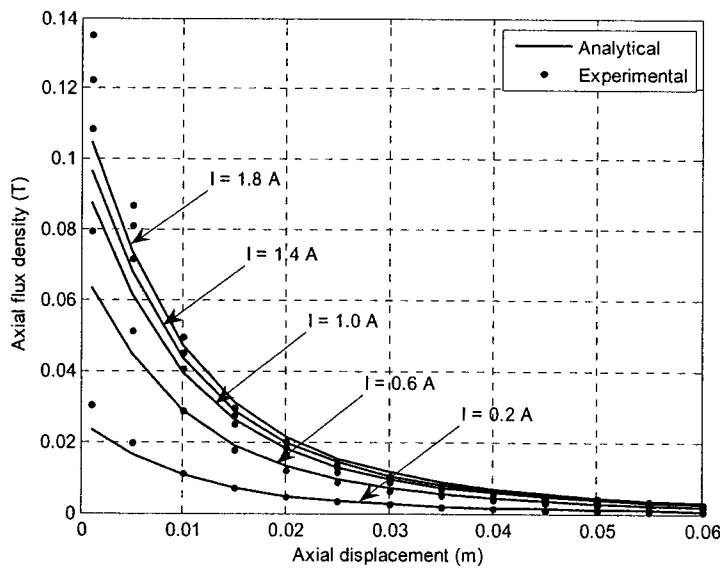
Figure 2.14 Comparison of the measured values and the computed values for the axial flux density along the centerline from an EM.

The method to compute the flux density using equations (2.16) and (2.17) assumes that the magnetic flux densities at points with the same axial distance to the EM surface are same. Due to the nonlinear characteristics of the magnetic field distribution in space, this method can not

accurately model the physical system. In this thesis, an experiment is used to measure the magnetic field distribution. The following steps are conducted in the experiment:

(1) Setup the experiment as shown in Figure 2.15;

(2) Measure the magnetic flux density at various gap distances of each points shown in Figure 2.16;

(3) Change the EM current and then repeat step (2).
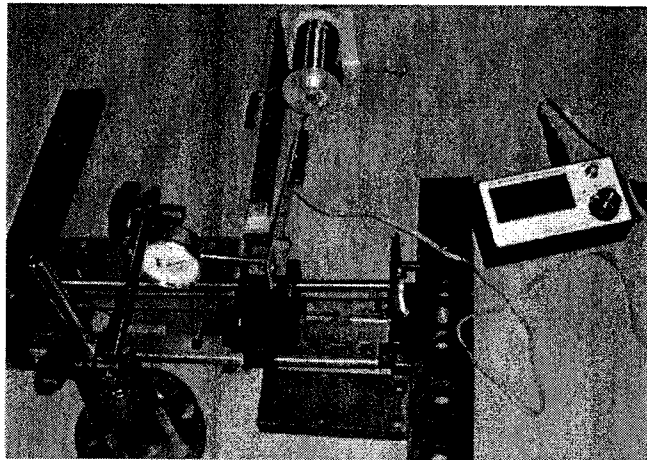
Figure 2.15   A setup to measure the flux density of the EM.
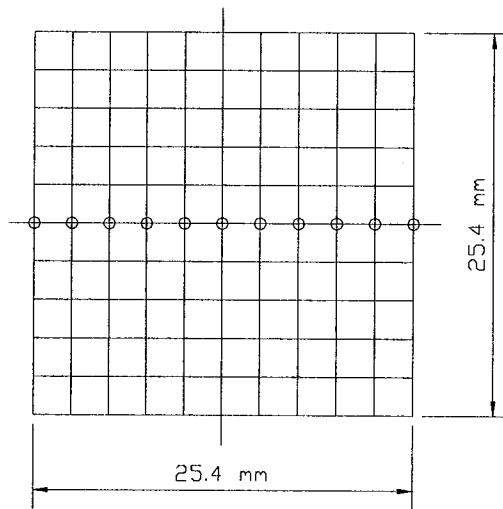
Figure 2.16   Magnetic flux density measuring points.

In the experiment, a cartridge holder of an inkjet printer was used to hold the magnetometer sensor tip such that the tip could move from side to side. The movement of the tip was measured by a dial gauge (KAR, 0.001"). An aluminum beam guided the EM to move back and forth and the movement was measured by a plastic ruler (12"). For each position in the space, the DC

26

magnetometer was used to measure the magnetic flux density. The power supply (Good Will Instrument, Model: GPC-3030D) was used to apply adjustable voltage to the EM. The multimeter (Fluke, 8845A) was used to measure the voltage in the EM. It was found that the electromagnetic flux density magnitude would not change if the EM current direction has been changed.

Figure 2.17 shows the experiment results. The figure indicates that the axial magnetic flux density does not peak along the centerline of the steel core, which is different from the analytical results in [38]. The flux density reaches maximum on the pole faces and decrease with an increase of the distance.
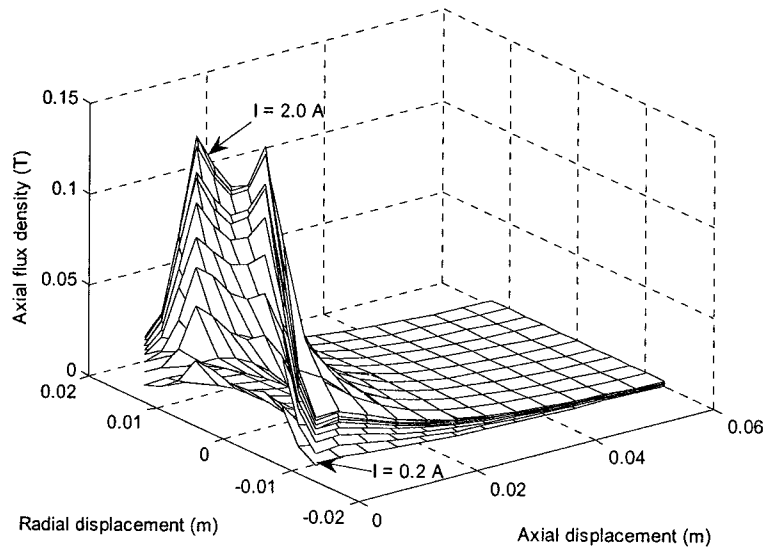
Figure 2.17   The axial magnetic flux density distribution of the EM, coil current from 0.2 A to 2.0 A.

2.4.2 The magnetic force between the EM and PM

The axial interaction force between the EM and the PM is proportional to the difference between the total flux over the pole face S_1 and the total flux over the pole face S_2. The force can be computed by: [36]

$$F_{pf} = M(\int_{S_1} B_{d1} ds - \int_{S_2} B_{d2} ds) \qquad (2.20)$$

where M is the magnetization of the PM, B_{d1} and B_{d2} are electromagnetic flux density on the PM pole face S_1 and S_2, respectively. Therefore, the magnetic force can be calculated if the magnetic field distribution is known. Both Liu [38] and He [39] established a magnetic force model by using the magnetic field distribution computed through equation (2.17). In this thesis, the experimental results in section 2.4.1 are used directly. According to the definition of the integration, equation (2.20) can also be approximately expressed as:

$$F_{pf} = M \sum_i^N (B_{d1i} - B_{d2i}) \nabla S_i \qquad (2.21)$$

where B_{d1i} and B_{d2i} corresponding to the small area ∇S_i were measured in the preceding experiment in Section 2.4.1. The net interaction force in the radial direction is zero due to the symmetry of distribution of the radial magnetic flux.

The round shape of the PM is used to approximate the square shape in order to simplify the computation. Compared to the PM with square shape, the one with round shape slightly overestimates the magnetic force [38]. Because of the symmetry of distribution of the axial magnetic flux, the points that have the same radius should have the same axial flux density. Figure 2.18 shows the distribution of these small areas. The flux density at a point in a small area is used to represent the flux density in the small area. Obviously, the smaller the area is, the more accurate computation result is.
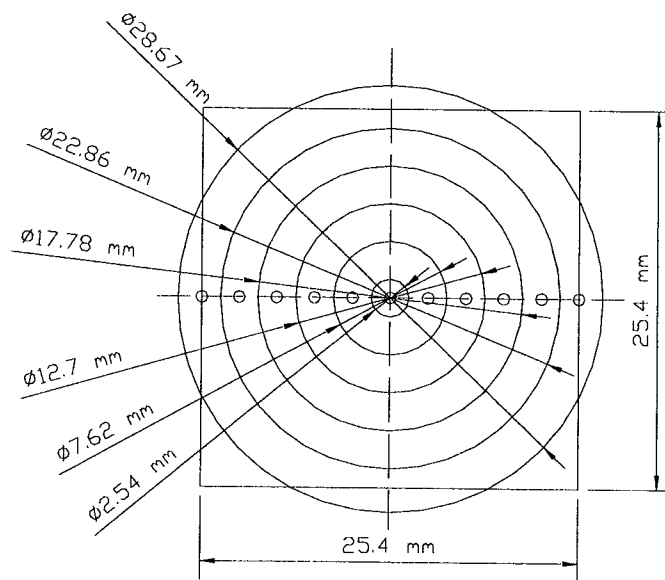
Figure 2.18   Divide the PM pole face into small areas.

28

Figure 2.19 shows computed values of the interaction force. It can be seen that an increase in the current results in an increase of the force magnitude and an increase in the distance causes a rapid decrease in the force magnitude. Due to an insufficient number of the points used, the method may underestimate the magnetic force acting on the PM. A reasonable analytical model may assume the following form:

$$F_{pf} = sign(i)(1 - e^{-b_3|i|}) \frac{b_1}{(d+b_2)^4} \tag{2.22}$$

where $sign(i) = 1$ if $i \geq 0$, $sign(i) = -1$ if $i < 0$, b_1, b_2, and b_3 are constants to be determined. A nonlinear optimization was conducted to find the optimum values for b_1, b_2, and b_3 such that the sum of the squared errors between the values computed by equation (2.21) and the values computed by equation (2.22) is minimized. The solid lines in Figure 2.19 are computed using equation (2.21) with the optimum values of $b_1^* = 4.9192 \times 10^{-5}$, $b_2^* = 2.9855 \times 10^{-2}$, and $b_3^* = 1.2109$. It can be seen that equation (2.22) fits the varying trend of equation (2.21) well. Equation (2.22) will be used in the following discussion.
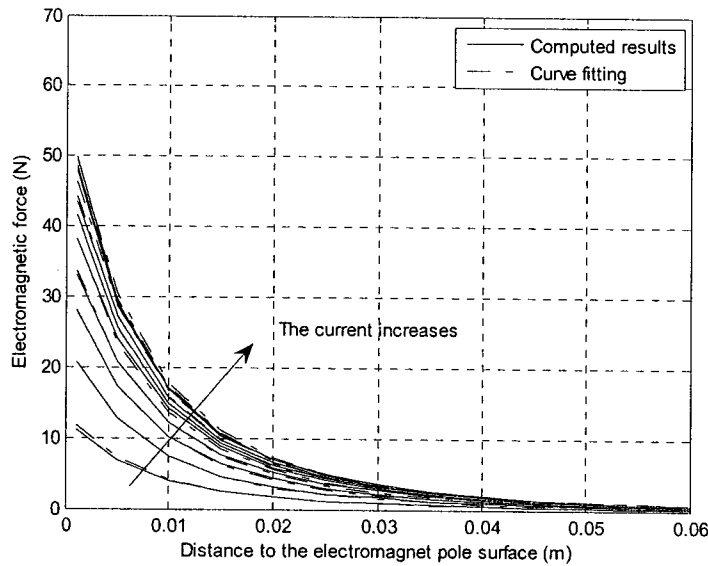
Figure 2.19   Interaction force versus the distance between the EM and PM, EM current varying from 0.2 A to 2.0 A.

2.4.3 The magnetic force among the EM, PM and steel core

It is tempted to assume that this force can be obtained by simply adding equation (2.6) and equation (2.22) [40]. However, many studies have shown that the relative permeability of

ferromagnetic materials is sensitive to several factors such as temperature and magnetization [34, 41, 42]. For example, when an electromagnet is energized, the temperature of its steel core will rise, which inevitably alters the relative permeability of the steel core. And when a permanent magnet is near a ferromagnetic material, the magnetization will lower the relative permeability of the material.

Considering the aforementioned reason, this thesis conducted the following procedure to develop a model for the force between the PM and the energized EM. First an experiment was conducted to determine the interacting force between the PM and the EM at different distances for various currents. The setups shown in Figure 2.8 and Figure 2.20 were used to measure the attracting force and the repelling force, respectively. The dots in Figure 2.21 show the results.
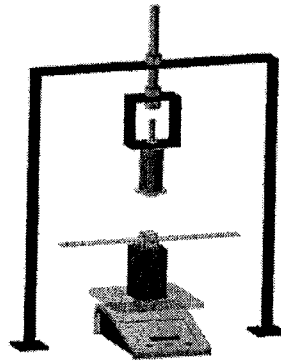
Figure 2.20   A setup to measure the repelling magnetic force between the PM and the EM.
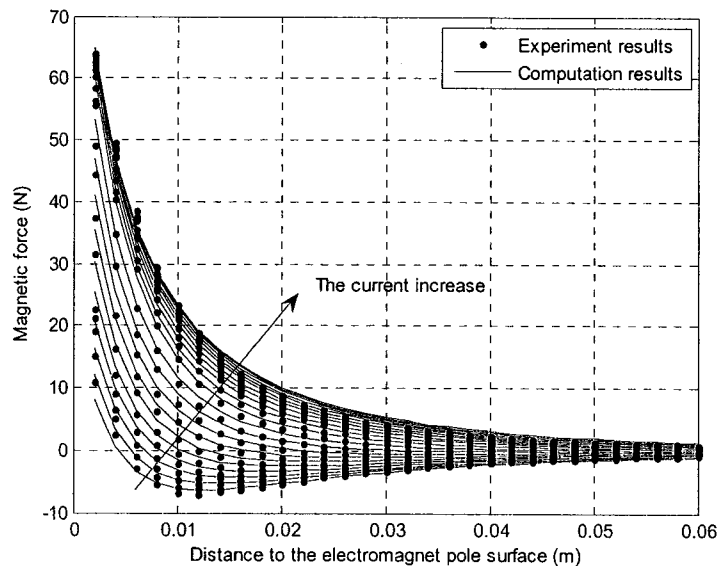
Figure 2.21   Measured magnetic force versus the gap distance among the EM, PM and steel core, EM current varying from -2.0 A to 2.0 A.

Then F_{pc} and F_{pf} are combined in the following way

$$F_{pe} = (1 - a_3|i|)F_{pc} + sign(i)(1 - e^{-b_3|i|})\frac{b_1}{(d+b_2)^4} \tag{2.23}$$

where F_{pe} denotes the force between the PM and the energized EM, F_{pc} is given by equation (2.6) with the optimum a_1^* and a_2^*, a_3, b_1, b_2, and b_3 are constants to be determined. The rational to modify F_{pc} in this way is that an increase in the current magnitude will reduce the relative permeability of the EM core. Also, due to the effect of the PM, the constants b_1, b_2, and b_3 need to be re-determined. Using the measured force values and equation (2.23), a least-squares minimization problem was solved and the best estimated constants were found to be $a_3^* = 0.20811$, $b_1^* = 2.2288 \times 10^{-4}$, $b_2^* = 4.6908 \times 10^{-2}$, and $b_3^* = 0.58781$. The solid lines in Figure 2.21 represent the values computed by equation (2.23) with the optimum constants. It can be seen that equation (2.23) is capable of predicting the varying trends of the measured values.

2.4.4 The stiffness of the EM spring

The interaction force between the PM and the EM with the steel core is defined in Equation (2.23). The free body diagram of the PM in the middle of the two EMs is shown in Figure 2.22.
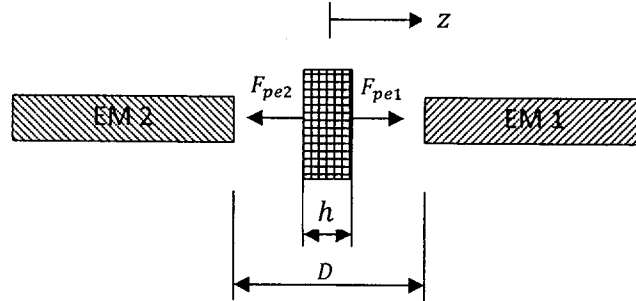
Figure 2.22   The free body diagram of the PM in middle of the two EMs.

The net force acting on the PM caused by the EMs and steel cores is given by

$$\Delta F_{pe} = F_{pe}(d_2, i) - F_{pe}(d_1, i)$$

$$= -8(1 - a_3|i|)a_1 q_1 \frac{z(q_1^2+z^2)}{(q_1^2-z^2)^4} - 8sign(i)(1 - e^{-b_3|i|})b_1 q_2 \frac{z(q_2^2+z^2)}{(q_2^2-z^2)^4} \tag{2.24}$$

where $F_{pe}(\cdot)$ is defined by equation (2.23) and d_1 and d_2 are defined by equations (2.9a) and (2.9b), respectively, $q_2 = \frac{D-h}{2} + b_2$. Differentiating equation (2.24) with respect to z yields the stiffness of the EM spring

$$k_{pe} = -8(1 - a_3|i|)a_1q_1 \frac{5z^4 + 10q_1^2 z^2 + q_1^4}{(q_1^2 - z^2)^5} - 8sign(i)(1 - e^{-b_3|i|})b_1q_2 \frac{5z^4 + 10q_2^2 z^2 + q_2^4}{(q_2^2 - z^2)^5} \quad (2.25)$$

Figure 2.23 shows the relationship of the EM stiffness vs. the displacement z for four currents when the gap distance D is 0.0760 m. It can be seen that with an increase of the current, the EM stiffness becomes more negative and the EM spring becomes softer.
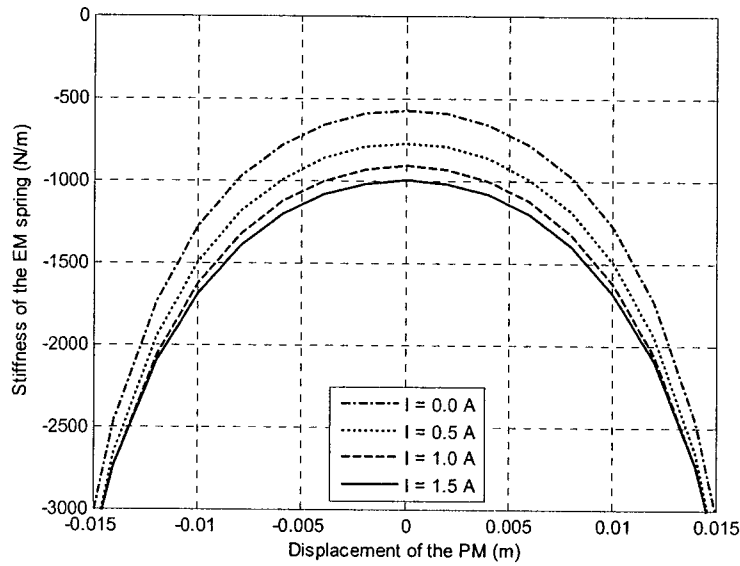
Figure 2.23   Stiffness of the EM spring with different currents when the gap distance is 0.0760 m.

2.5 The Mechanical Spring

Different from the HSLDS isolator proposed in [11] that employed two linear coil mechanical springs, the mechanical spring used in this study is a steel beam that demonstrates strong nonlinearity. This section determines stiffness of two steel beams: highly nonlinear stiffness beam and a low nonlinear stiffness beam.

By clamping the PM in the middle of the beam, the beam can be treated as two beams in parallel. Each of the beams is fixed at one end and free to translate at the other end. For very

32

small deflection, the beam can be considered as a linear system [43]. He [39] obtained an analytical model of the restoring force. However, the displacement of the PM results in both bending and axial stretching in the beam. In addition, the process of installation inevitably adds an initial tension to the beam. All these factors have influences on the total stiffness of the beam. Thus, an experiment is conducted to find the stiffness of the beams. Figure 2.24 shows the setup of the experiment. A dial gauge (KAR, 0.001') was used to measure the displacement of the PM and a force gauge (Rapala, 50lbs) was employed to obtain the restoring force of the beam.
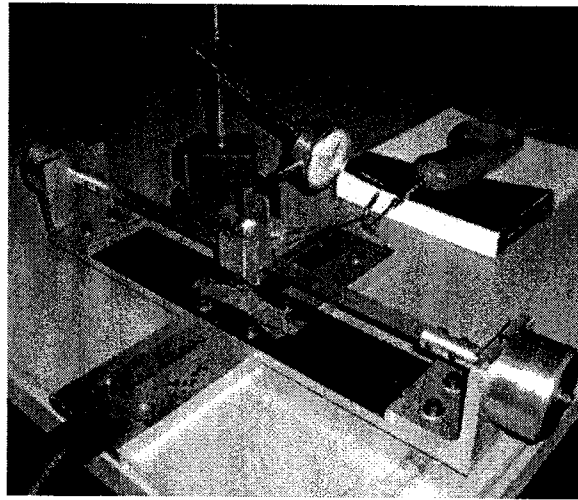
Figure 2.24   Experimental setup to measure the stiffness of the beam.

2.5.1   Highly nonlinear stiffness spring

A highly nonlinear beam is made of a steel ruler with length × width × thickness of 0.0320 × 0.0150 × 0.0005 m. With the beam firmly fastened in the beam support, an initial tension was applied to the beam. In order to obtain a highly linear stiffness, the initial tension should be as small as possible. Figure 2.25 demonstrates the experimental results. Through the Matlab built-in function "POLYFIT", the restoring force can be approximated as

$$F_b = 1.0385 \times 10^3 z + 3.4660 \times 10^7 z^3 \qquad (2.26)$$

where z is the displacement of the PM relative to the base. Equation (2.26) implies that the approximate stiffness of the beam around the equilibrium position is 1038.5 N/m.

33
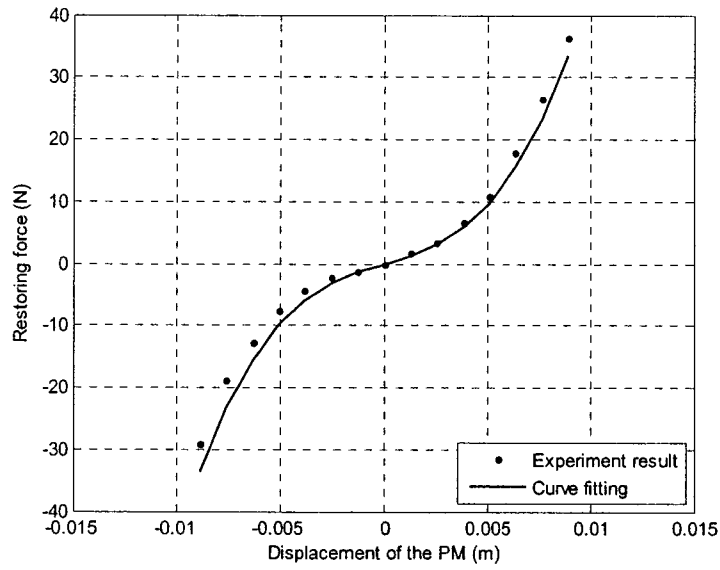
Figure 2.25 The restoring force of the beam versus the displacement of the PM.

2.5.2 Low nonlinear stiffness spring

A low nonlinear stiffness spring is made of a saw blade with length × width × thickness of 0.0280 × 0.0120 × 0.0006 m. Figure 2.26 demonstrates the experimental results.
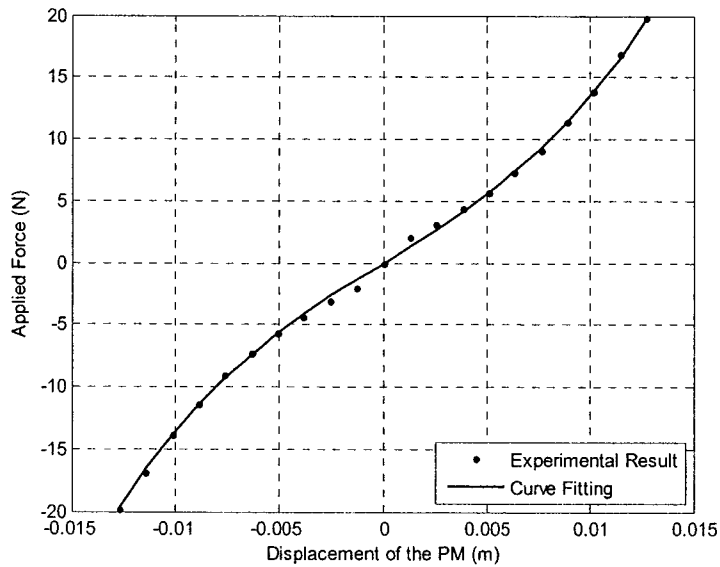
Figure 2.26 The restoring force of the beam versus the displacement of the PM.

Through the Matlab built-in function "POLYFIT", the restoring force can be approximately computed by:

$$F_b = 1.0385 \times 10^3 z + 3.1687 \times 10^6 z^3 \qquad (2.27)$$

It is noted that the approximate stiffness of the beam around the equilibrium position is 1038.5 N/m which is the same as that of the highly nonlinear beam. The stiffness curves of the highly nonlinear stiffness spring and low nonlinear stiffness spring are compared in Figure 2.27.
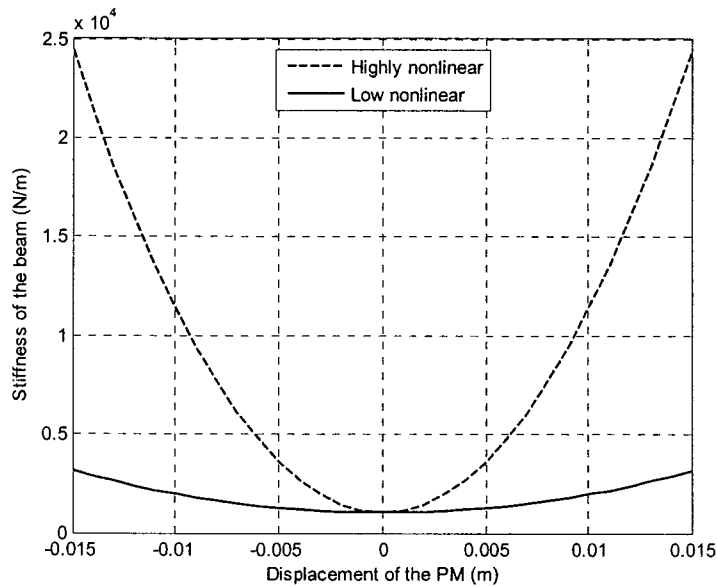
Figure 2.27   Comparison of two mechanical springs.

2.6   The Damping Coefficient of the Mechanical Spring

Damping is both difficult to model mathematically and difficult to measure. Choosing the correct form of damping is not an easy task. Hence it is often approximated as a linear dependence on velocity. A record of the displacement response of an under-damped system can be used to determine the damping ratio [1].

An experiment was set up to determine the logarithmic decrement. Figure 4.2 shows the setup for the experiment in which a laser sensor (Wenglor, CP24MHT80) was used to measure the displacement of the PM. The experiment result is shown in Figure 2.28. Through the Matlab function "FFT", the damping frequency of the beam is found to be 12.4 Hz, as shown in Figure

35

2.29. Due to the very small value of the damping ratio, the damped natural frequency of the beam is approximated to be the natural frequency.
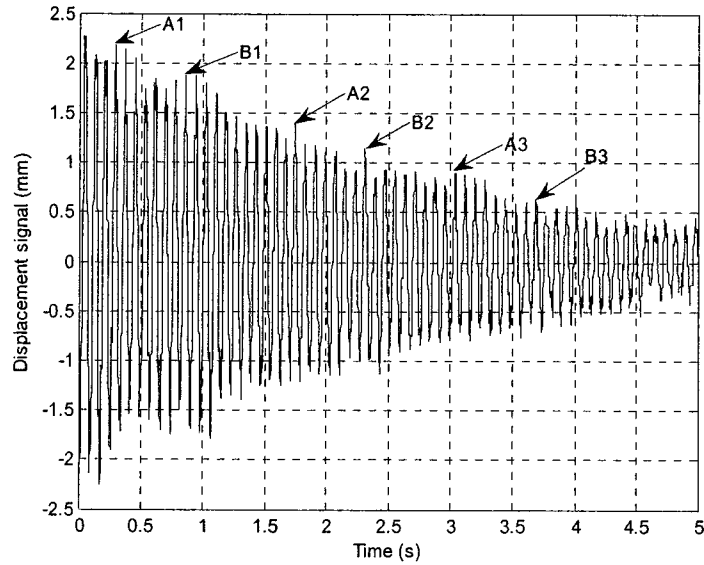
Figure 2.28   Response of the beam subjecting to an initial velocity.
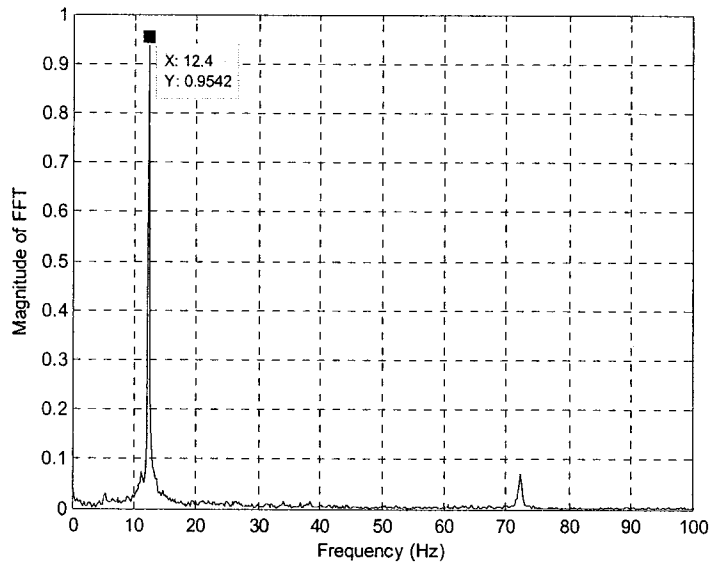
Figure 2.29   Spectrum of the response of the beam in FFT.

In order to get rid of the effect of a low frequency response, three set of points are selected to calculate the logarithmic decrement according to the equation [1]:

$$\delta = \frac{1}{n}\ln\left(\frac{z(t)}{z(t+nT)}\right)$$

The average of δ is found to be 0.031028. Thus, the damping ratio can be computed by:

$$\zeta = \frac{\delta}{\sqrt{4\pi^2+\delta^2}} = 4.9382 \times 10^{-3}$$

Thus, the damping coefficient is computed by;

$$c = 2m\zeta\omega_n = 0.13081\ Kg/s$$

2.7 The Combined System

2.7.1 A passive HSLDS isolator with the highly nonlinear stiffness spring
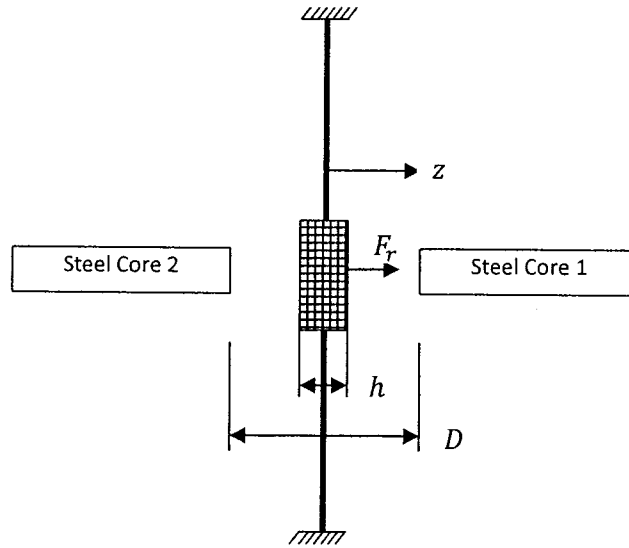
Figure 2.30 A passive HSLDS isolator.

Without the EM current, the system can be considered as a passive HSLDS isolator. Figure 2.30 shows the schematic of the system. The steel beam possesses a positive hardening stiffness. When the deflection of the beam is small, the natural frequency of the system is $\omega_n = \sqrt{k/m}$, where m is the mass of the PM and k is the stiffness of the beam. The effect of the two steel cores, both attracting the PM, is to produce a negative softening stiffness which can be made to counteract the positive stiffness of the beam. The static stiffness depends on the beam, while the dynamic stiffness comes from the combined effect of the beam and permanent magnet spring.

37

Using equations (2.10) and (2.26), the restoring force of the passive isolator with the strong nonlinear mechanical spring is given by

$$F_r = F_b + \Delta F_{pc}$$

$$= 1.0385 \times 10^3 z + 3.4660 \times 10^7 z^3 - 8a_1 q_1 \frac{z(q_1^2 + z^2)}{(q_1^2 - z^2)^4} \qquad (2.28)$$

Figure 2.31 demonstrates the restoring forces for four gap distances. It is noted that the smaller the gap distance, the softer the isolator spring.
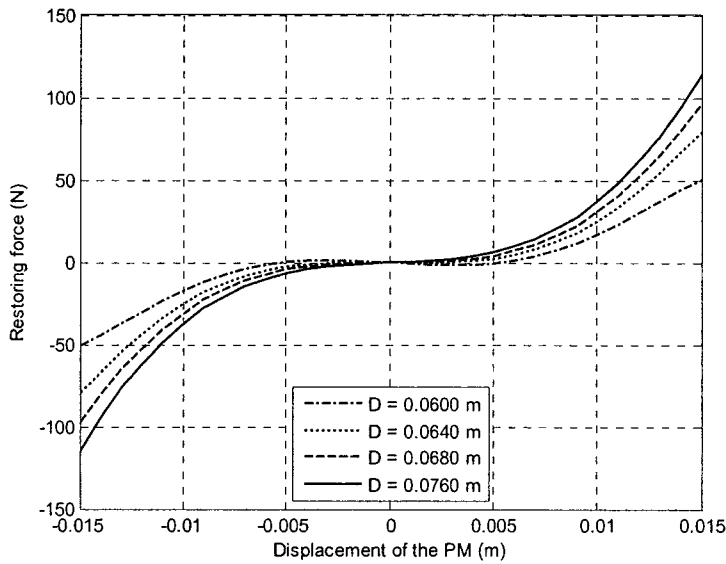
Figure 2.31   Applied force versus displacement.

From equation (2.28), the stiffness of the system is found to be:

$$k = 1.0385 \times 10^3 + 1.0398 \times 10^8 z^2 - 8a_1 q_1 \frac{5z^4 + 10q_1^2 z^2 + q_1^4}{(q_1^2 - z^2)^5} \qquad (2.29)$$

Figure 2.32 shows several stiffness curves with different values of the gap distance D. The figure indicates that the setup possesses the characteristic of a hardening spring, i.e., the stiffness increases with an increase of the beam deflection in the neighbourhood of the equilibrium position. Such a hardening effect is mainly due to the high nonlinearity of the beam.

With $D = 0.0670$ m, the dynamic stiffness is found to be 6.6845 N/m at the equilibrium position. Figure 2.33 demonstrates the curve of the dynamic stiffness versus the displacement of the PM when the gap distance is 0.0670 m. It can be observed that the dynamic stiffness increase

significantly when the PM moves away from the equilibrium position. In the other word, the natural frequency of the system increases when the vibration amplitude increases.
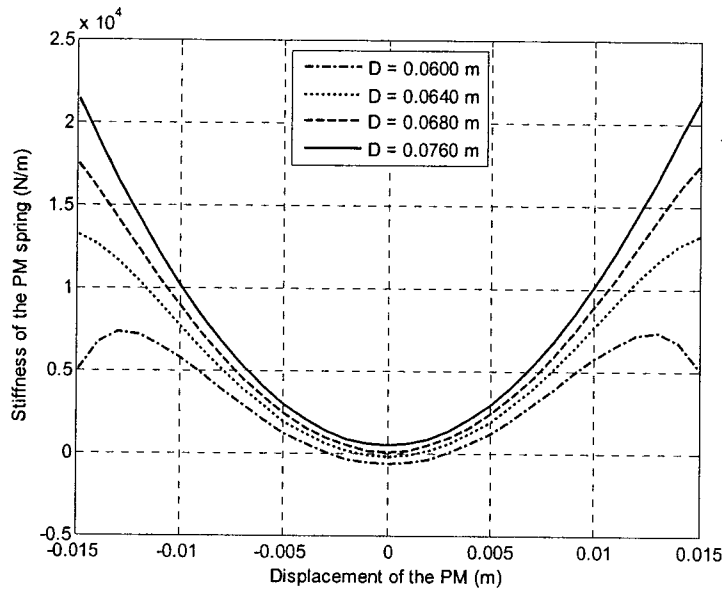
Figure 2.32   Dynamic stiffness of the isolator versus displacement of the PM.
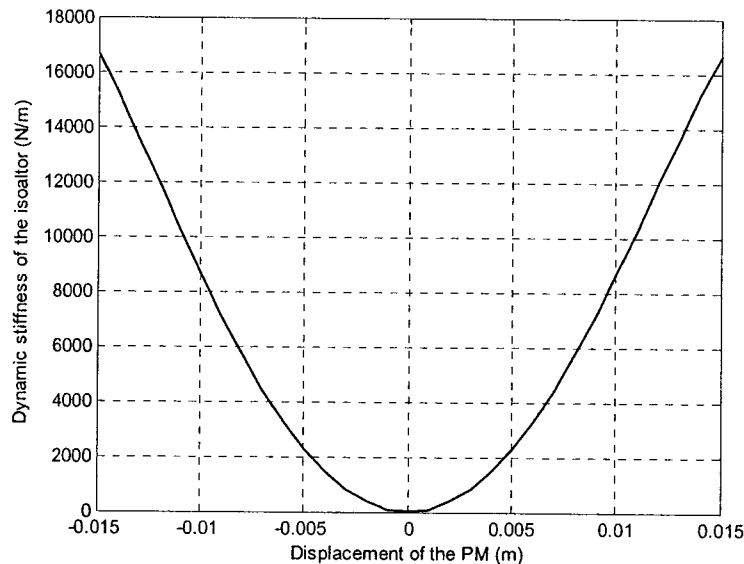
Figure 2.33   Dynamic stiffness of the isolator versus displacement of the PM when D = 0.0670 m.

2.7.2 A passive HSLDS isolator with the low nonlinear stiffness spring

In this section, a mechanical spring with the low nonlinear stiffness is connected to the PM spring in parallel. Using equations (2.10) and (2.27), the restoring force for a displacement z can be expressed as:

39

$$F_r = F_b + \Delta F_{pc}$$

$$= 1.0385 \times 10^3 z + 3.1687 \times 10^6 z^3 - 8a_1 q_1 \frac{z(q_1^2 + z^2)}{(q_1^2 - z^2)^4} \qquad (2.30)$$

The curve of restoring force vs. the displacement is shown in Figure 2.34 for several values of the distance D.
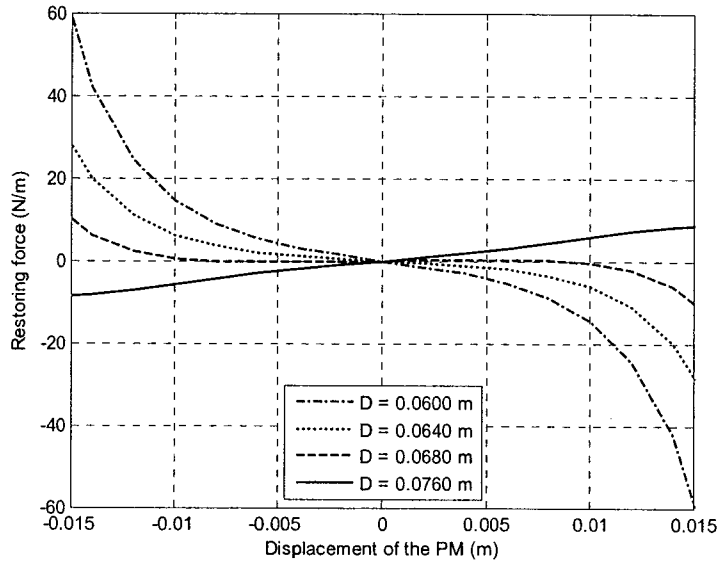
Figure 2.34   Restoring force versus the displacement of the PM.
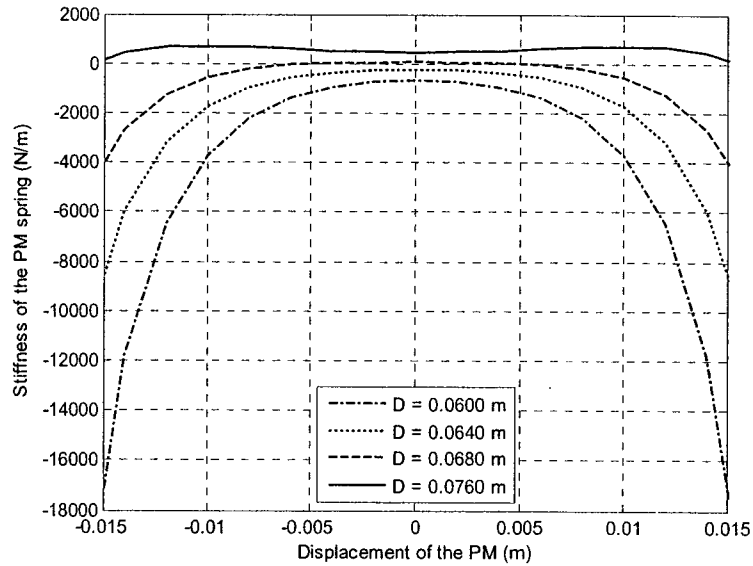
Figure 2.35   Dynamic stiffness versus the displacement of the PM.

From equation (2.30), the stiffness of the system is found to be

$$k = 1.0385 \times 10^3 + 9.5161 \times 10^6 z^2 - 8a_1 q_1 \frac{5z^4 + 10q_1^2 z^2 + q_1^4}{(q_1^2 - z^2)^5} \qquad (2.31)$$

Figure 2.35 shows several dynamic stiffness curves with different values of the gap distance D. The figure indicates that a too small gap distance will make the system unstable.

In the neighbourhood of the equilibrium position, the dynamic stiffness may have the hardening property or the softening property. The fluctuation of the stiffness should be small so that the displacement of the PM has less effect on the stiffness of the system. In this study, the desired region is defined as a region where the dynamic stiffness at any point cannot be 10% greater than or less than the one at the equilibrium point and the dynamic stiffness should be positive. The width of the desired region can be found by a numeric method. Figure 2.36 plots the relationship between the width of the desired region and the gap distance D between the two steel cores. It can be seen that the curve is unimode. It is found that the maximum width of the desired region is 0.0168 m when $D = 0.0715$ m.
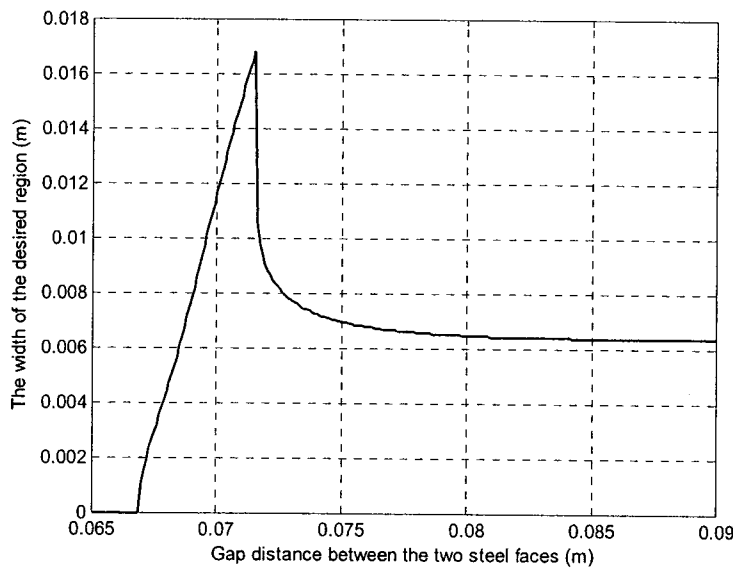
Figure 2.36 The width of the desired region versus the gap distance between the two steel cores

Figure 2.37 demonstrates the curve of the dynamic stiffness versus the displacement of the PM when the gap distance is 0.0715 m. Figure 2.38 shows the curve of the dynamic stiffness at the equilibrium position versus the gap distance between the two steel cores. From Figures 2.36 and 2.38, the following observations can be drawn. First, when the gap distance is bigger than 0.0715 m, the width of the desired region decreases and the dynamic stiffness at the equilibrium

41

point increases with an increase of the gap distance. This is not desirable. Second, there is a trade-off when the gap distance is less than 0.0715 m. An increase of width of the desired region results in an increase of the dynamic stiffness at the equilibrium position, therefore a high dynamic stiffness.
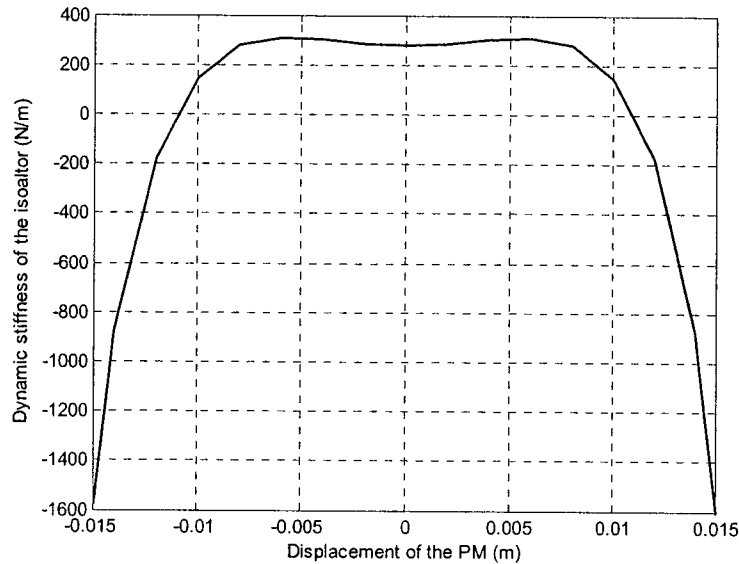
Figure 2.37   Dynamic stiffness versus displacement of the PM when D = 0.0715 m
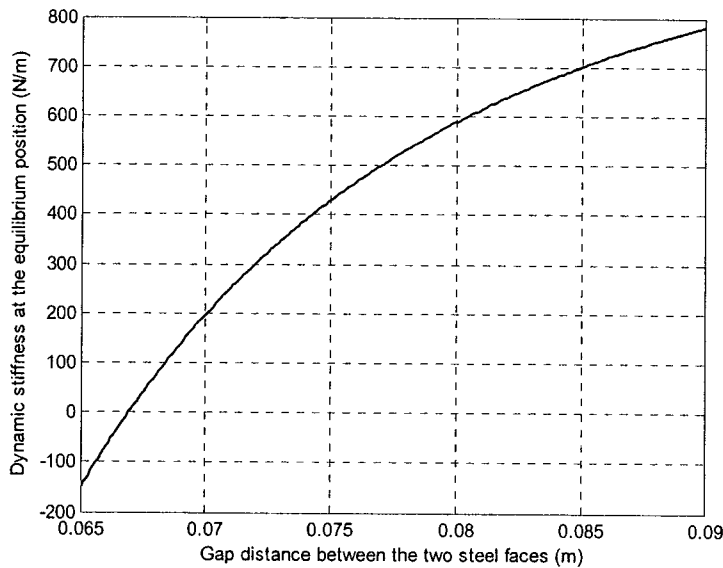
Figure 2.38   Dynamic stiffness at the equilibrium position versus gap distance between the two steel cores

Equation (2.31) describes the stiffness equation of the passive isolator. When the gap distance D is 0.0670 m, the dynamic stiffness is 6.6845 N/m at the equilibrium position, which

can be considered as quasi-zero stiffness. Figure 2.39 shows the curve of the dynamic stiffness versus the displacement of the PM. The curve indicates that the dynamic stiffness becomes negative when the PM moves away from the equilibrium position. Therefore, the system is not stable and this setup cannot work as quasi-zero stiffness isolator.
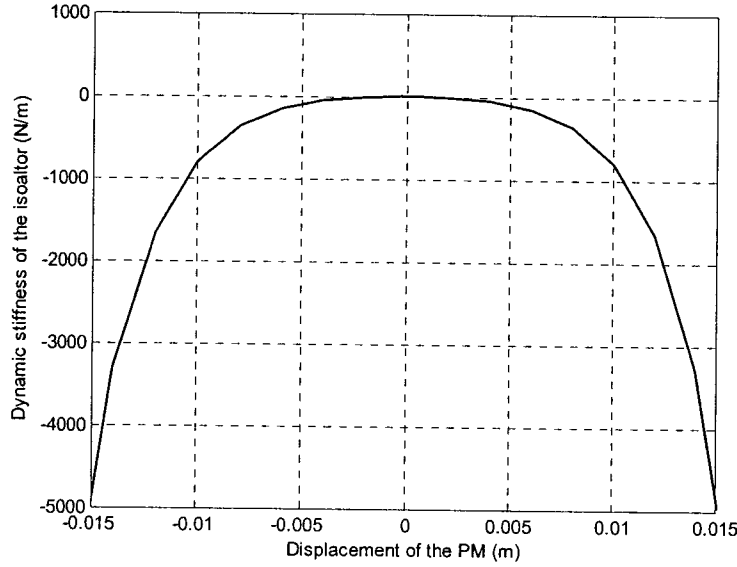
Figure 2.39   Dynamic stiffness versus displacement of the PM when D = 0.0670 m.

2.7.3 A tunable HSLDS isolator with the low nonlinear stiffness spring

When the PM-beam assembly is placed between the EMs as shown in Figure 2.40, the stiffness of the combined system can be tuned by adjusting the gap distance between the steel cores and the current in the EMs. In practice, the gap distance is not convenient to be changed after the system has been set up. With the EMs, it is a better way to improve the performance of the isolator by tuning the current in the EMs. Due to the ability of on-line tuning, the isolator is named as a tunable isolator. The restoring force of the system can be written as:

$$F_r = 1.0385 \times 10^3 z + 3.1687 \times 10^6 z^3$$

$$-8(1 - a_3|i|)a_1 q_1 \frac{z(q_1^2+z^2)}{(q_1^2-z^2)^4} - 8sign(i)(1 - e^{-b_3|i|})b_1 q_2 \frac{z(q_2^2+z^2)}{(q_2^2-z^2)^4} \qquad (2.32)$$

43
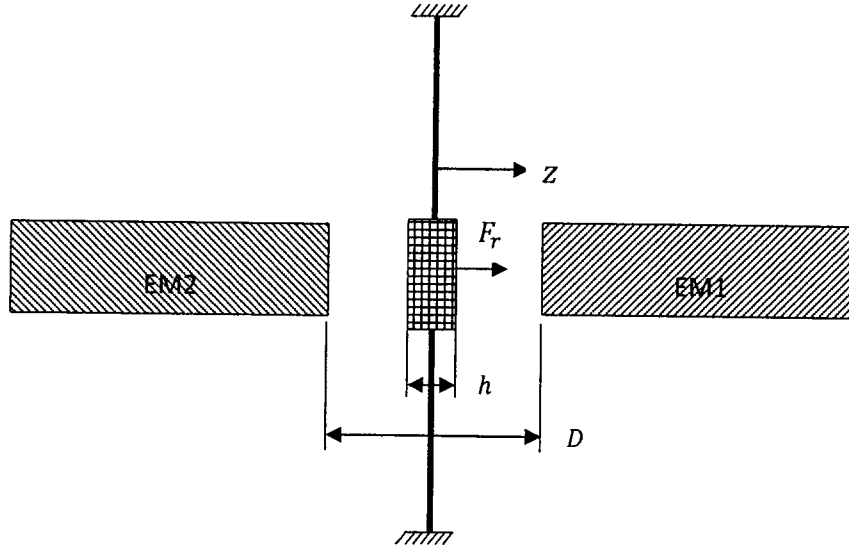
Figure 2.40   A tunable HSLDS isolator.

By differentiating equation (2.32) with respect to the PM displacement z, the dynamic stiffness of the system can be expressed as

$$k = 1.0385 \times 10^3 + 9.5161 \times 10^6 z^2 - 8(1 - a_3|i|)a_1 q_1 \frac{5z^4 + 10q_1^2 z^2 + q_1^4}{(q_1^2 - z^2)^5}$$

$$-8sign(i)(1 - e^{-b_3|i|})b_1 q_2 \frac{5z^4 + 10q_2^2 z^2 + q_2^4}{(q_2^2 - z^2)^5} \qquad (2.33)$$
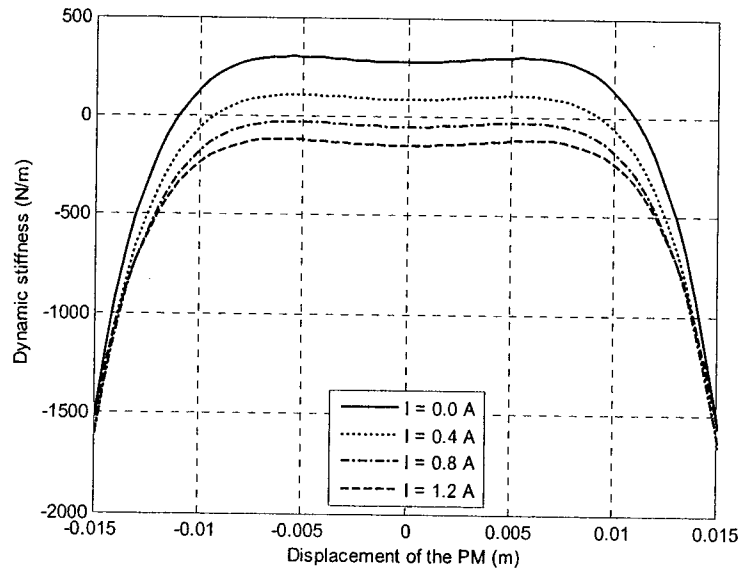
Figure 2.41   Dynamic stiffness versus displacement of the PM with distance 0.0715 m for several EM currents.

Figure 2.41 shows the stiffness curves for several values of the EM current when the gap distance is 0.0715 m, which is the optimum distance for the passive isolator discussed in Section 2.7.2. It is noted that the dynamic stiffness of the system can be changed after the gap distance D is fixed. In addition, with an increase of the EM current, the stiffness around the equilibrium position decreases.

Since two factors determine the stiffness curve of the system, an optimization design method is used to design the isolator. The design objective is to obtain a wider desired region and a lower positive dynamic stiffness at the equilibrium point. Figure 2.42 shows the width of the desired region as a function of the EM current and gap distance. Figure 2.43 demonstrates how both the EM current and the gap distance affect the dynamic stiffness of the isolator at the equilibrium position. The observation of these two figures indicates that the current in the EMs does not effectively affect the width of the desired region when the setup obtains the maximum width of the desired region, but the current always has an effect on the dynamic stiffness, especially when the gap distance between the two EMs is small. Therefore, the best choice to design the tunable isolator is to obtain the maximum width of the desired region by determining the gap distance first, and then tune the EM current to reach the desired stiffness.
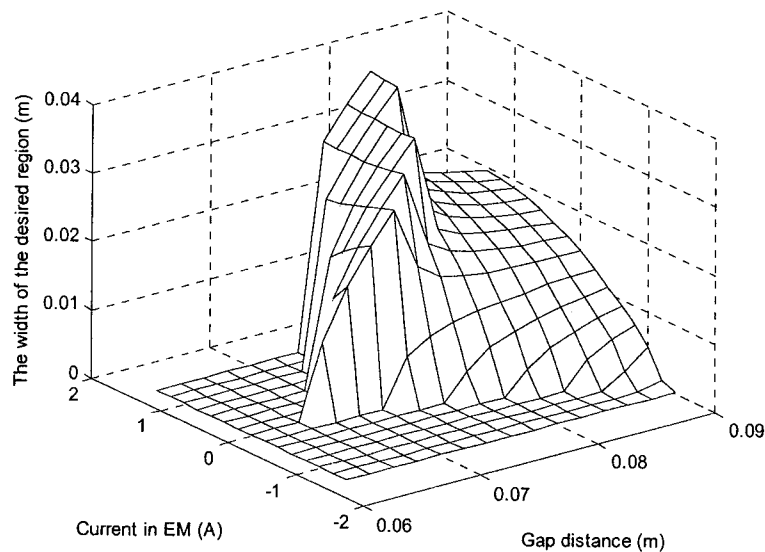
Figure 2.42   The width of desired region for different currents in the EM and the different gap distances.

45
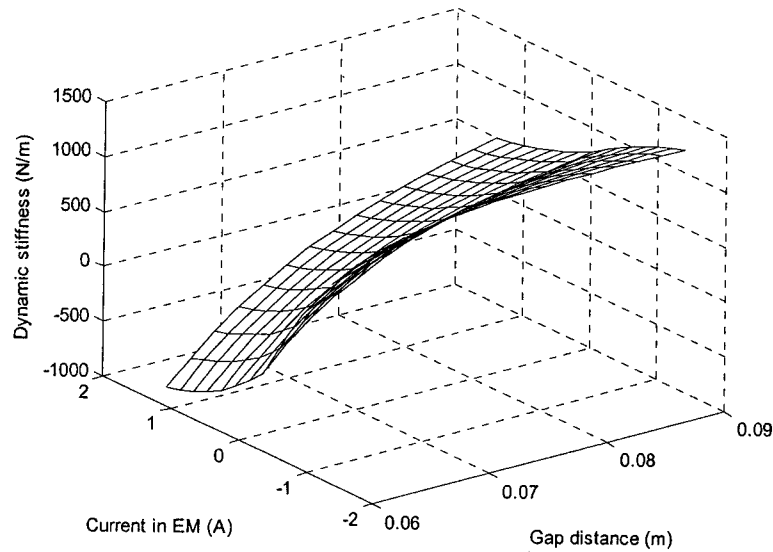
Figure 2.43 Dynamic stiffness for different currents in the EM and the different gap distances.

If an isolator possesses a very small dynamic stiffness, it is referred to as a quasi-zero stiffness isolator [3]. Section 2.7.2 mentioned that the dynamic stiffness of the passive isolator at equilibrium position can be quasi-zero by properly choosing the gap distance between the PM and the steel cores, but that setup is not stable in the neighborhood of the equilibrium position. With the tunable isolator, it is possible to realize the quasi-zero stiffness isolator by properly choosing both the current and the gap distance of the EMs. In this thesis, the isolator can be considered as a quasi-zero stiffness isolator when its dynamic stiffness is less than 10.0 N/m and greater than zero. Apparently it is desired to make the PM motion range as large as possible while the isolator remains the quasi-zero stiffness.

For this purpose, a Matlab program is used to find all the values of the current and the gap distance such that the stiffness at the equilibrium position is less than 10.0 N/m. The best combination is found to be the current 1.39 A and the gap distance 0.0748 m. With this configuration, the maximum desired region 0.0268 m is obtained and the stiffness at the equilibrium position is 0.04649 N/m. Figure 2.44 shows the curve of dynamic stiffness versus the displacement of the PM when the best combination is applied. The curve indicates that the dynamic stiffness at the equilibrium position is near to zero and the dynamic stiffness remains positive when the PM slightly moves away from the equilibrium position.

46
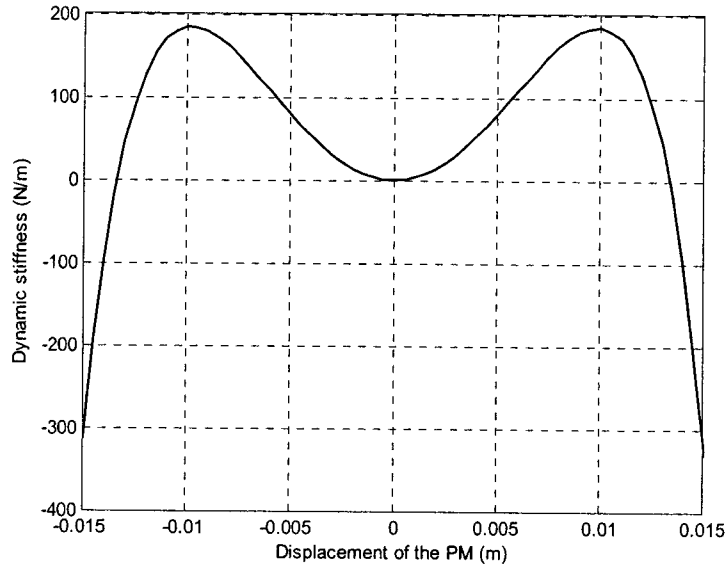
Figure 2.44   Dynamic stiffness versus displacement of the PM for a quasi-zero stiffness isolator.

2.7.4 Vibration analysis

A vibration analysis is conducted to study the response of the isolator to a base excitation. Due to the fact that a closed-form solution is not readily available for a nonlinear differential equation [1], a numerical integration is employed to solve the following equation of motion:

$$m\ddot{z} + c\dot{z} + f(z) = -m\ddot{y} \tag{2.34}$$

where z is the PM's displacement relative to the base, y is the base motion and $f(\cdot)$ is the restoring force defined by equation (2.26), (2.28), (2.30) and (2.32), respectively. Note that equation (2.26) defines the stiffness of the highly nonlinear beam, equation (2.28) defines the stiffness of the highly nonlinear beam plus the PM spring with $D = 0.0670$ m, equation (2.30) defines the low nonlinear beam plus the PM spring with $D = 0.0715$ m, and equation (2.32) defines the combined system with the quazi-zero stiffness. They are referred to as systems 1, 2, 3, and 4, respectively.

Assume that the isolator is subjected to a base excitation that is harmonic

$$y(t) = Ysin(\omega_b t) \tag{2.35}$$

47

where Y and ω_b denotes the amplitude and frequency of the base motion, respectively. Equation (2.36) describes the relationship among x, y and z.

$$z = x - y \qquad (2.36)$$

where x is the PM displacement relative to the ground; y is the base motion and z is the PM displacement relative to the base.

Substitution of equation (2.35) and equation (2.36) into equation (2.34) yields

$$m\ddot{x} + c\dot{x} + f(x - Y\sin(\omega_b t)) = cY\omega_b\cos(\omega_b t) \qquad (2.37)$$

Defining the state variables $(x_1, x_2) = (x, \dot{x})$, equation (2.37) can be written in the form:

$$\begin{cases} \dot{x}_1 = x_2 \\ \dot{x}_2 = -\dfrac{c}{m}x_2 - \dfrac{f(x_1 - Y\sin(\omega_b t))}{m} + \dfrac{cY\omega_b\cos(\omega_b t)}{m} \end{cases} \qquad (2.38)$$

where x_1 is the displacement of the PM relative to the ground, x_2 is the velocity of the PM relative to the ground, the mass $m = 0.17\ kg$ and the damping coefficient $c = 0.13081\ kg/s$. A Matlab function, ODE45, is used to solve equation (2.38) with the different restoring forces.

Figure 2.45 shows the time responses of the isolator when the amplitude of the base motion was 0.0010 m, the frequency was 10 Hz and the initial conditions were zero. It is noted that the system is in the steady state after 20 seconds. By varying the excitation frequency, the curves of the transmissibility ratio versus the excitation frequency are obtained as shown in Figure 2.46. The figure indicates that a low dynamic stiffness extends the isolation region and reduces the amplitude of the steady state response. The curves of the systems 1 and 2 exhibit a typical behaviour of nonlinear system: the response amplitude undergoes a sudden discontinuous jump near resonance [44]. The frequency at which the response amplitude jumps is referred to as the jump frequency. The jump frequency not only depends on the system itself, but also the amplitude of the excitation signal and initial conditions. Figure 2.47 shows the displacement transmissibility ratio as a function of the excitation frequency when the amplitude of the excitation displacement is 0.0005 m.
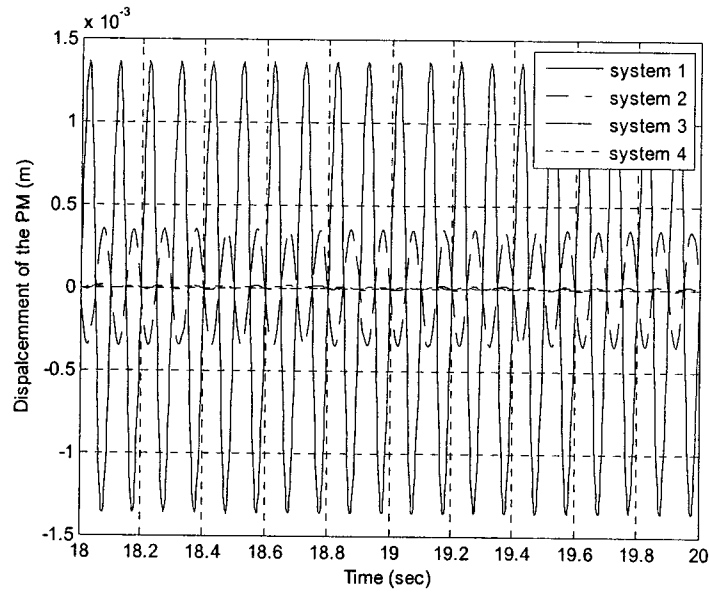
Figure 2.45   Responses of four isolation systems when base motion frequency is 10 Hz and Y =0.0010 m.
1), highly nonlinear beam; 2), highly nonlinear beam and the PM spring;
3), low nonlinear beam and the PM spring; 4), quasi-zero stiffness isolator
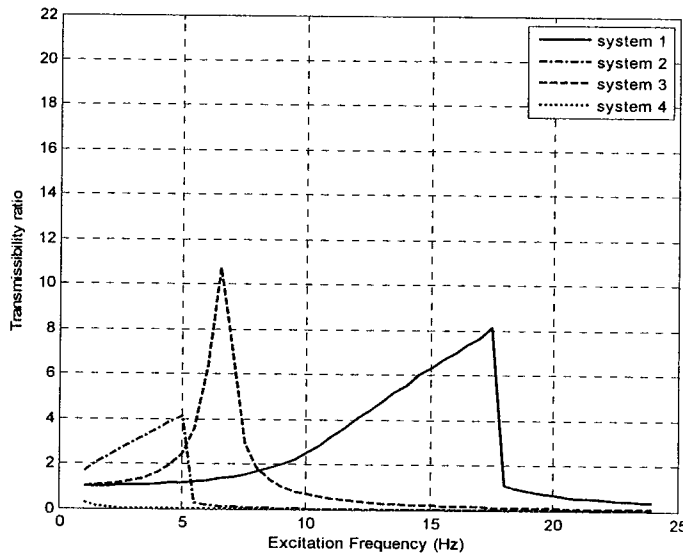
Figure 2.46   Displacement transmissibility ratio as a function of the excitation frequency, when Y=0.0010 m
1), highly nonlinear beam; 2), highly nonlinear beam and the PM spring;
3), low nonlinear beam and the PM spring; 4), quasi-zero stiffness isolator.

49
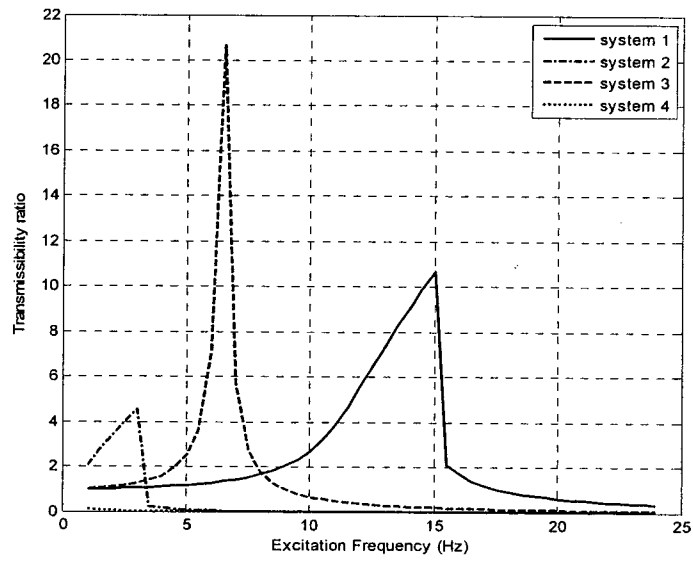
Figure 2.47   Displacement transmissibility ratio as a function of the excitation frequency, when Y=0.0005 m
1), highly nonlinear beam; 2), highly nonlinear beam and the PM spring;
3), low nonlinear beam and the PM spring; 4), quasi-zero stiffness isolator.

Chapter 3.   Comsol Multiphysics Simulation

In this chapter, a commercial package, Comsol Multiphysics, is used to characterize the tunable isolator. The intention is to compare the results from Comsol simulation with those from the experiments.

3.1   Description of the Model

The model created in Comsol Multiphysics is shown in Figure 3.1. A PM is placed in between a pair of the EMs, and the assembly is surrounded by a typical cylinder infinite elements. In order to reduce the amount of mesh elements, only 1/180 of the EM-PM-EM assembly is modeled. The model is built in AC/DC Model>Statics>Magnetostatics mode.
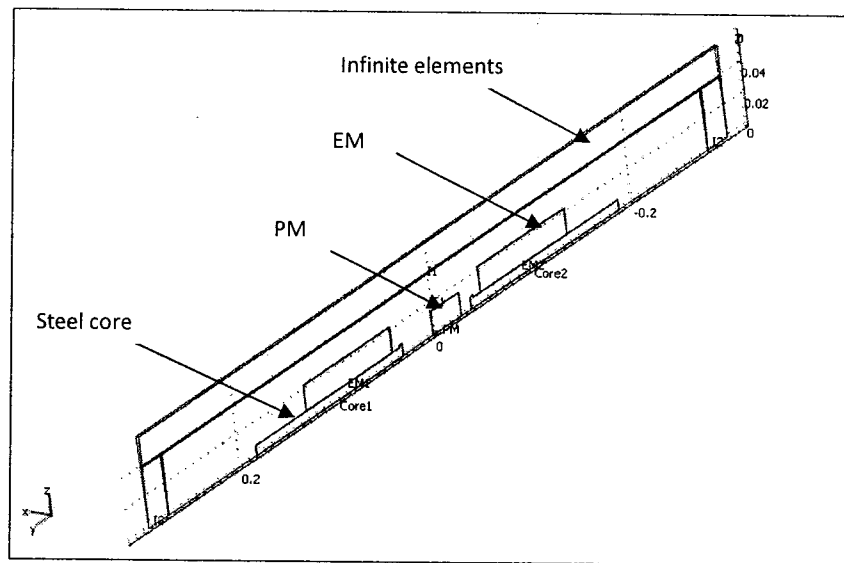
Figure 3.1   A 1/180 of EM-PM-EM assembly surrounded by a typical cylinder infinite element region.

3.1.1   Infinite elements

In theory, the magnetic field is unbounded and should extend toward infinity. A traditional approach is just to extend the simulation domain far enough and then consider the magnetic field is bounded [39]. The boundary condition at the far end has negligible influence on the

51

simulation. This approach can create a large amount of unnecessary mesh elements and increase the computation burden. Another approach is to use "infinite elements". This implementation maps the model coordinates from the local, finite sized domain, to a stretched domain. The inner boundary of this stretched domain is coincident with the local domain, but at the external boundary the coordinates are scaled towards infinity [45].

3.1.2 Permanent magnet

The PM used in this study consists of two square-shape permanent magnets. The assembly can be considered as one square-shape PM with a dimension of $0.0254 \times 0.0254 \times 0.0290$ m (length $\times$ width $\times$ thickness). In the Comsol simulation, this square-shape PM is approximated as a round-shape PM [38]. The two pair of steel fasteners that is used to embed the PM in the middle of the beam has an interaction with the EMs. The number of meshed elements in the PM pole face has been reduced due to the small size of the model. Taking these factors into account, an increase of the PM cross-sectional area is used to calibrate the interaction force. By modifying the square pole face of the PM to a round shape face with a radius 0.0154 m, the flux density along the center line (z-axis) from the Comsol simulation is close to the one from the experiment as shown in Figure 3.2.
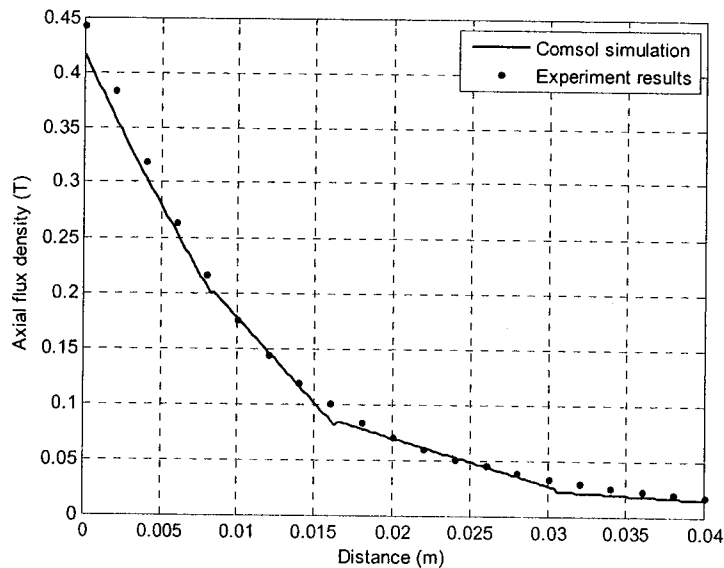
Figure 3.2   Magnetic flux density along the centerline of the PM with the origin located at the center of the pole face.

3.1.3 Steel core

In the actual apparatus, a screw is used to fasten the coils to the steel core. The interaction force between the screw and the PM cannot be neglected especially when the distance is very small. In order to simplify the simulation, the shape of the steel core has been modified as shown in Figure 3.3. The shoulder at the end of the core is used to represent the screw on the steel core. The relative permeability of the core is found in Table 3.1 in Section 3.2.
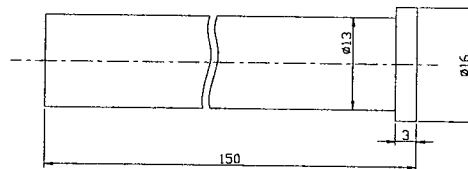
Figure 3.3 A modified steel core.

In the Comsol simulation, when changing the distance between the PM and the steel core, the curve of the relationship between the attracting forces and the distances is obtained. Comsol Multiphysics 3.4 provides the "Solver Manager" dialog to help users control the solution process. Comsol scripts can be used to compute the solution when the "solver using a script" check box in the "Script" tab is selected. The scripts used in this section include a loop that calculates the magnetic force acting on the steel core for each different gap distances. Figure 3.4 presents the comparison of Comsol simulation results and experiment results.
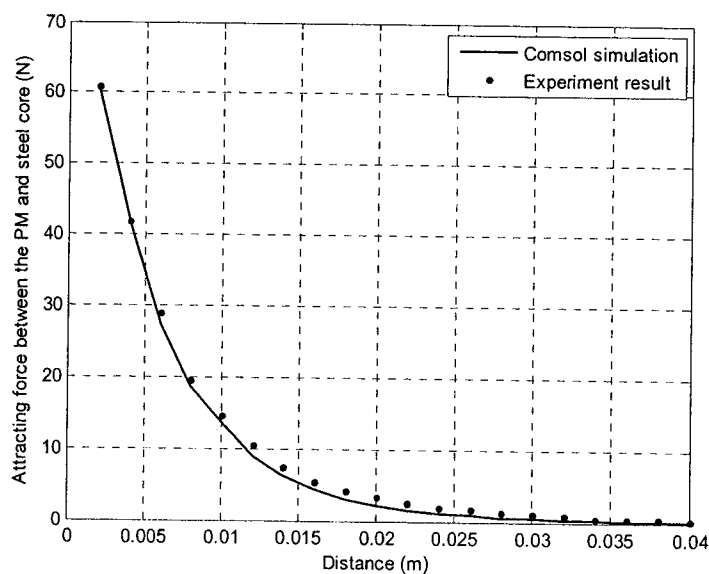
Figure 3.4 Attracting force acting on the steel core versus the distance between the PM and steel core.

3.1.4 Electromagnet

The EM coil is modeled as a hollow cylinder which is considered to be an acceptable simplification of the real coil [39]. The cylinder carries a current in the circular direction on the transverses cross section of the hollow cylinder. The magnitude of the current density that flows in the cross section of the cylinder is approximated to be the one in each turn.

$$J_0 = \frac{I}{\pi r^2} \tag{3.1}$$

where J_0 is the magnitude of the current density, I is the current in the EM and r is radius of Gauge 22 copper wire used in the actual coil. The x component of the current density is (the coordinate system is defined in Figure 3.1)

$$J_x = \frac{J_0 z}{\sqrt{x^2 + z^2}} \tag{3.2}$$

and the z component is

$$J_z = \frac{J_0 x}{\sqrt{x^2 + z^2}} \tag{3.3}$$

Figure 3.5 demonstrates the axial magnetic flux density from the EM versus the axial displacement along the centerline.
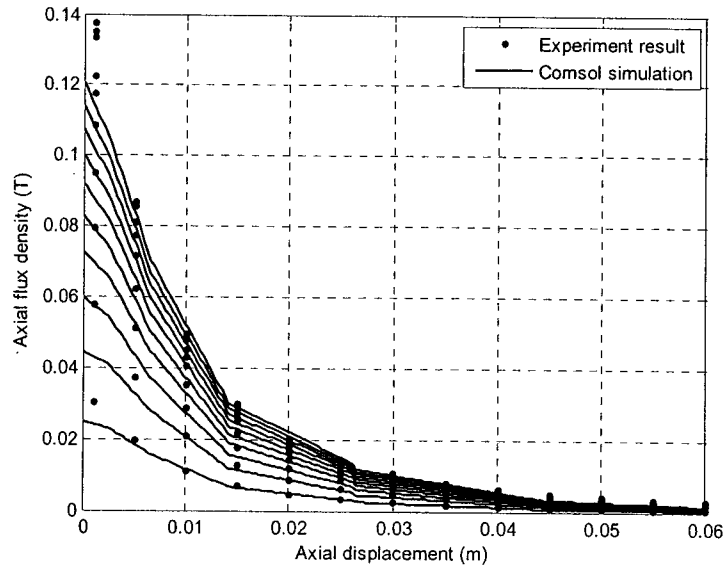
Figure 3.5   The axial magnetic flux density from the EM along the centerline.

3.2 Study of Relative Permeability

The ability of a material to become magnetized is called magnetic permeability. Substances with higher permeability will become more easily magnetized than that of lower permeability. All substances, even air, have a degree of magnetic permeability. The air in a vacuum, also called free space, has a constant value which is called the magnetic constant. This value is represented by the symbol μ_0 and is valued as $4\pi \times 10^{-7}$ H/m. The ratio of the permeability of a specific medium to the permeability of the free space is defined as relative permeability, sometimes denoted by the symbol μ_r.

When placed near a PM, a ferromagnetic material becomes magnetized and be attracted by the PM. Many factors, including the permeability of the ferromagnetic material, have effects on the attracting force between the PM and the ferromagnetic material. A Comsol simulation is conducted to study how the relative permeability affects the attracting force between the PM and the steel core.

Since only 1/180 of the PM and steel core is modeled, the actual force is 180 times the result from Comsol simulation [46]. The model shown in Figure 3.1 was used here. The gap distance between the left EM and the PM was 0.0020 m. The EM current was set to zero and the right EM was disabled. Figure 3.6 demonstrates how the permeability of the steel core has an influence on the attracting force. The figure indicates that the attracting force is very sensitive to the relative permeability of the steel core if the relative permeability is less than 400.0. Thus, it is important to determine the relative permeability of the steel core in different operating conditions. The relative permeability is not a constant figure. Rather, it changes with the position of the material in relation to the magnetic field, the frequency of the field, humidity, temperature, and other factors. The techniques [34, 41] to determine the relative permeability are beyond the scope of this study. The change of the current in the EM changes the magnetic field and temperature in the steel cores. In order to simplify the computation, only the relationship between the relative permeability and current is considered in this study. Given a certain distance, measure the interacting force between the PM and the EM for different currents in the EM. And then, adjust the relative permeability of the steel core in the Comsol model to make the interaction force fit the experiment results. Figure 3.7 illustrates the curve of the attracting force versus the current.
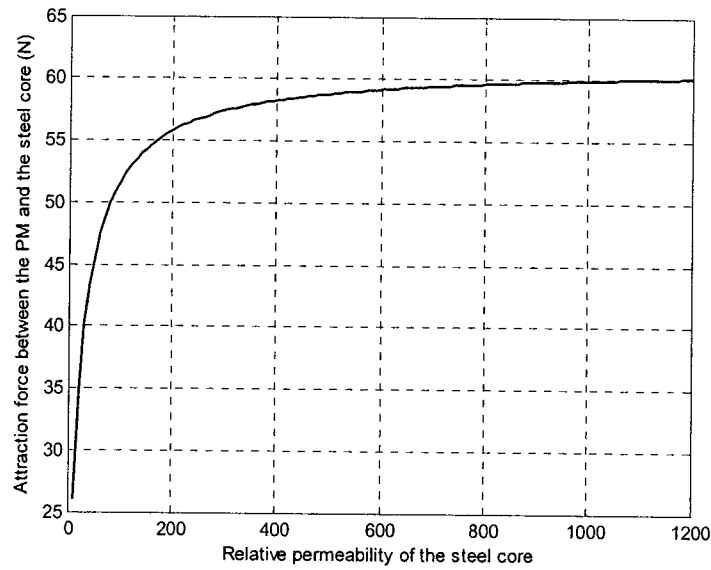
Figure 3.6   The attracting force versus the relative permeability with a gap distance 0.0020 m.
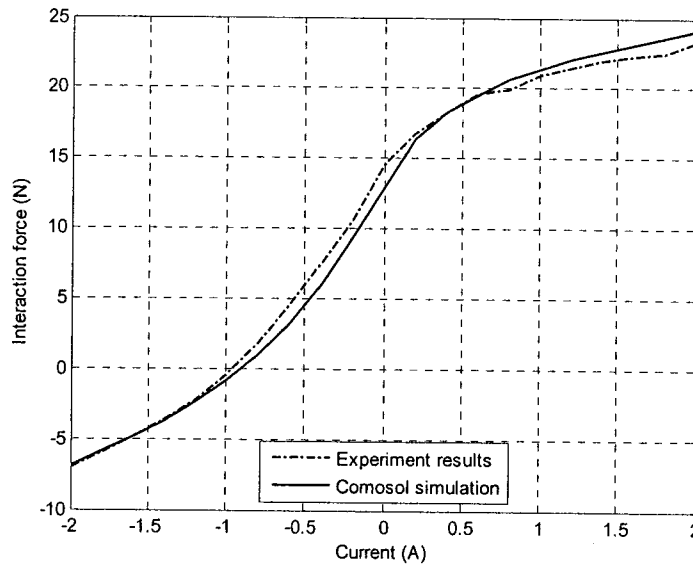
Figure 3.7   The attracting force versus the EM current when the gap distance is 0.0100 m.

The relative permeability corresponding to a certain current is presented in Table 3.1. The table is used to define a function to determine the relative permeability of the steel core through interpolation method in Comsol model. It is noted that the relative permeability of the steel core decreases with an increase of current in the EM.

Table 3.1   The relative permeability of steel core versus the current in the EM.

Current (A)	Relative Permeability
0.0	450.0
0.2	350.0
0.4	150.0
0.6	89.6
0.8	64.5
1.0	49.0
1.2	40.0
1.4	33.6
1.6	29.0
1.8	25.5
2.0	23.0

3.3   Simulation of the Interaction Force between the PM and the EM

The interaction force between the PM and the EM consists of two parts: the interaction between the PM and the steel core which was discussed in Section 3.1.3 and the interaction between the PM and the electronic coil. Figure 3.8 shows the simulation results.
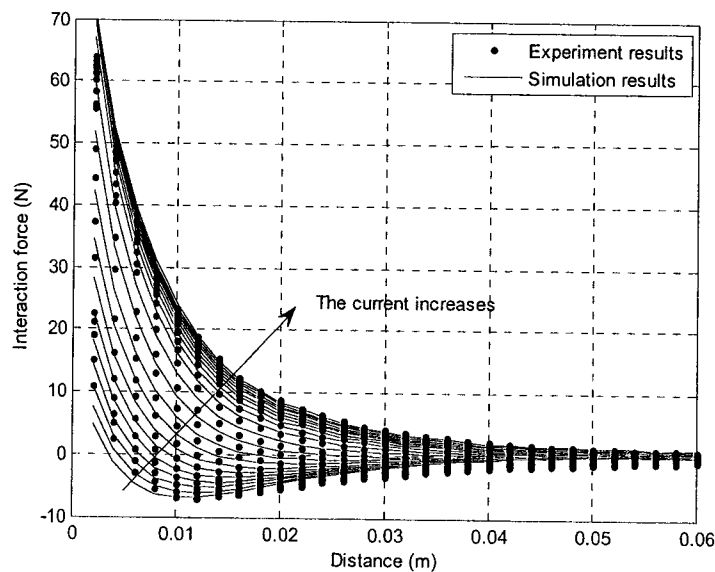
Figure 3.8   Interaction force versus the distance between the EM and PM with current varying from -2.0 A to 2.0 A.

In comparison with the experiment results, the Comsol simulation underestimates the interaction force when the gap distance increases. In practice, the relative permeability of the steel core increases when the PM moves away from the EM. In this simulation, the effect of the distance between the PM and EM was neglected and only the current was taken into consideration.

3.4 Simulation of the Electromagnetic Spring

When the PM is placed in the gap of the EMs shown in Figure 3.1, the EM-PM-EM assembly can be considered as an electromagnetic spring. By placing the PM on different locations in the gap, the relationship between the magnetic force and the PM displacement is obtained. From this relationship, the stiffness is found.

Both the gap distance between the two EMs and the EM current determine the stiffness of the EM spring. Figure 3.9 shows how the gap distance affects the stiffness of the spring and Figure 3.10 demonstrates how the current in the EMs has an effect on the stiffness of the spring. It is observed that an increase of the gap distance makes the PM spring stiffer and reduces the softening property. With an increase of the EM current, the stiffness of the EM spring decreases and the softening property increases.
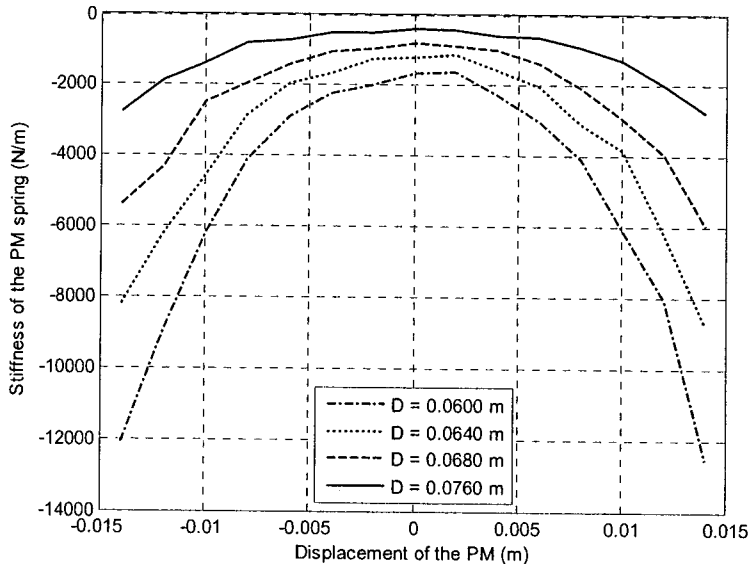
Figure 3.9   Stiffness of the magnet spring with different gap distances with no current in the EMs.
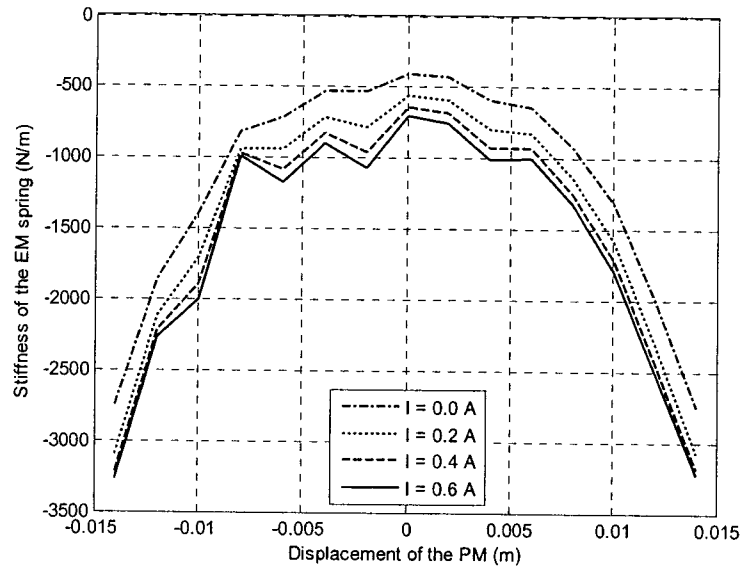
Figure 3.10   Stiffness of the magnet spring with different currents in the EMs when the gap distance is 0.0760 m.

3.5   Simulation of the Mechanical Spring

The beam with high nonlinearity is concerned in this section. Since the elastic modulus of the beam is very high, the axial force causes the beam supporter to bend upward before the beam has a large deformation. The plane stress mode from the structural mechanics module is employed to create a model to simulate the beam. The model is shown in Figure 3.11, and Figure 3.12 compares the experiment results and simulation results. In this simulation, an initial tension of 8 Mpa is applied to the beam model.
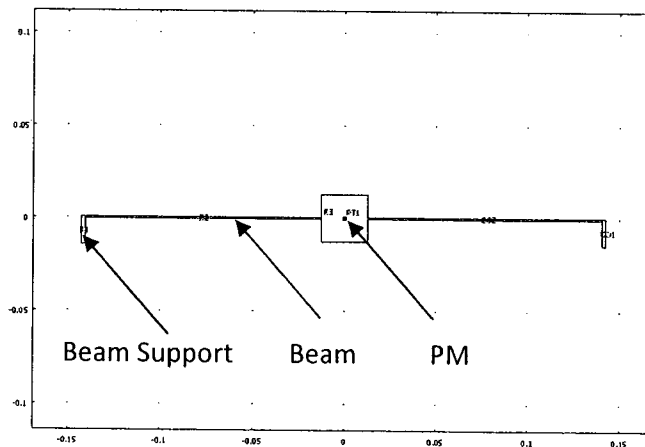
Figure 3.11   A model of positive spring.

59
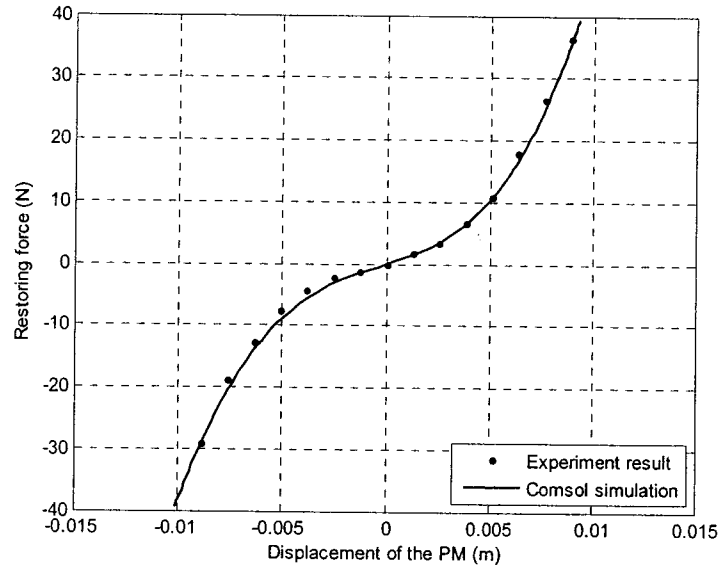
Figure 3.12   Restoring force versus the PM displacement.

When the beam is installed in the supports, it always has an initial tension in it. An initial tension in the beam definitely affects the stiffness of the beam and the hardening property. A Comsol simulation compares the stiffness of the beam with different initial tension in the beam. The results are shown in Figure 3.13. It is found that the stiffness of the beam increases but the harden property of the beam decreases with an increase of the initial tension in the beam.
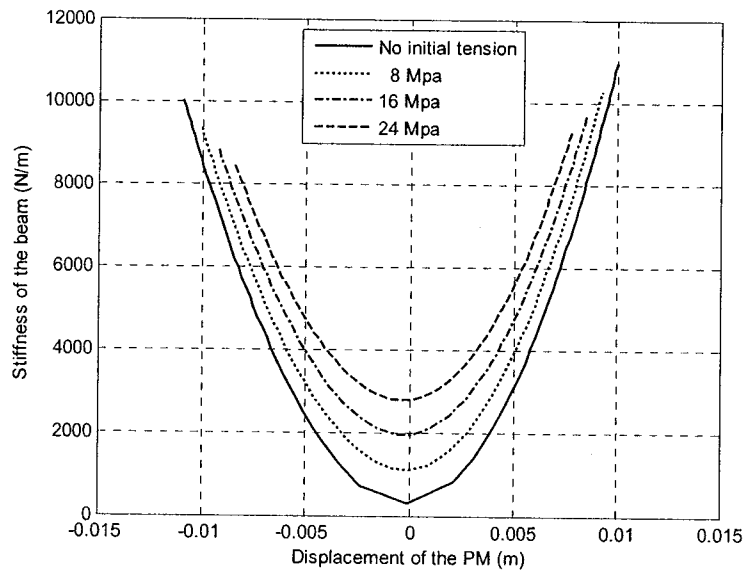
Figure 3.13   Stiffness of the beam versus the PM displacement with different initial tension.

3.6 Simulation of the Tunable Isolator

As shown in Figure 3.14, the stiffness of the tunable isolator is composed of three parts: the spring k_b created by the beam, the spring k_p formed by the interaction between the PM and steel core and the spring k_e generated by the interaction between the PM and the EMs. The value k_b is adjusted by the tension in the beam, length and thickness of the beam. The value k_p is determined by the gap distance between the steel cores, and the value k_e varies with the current in the EMs. Note that the net magnetic force acting on the PM behaves in the following way. When the PM is located exactly in the middle of the gap between the EMs, the net magnetic force is zero. When the polarities of the left and right EMs is the same as the ones shown Figure 3.14 and the PM moves left, the net magnetic force acts leftward, which corresponds to a negative magnetic stiffness. When the polarity of the left and right EMs changes to opposite and the PM moves left, the net magnetic force acts rightward, which corresponds to a positive magnetic stiffness.
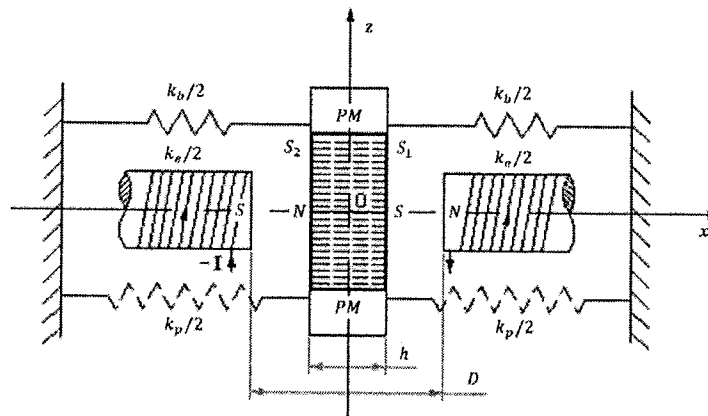
Figure 3.14   Three springs involved in the tunable isolator.

One of the Comsol Multiphysics' capabilities is to simulate multiphysics applications—those with more than one type of physics or equations such as coupled-field problems. In such a model, the software can solve all the equations, taken from various areas of physics, as one fully coupled system. Due to limitation of 32bits computer operation system, a "weakly coupled" way of solving a coupled multiphysics model is employed in this study. This method solves for one type of physics at a time and then use that solution as the initial value when solving for the other type of physics.

As shown in Figure 3.15, the applying force F which moves the PM to a displacement z is the subtraction of the net magnetic force F_m and restoring force F_b:

$$F = F_m - F_b \tag{3.4}$$

Both F_m and F_b depend on the displacement of the PM. Given a certain restoring force of the beam F_b, the displacement of the PM z is obtained through Structural Mechanics module. With the displacement of the PM, the F_m can be calculated by AC/DC module. And then, the applying force F is found through Equation (3.4) for the displacement z. Finally, the curve of the applying force F versus the displacement z of the PM is obtained as shown in Figure 3.16. Figure 3.17 demonstrates the stiffness of the isolator. It can be seen that, in the neighbourhood of the equilibrium position, the stiffness is very small.
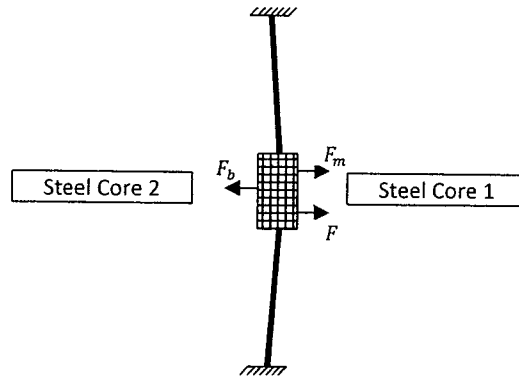
Figure 3.15   Free body diagram of the PM in the isolator.
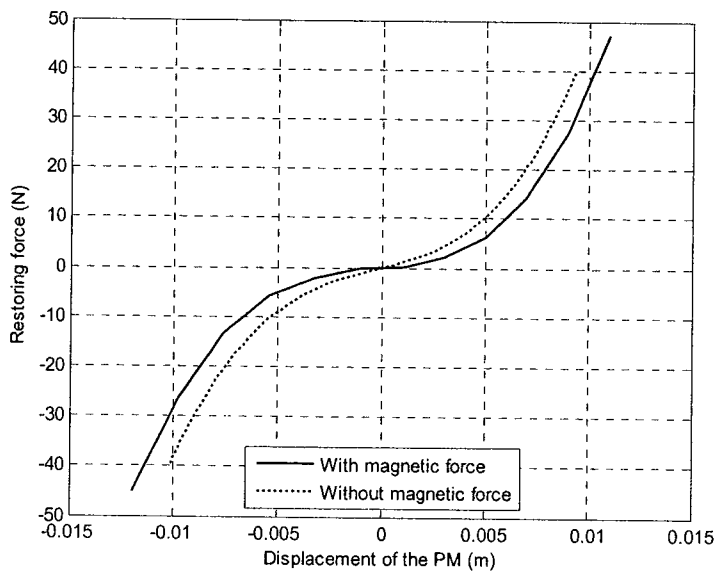
Figure 3.16   Restoring force versus displacement of the PM with gap distance 0.0760 m and current 0.6 A.

62
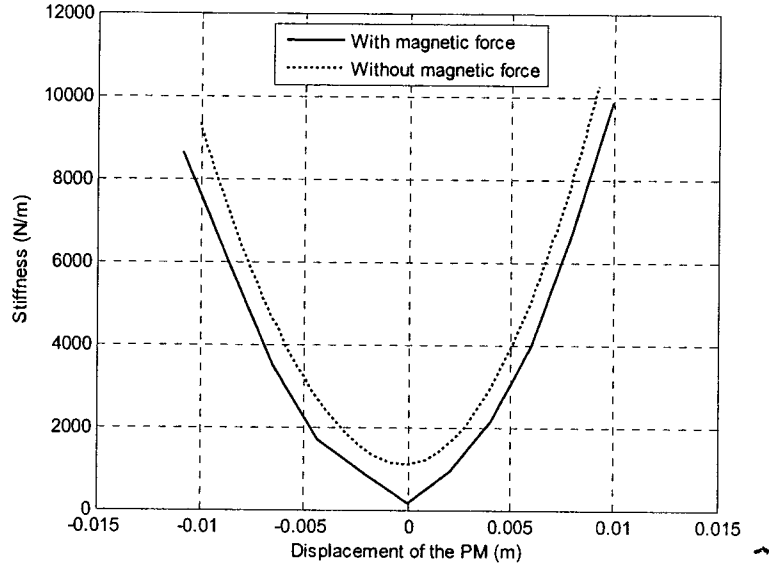
Figure 3.17   Dynamic stiffness versus displacement of the PM with gap distance 0.0760 m and current 0.6 A.

3.7 Vibration Analysis

An alternative way to solve this coupled system is to consider the magnetic force as a function of displacement, and then apply the force function on the PM in the Structural Mechanics module. Thus, the multiphysics application is changed to a single-physics application.

Section 3.6 has already obtained the relationship between the magnetic force and the displacement of the PM when the gap distance between the two EMs is 0.0760 m and the EM current is 0.6 A. By the curve fitting method, the magnetic force function can be written as:

$$F_t = \begin{cases} -2.9764 \times 10^3 (z + 0.0150) + 23.7 & z < -0.0150 \\ -7.1332 \times 10^2 z - 3.8423 \times 10^6 z^3 & -0.0150 \le z \le 0.0150 \\ -2.9764 \times 10^3 (z - 0.0150) - 23.7 & z > 0.0150 \end{cases}$$

With applying this magnetic force function on the PM in the Structural Mechanics module, the simple physics model can represent the coupled model.

In this study, the response of the PM is of interest. The isolator can be simplified as a lumped mass system. Therefore, it will be more effective to use the Structural Mechanics module to solve an ordinary differential equation (ODE) rather than solve a partial differential equation (PDE). The equation of the motion of the isolator is defined in equation (2.34). The base

63

excitation is defined in equation (2.35). The global equations dialog box in the Structural Mechanics module is used to import equation (2.37) to Comsol Multiphysics and then the time-dependent solver is employed to solve the equation.

Figure 3.18 shows the steady state responses of the isolator when the amplitude of the base motion was 0.0010 m, the frequency was 60 Hz and the initial conditions were zero. It is observed that the system is in the steady state after 16.0 seconds. By varying the excitation frequency, the PM response for each excitation frequency was obtained. Comsol scripts are used to retrieve the local peak values of the steady state response in the interval [16 20] s. The r.m.s of these peak values is considered as the amplitude of the steady state response. The curves of the displacement transmissibility ratio versus excitation frequency are obtained as shown in Figure 3.19. As indicated in Section 2.7.4, the amplitude of the base excitation has an effect on the displacement transmissibility ratio curve. Figure 3.20 shows the curve when the amplitude of the excitation displacement is 0.0020 m. From Figure 3.19 and Figure 3.20, it is observed that the tunable isolator has a larger isolation region. In addition, the system 1 defined in Figure 2.52 and the system 1 defined in Figure 3.19 represent the same system that is composed of only the highly nonlinear beam. Comparison of the transmissibility ratios in two figures indicates that the results from Comsol simulation agree with the results from the Matlab simulation.
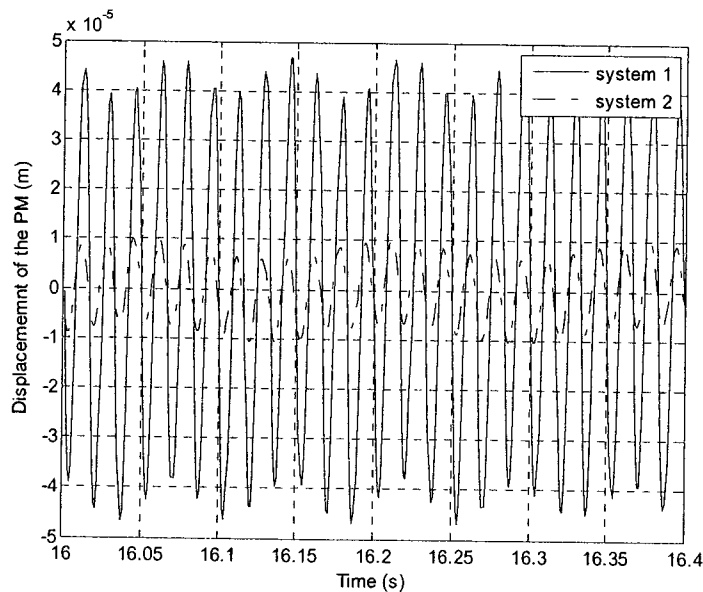
Figure 3.18   Steady state responses of two isolation systems when base motion frequency is 60 Hz and Y =0.0010 m, 1), highly nonlinear beam; 2), the tunable isolator
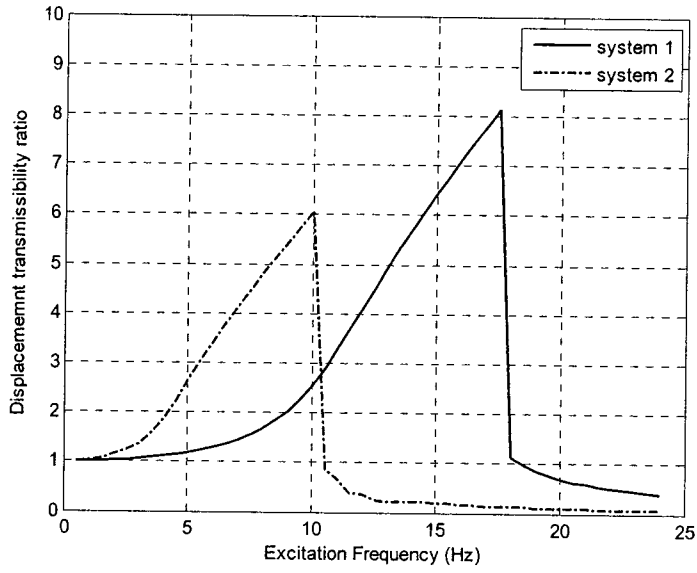
Figure 3.19   Displacement transmissibility ratio as a function of the excitation frequency, when Y=0.0010 m
1), highly nonlinear beam; 2), the tunable isolator
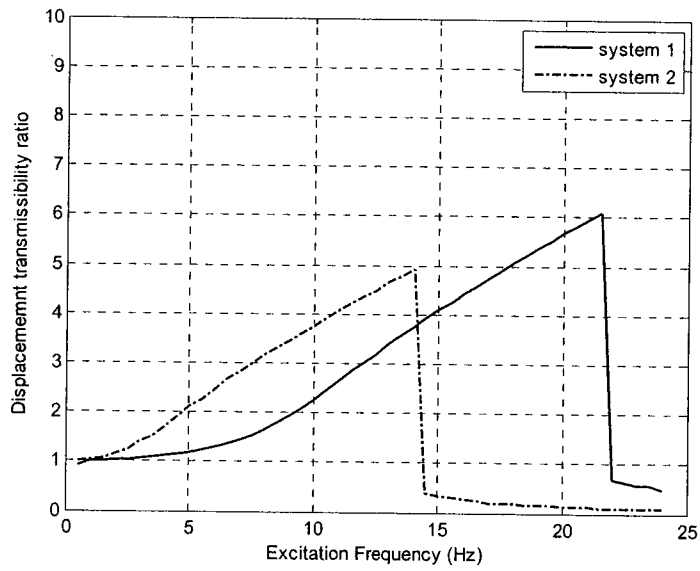
Figure 3.20   Displacement transmissibility ratio as a function of the excitation frequency, when Y=0.0020 m
1), highly nonlinear beam; 2), the tunable isolator

65

Chapter 4. Experimental Studies

This chapter reports the experimental results conducted on the apparatus. The chapter is organized as follows. Section 4.1 focuses on the determination of the natural frequencies of the tunable HSLDS isolator by varying its gap distance or the currents to the EMs. Section 4.2 investigates the displacement transmissibility by subjecting the isolator to a base excitation. Section 4.3 explores the possibility of an on-line tuning. In the experiments, the high nonlinear beam was used.

4.1 Natural Frequencies of the Isolator

Figure 4.1 shows the experimental system which includes three parts: computer control system, electromagnetic isolator system, and data collection system. Figure 4.2 illustrates the photograph of the experiment setup. The computer control system consists of a Data Acquisition (DAQ) Board and a personal computer (PC). The PC provides an operation system to the DSPACE ContorlDesk which offers the interface between Matlab, Simulink and DAQ. The data collection system includes a laser position sensor (Wenglor, CP24MHT80) which measures the displacement of the PM. The analog signal generated by the sensor is converted to the digital signal through the DAQ and then the digital signal is recorded in the computer for further analysis. The sampling time was 0.001 second.
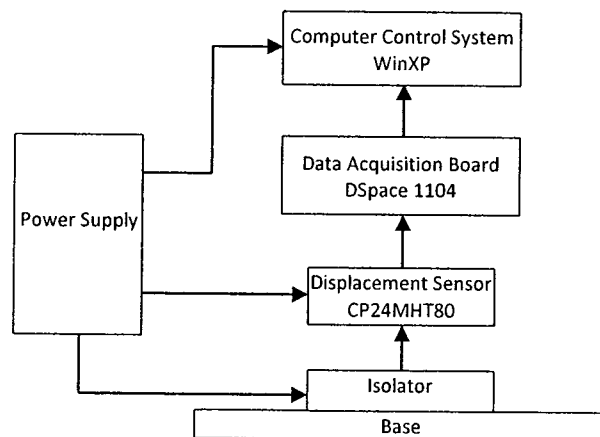
Figure 4.1 Schematic of the experiment system.

66
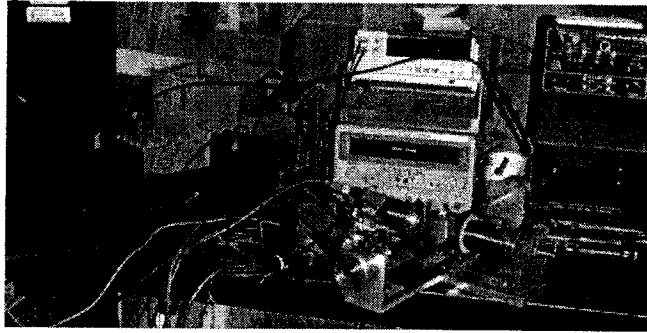
Figure 4.2   Photograph of the experiment setup.

In order to determine the damped natural frequency of the isolator, the PM was set into a free vibration by an initial displacement. First, the isolator without the pair of the EMs was tested. Figure 4.3 shows a time response of the PM and its spectrum. It can be seen that without the negative stiffness effect, the isolator system has damped natural frequency of about 13.0 Hz and a low damping ratio.
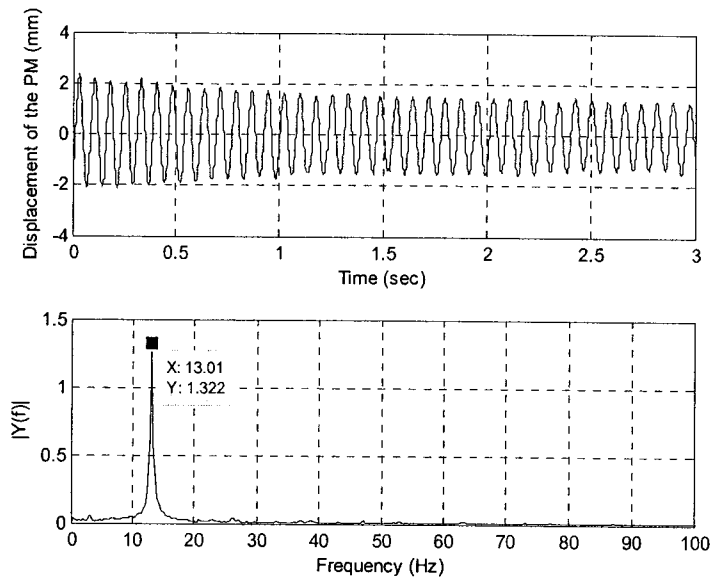
Figure 4.3   Response of the PM and Spectrum of the response when the pair of the EMs was not installed.

Next, the pair of the EMs was installed in place. The gap distance between the PM and the EMs was adjusted. The experiment was repeated for gap distance varied from 0.0680 m to 0.0880 m in a step of 0.0040 m. Figure 4.4 shows the results when the gap distance was 0.0760 m. It can be seen that the damped natural frequency was reduced to 8.7 Hz and the damping ratio was increased as expected. This validates that the interaction between the cores of the EMs and

67

the PM softens the overall spring. Figure 4.5 shows the relationship of the damped natural frequency vs. the gap distance. It can be seen that with increase of the gap distance, the damped natural frequency increase, the change of the natural frequency due to variation of the gap distance becomes smaller.
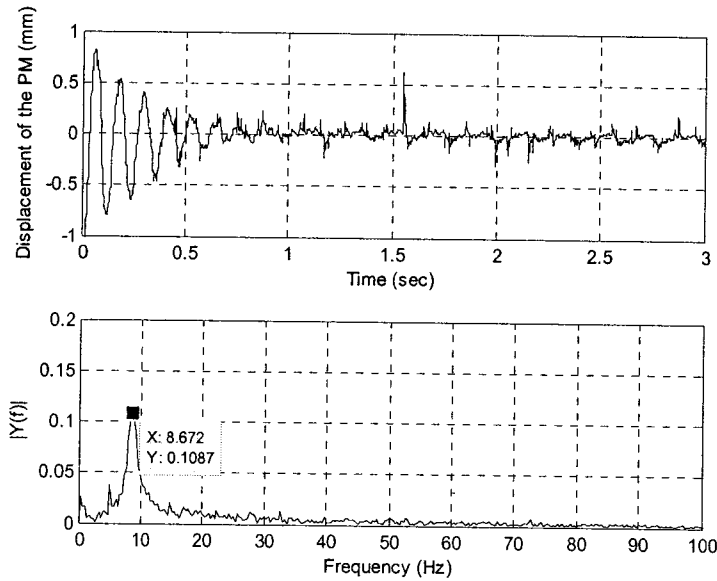
Figure 4.4   Response of the PM and Spectrum of the response when the gap distance is 0.0760 m.
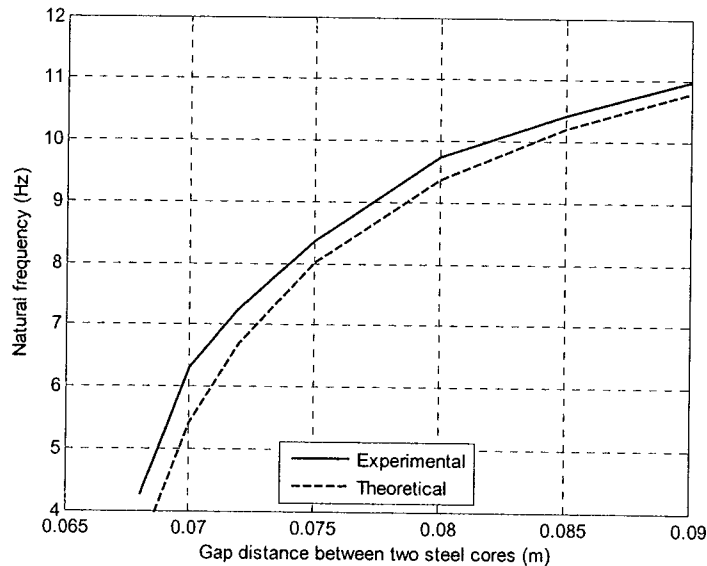
Figure 4.5   Natural frequency of the isolator versus the gap distance.

Last, the negative stiffness effect due to the interaction of the PM and EMs was investigated. For this purpose, the gap distance was fixed at 0.0800 mm, and the current to the EMs was

68

varied from 0.0 A to 2.0 A at a step of 0.25 A. Figure 4.6 shows the results. It validates that tuning the EM current can vary the natural frequency of the isolator.
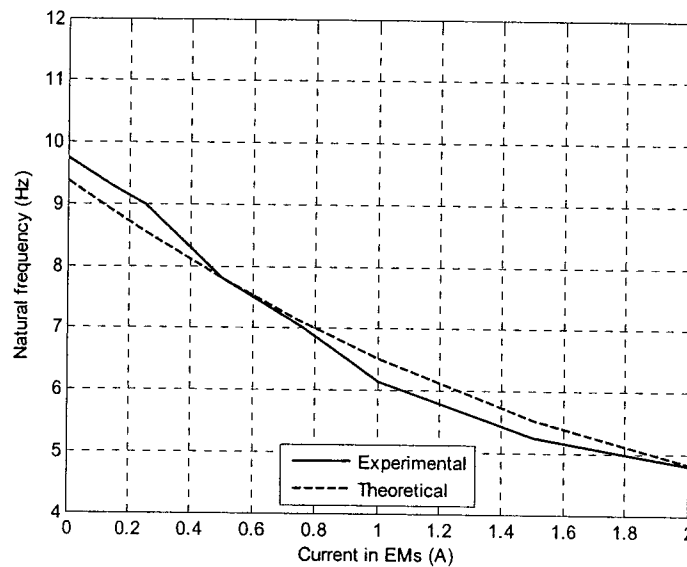
Figure 4.6   Natural frequency of the isolator versus the current when the gap distance is 0.0800 m.

4.2 Displacement Transmissibility

The main aim of this testing is to evaluate the performance of the isolator by investigating the displacement transmissibility ratio versus the excitation frequency for different configurations of the isolator. Figure 4.7 shows the experimental setup which includes four parts: computer control system, base excitation system, electromagnetic isolator system, and data collection system. Figure 4.8 illustrates the photograph of the experiment setup.
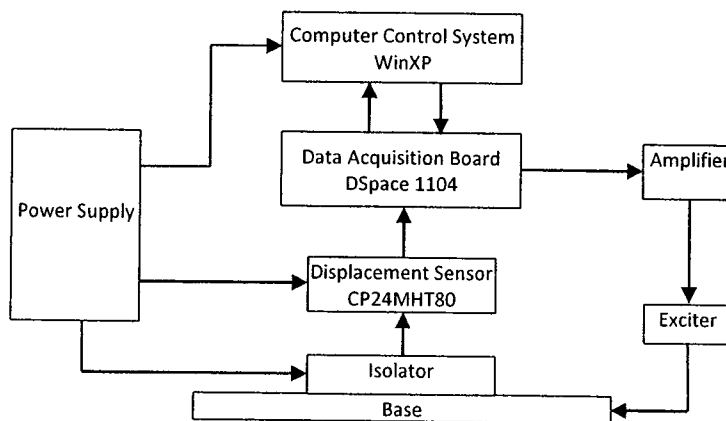
Figure 4.7   Schematic of the experiment system
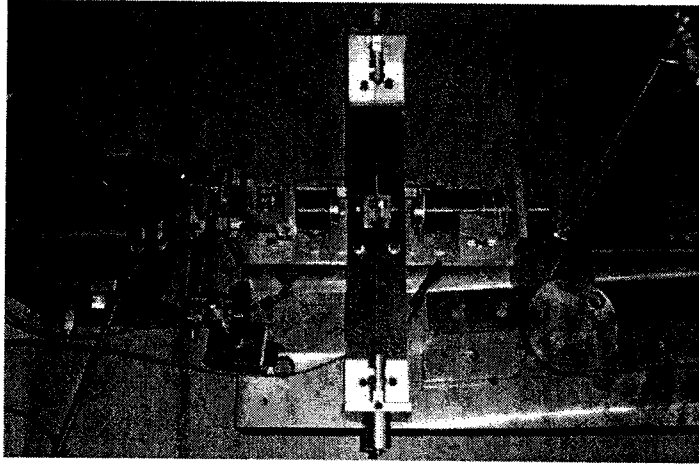
Figure 4.8 Photograph of the experiment setup.

The computer control system, electromagnetic isolator system, and data collection system are the same ones used in the testing reported in Section 4.1. The base excitation system includes a power amplifier (Brüel & Kjær, type 2706), a shaker (Brüel & Kjær, type 4809) and a shaking table. The power amplifier amplifies the signal generated by the computer control system and then sends to the shaker. The shaking table consists of a 6709K12 precision rail and two SR20TB linear guide carts. The apparatus base was securely fastened to the carts such that it could slide on the rail freely. A stinger was used to connect the shaker to the base of the apparatus. The amplitude of the base excitation was maintained at 0.0010 m by adjusting the amplifier gain and the digital amplitude. A pendulum was used to produce an impact to the base, serving as a disturbance whenever needed. The impact external intensity was varied by using different mass on the pendulum. Two masses were used: small (160 g) and large (320 g). The pendulum was released from an initial position of 90^0 to ensure the same disturbance intensity.

The experiment was repeated in the following way. First, the isolator was set up in a prescribed configuration: which is specified by the gap distance and the EM current. Then the isolator was excited sinusoidally at a prescribed frequency. The base motion and the PM motion were measured, respectively. The peak values in a time response of 10 seconds were used to compute the Root-Mean-Square (r.m.s) value. The transmissibility ratio was found as the ratio of the r.m.s value of the PM displacement over that of the base displacement.

First a configuration without the EMs installed was tested. Figure 4.9 shows the transmissibility ratio obtained when the base excitation amplitude was 0.0010 m. It can be seen

that the vibration increases with increase of the exciting the exciting frequency up to about 19 Hz. When the exciting frequency was greater than 19 Hz, the transmissibility ratio suddenly became less than one and the vibration isolation occurred. This is the so-called jump phenomenon [44]. The lowest exciting frequency that can have such a jump phenomenon is referred to as the jump frequency in this study. The system also demonstrated the other highly nonlinear behaviour, i.e., unstability. It was noted that when the exciting frequency approached 19 Hz from the right, the vibration amplitude of the PM is very sensitive to the external disturbance: a disturbance would send a small vibration into a large vibration. This is the so-called bifurcation phenomenon [44].
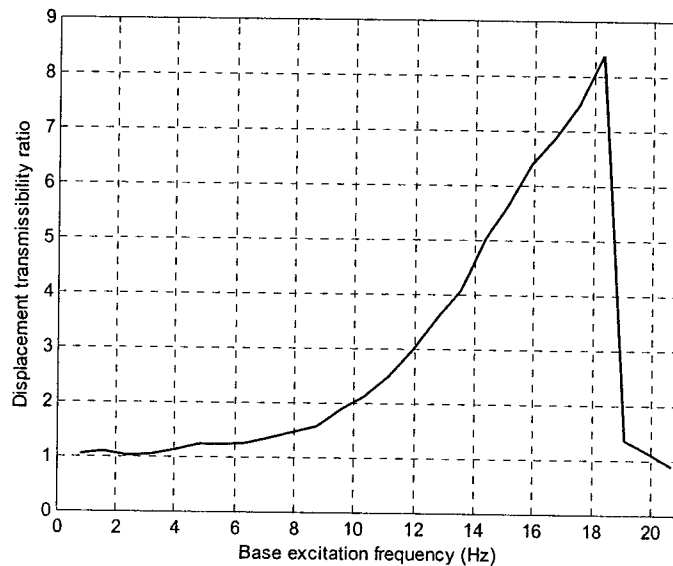
Figure 4.9   Displacement transmissibility ratio of the system without the negative stiffness spring.

Next, the configurations with the EMs installed were considered. With the interaction between the PM and the cores of the EMs, the PM negative stiffness took effect. Figure 4.10 shows the transmissibility ratios for three gap setups. It is noted that with decrease of the gap between the steel cores, the jump frequency shifts to the left or the isolation region is widened. It is also noted that when the exciting frequency was less than the jump frequency, the bigger the gap, the smaller the transmissibility. Subsequently, the negative stiffness effect generated by the interaction between the PM and EMs was investigated. With a fixed gap distance 0.0780 m, the current to the EMs was varied from 0.0 A to 2.0 A at a step of 1.0 A. the results were shown in

71

Figure 4.11. It is observed that with increase of the current in the EMs, the jump frequency of the isolator decreases, and therefore the isolation region is expanded.
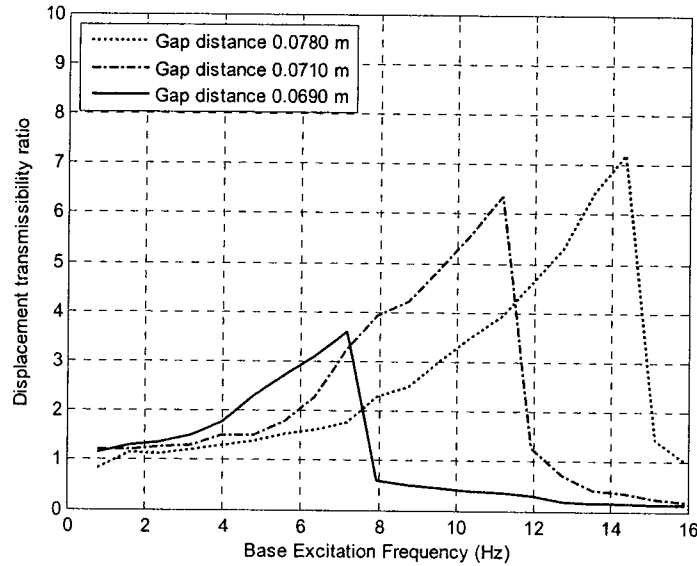
Figure 4.10   Displacement transmissibility ratio of the system with the PM spring in several gap distances.
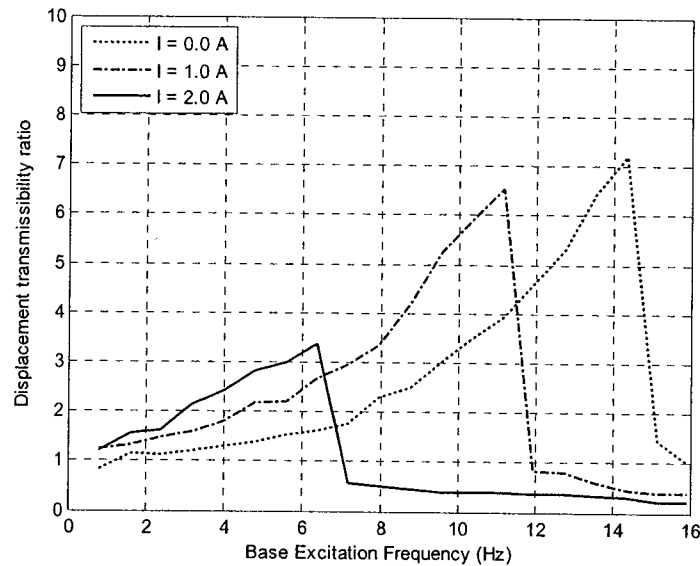
Figure 4.11   Displacement transmissibility ratio of the system with different currents in the EMs when the gap distance is 0.0780 m.

In the previous experiment, it is observed that the PM might vibrate in large amplitude or in small amplitude when the base excitation frequency was greater than the jump frequency. A further experiment to study the response of the PM to a large amplitude excitation was conducted. An external disturbance acting on the PM or holding the PM for a while could switch

the response of the PM between large vibration and small vibration. Figure 4.12 shows the two steady state responses of the PM when the gap distance is 0.0780 m, current is 1.0 A and the base excitation frequency is 7.96 Hz and amplitude is 0.0010 m. It is noted that the amplitude difference between the two responses is significant. If only the larger amplitude of the response was used to compute the transmissibility ratio, Figure 4.13 was obtained instead of Figure 4.11.
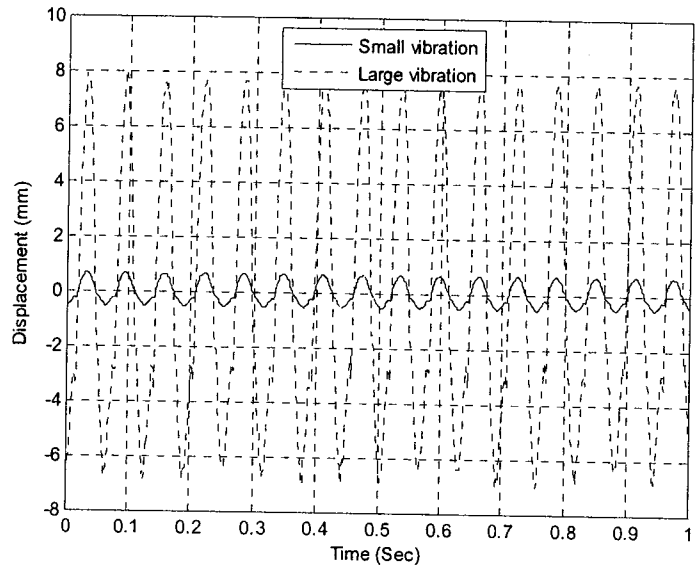
Figure 4.12   Two steady responses of the PM when the gap distance is 0.0780 m, current is 1.0 A and the base excitation frequency is 7.96 Hz.
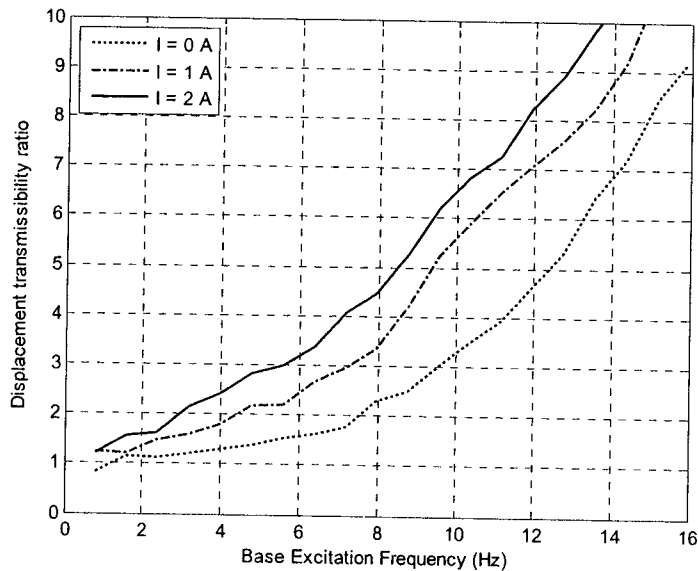
Figure 4.13   Displacement transmissibility ratio of the system with different currents in the EMs when the larger amplitude of the response is considered. Gap distance is 0.0780 m.

73

How disturbance acting on the apparatus base affected the steady state response of the PM was studied. The isolator was set up such that the gap distance was 0.0780 m and the EM current was 1.0 A. The pendulum was used to generate an impact to the base after the response of the PM was in the steady state. Figure 4.14 demonstrates the transmissibility ratio obtained. It can be observed that an impact to the base can trigger a sudden change in the response of the PM, and therefore change the transmissibility ratio. With an increase of the impact magnitude, the jump frequency shifts to the right and the isolation region is narrowed.
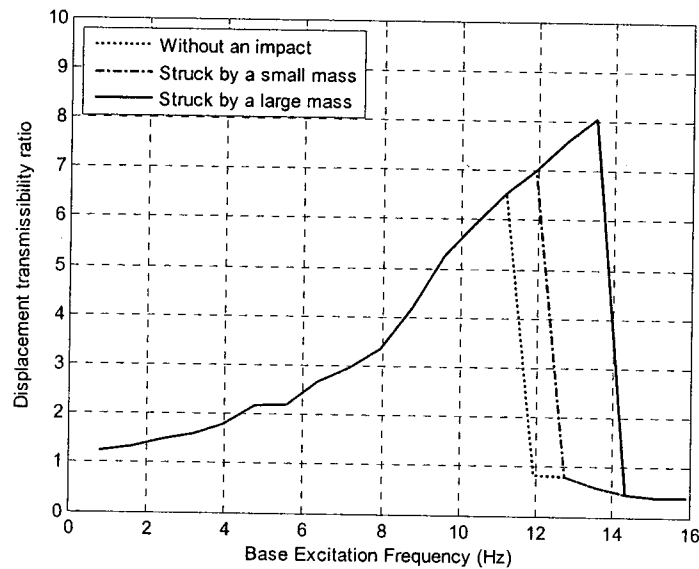
Figure 4.14   Displacement transmissibility ratio of the system with different shock loads when gap distance is 0.0780 m, current in the EMs is 1.0 A.

4.3   Online Tuning Experiment

An online tuning intends to adjust the EM current according to the response of the PM such that the electromagnetic isolator maintains its best performance in the event of condition changes. For example, when a machine starts up, the exciting frequency will increase and pass through the jump frequency. Or when the isolator operates in the isolation region, a disturbance may still set the isolated mass into a large vibration. In this section, an auto-tuning strategy is developed. Using the online tuning, the best displacement transmissibility is determined. The isolator's auto-tuning ability is tested by devising several testing scenarios.

74

To devise a tuning strategy, refer to Figure 4.11. When subjected to a constant amplitude base excitation, a tunable isolator possesses two jump frequencies. When the EM current is zero, the amplitude jump occurs at a higher frequency denoted as f_1. When the EM current is maximum, the amplitude jump occurs at a lower frequency denoted as f_2. For the isolator of Figure 4.11, f_1 is about 15.0 Hz, while f_2 is about 7.0 Hz. When the exciting frequency is less than f_2, the dynamic stiffness should be as large as possible to keep the transmissibility ratio close to one. When the excitation frequency is greater than f_1, the EM current should be zero. When the exciting frequency is between f_2 and f_1, the dynamic stiffness should be reduced by applying the current to the EMs.

Figure 4.15 shows the schematic of the experiment setup that is almost as same as the one in the previous experiment. In addition to the displacement sensor, an accelerometer (Brüel & Kjær, 4393V) and a charge amplifier (Brüel & Kjær, 2692) were used together to measure the base excitation. The computer control system also generated a control signal that was sent to the EMs through an amplifier (LM12CL). Figure 4.16 shows a Simulink model for auto-tuning. Through channel DAC #8, the sinusoidal signal is sent to the shaker to generate base motion. The displacement signal of the PM and the acceleration signal of the base are acquired through channel ADC #5 and ADC #8, respectively. An embedded MATLAB function block "Cal_Freq" is used to collect the samples for a prescribed length such as $N = 2048$ and then compute the frequency of the base motion through FFT. An embedded MATLAB function block "Cal_RMS" is used to collect the samples for a prescribed length such as $N = 2048$ and calculate the Root-Mean-Square value of the PM displacement. An embedded MATLAB function block "Cal_Switch" is used to determine which of the found frequencies is more likely to be the exciting frequency. In general, for a high exciting frequency, the frequency determined using the base acceleration signal is more reliable while for a low exciting frequency, the one determined using the PM displacement signal is more reliable. The found exciting frequency and the RMS value of the PM displacement are sent to an embedded MATLAB function block "Cal_TuningSignal" where the desired EM current is determined. When the base excitation frequency is less than f_2, the desired EM current is set to a negative value so that the EM spring appears as a positive spring. When the exciting frequency is between f_2 and f_1, the EM current is

changed to a positive values so that the HSLDS is generated. When the base excitation frequency is greater than f_1, no EM current is needed and the isolator works as a passive isolator.
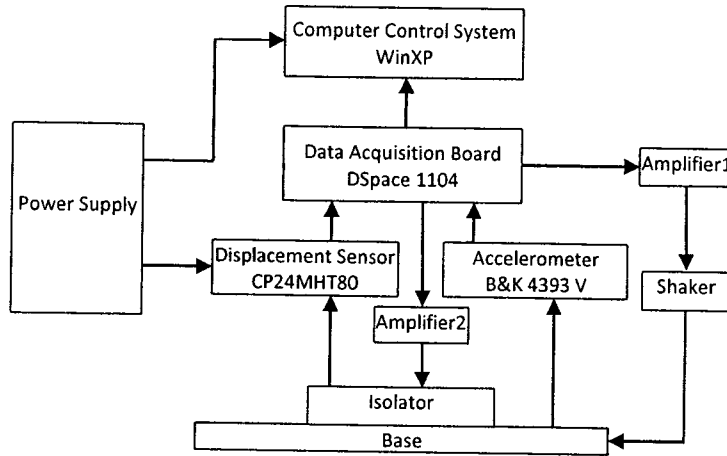
Figure 4.15   Schematic of the experiment system
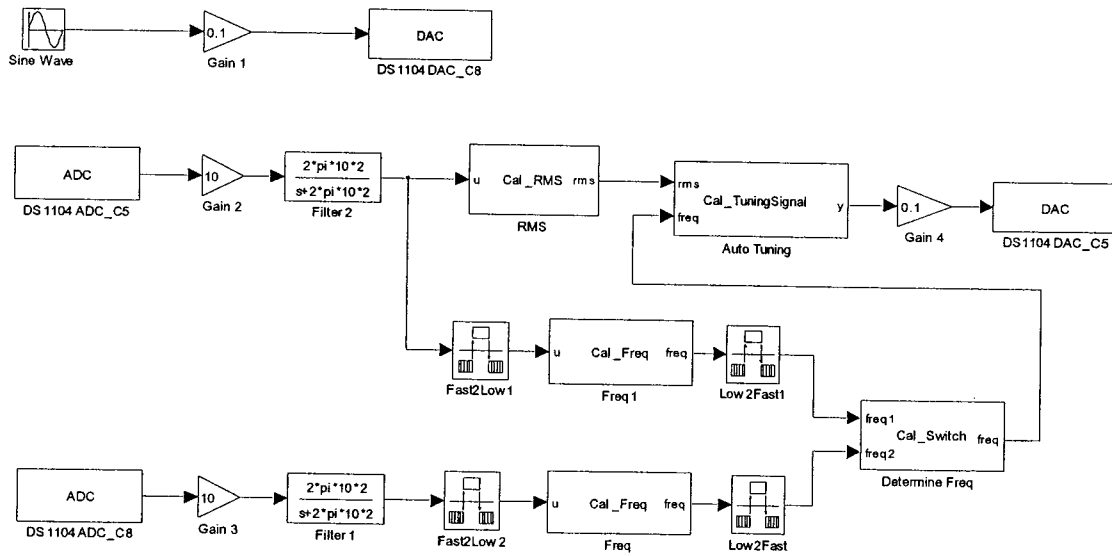
Figure 4.16   Simulink model of the online tuning.

The on-line tuning strategy was tested with a base excitation whose amplitude was 0.0005 m. Figure 4.17 compares the results of the four configurations: 1). the EM current is -1.5 A and the EM spring possesses a positive stiffness; 2). the EM current is zero; 3). the EM current is 1.0 A and the EM spring possesses a negative stiffness; 4). the EM current is tuned on-line. The online tuning method works as follows. When the excitation frequency is less than 9.5 Hz, the EM-PM-EM assembly is set in a repelling configuration by applying a current -1.5 A to the EMs. This way, the EM spring serves as a positive spring, and thus the isolator has a high dynamic

stiffness. When the excitation frequency lies in the range [9.5 14.0] Hz, the direction of the EM current is changed so that the EM-PM-EM is in the attracting configuration. In the meanwhile, the value of the EM current is changed to 1.0 A. These adjustments result in vibration isolation. When the excitation frequency is greater than 14.0 Hz, the EM current is changed to zero. This tuning method can always make sure that the transmissibility ratio is smaller. Figure 4.17 shows the transmissibility obtained by implementing the tuning strategy. It can be seen that the isolator performance is improved significantly. For the frequency less than 9.5 Hz, the transmissibility was kept almost to be one. For the frequency range of [9.5 14.0] Hz, the transmissibility is smaller than the values obtained without applying the current.
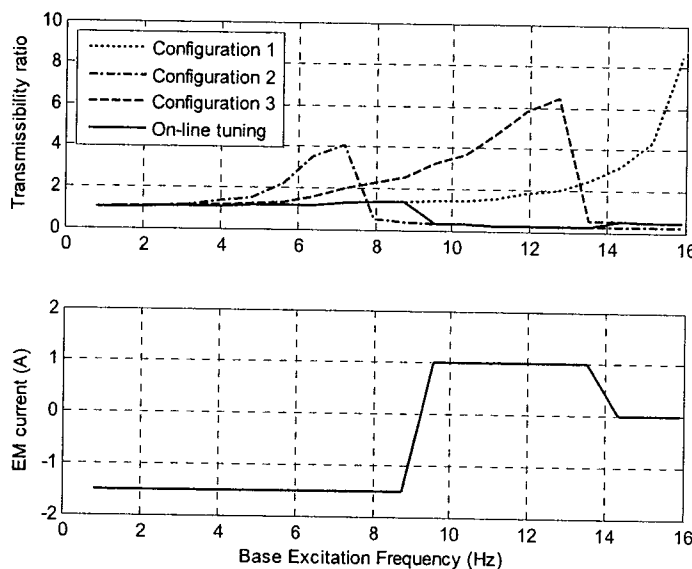
Figure 4.17   Displacement transmissibility ratio of the tunable isolator system
when the amplitude of the base excitation is 0.0005 m.
(a) the displacement transmissibility ratios for several configurations:
  1) EM current is -1.5 A and EM spring serves as positive spring;
  2) No current in EM;
  3) EM current is 1.0 A and EM spring serves as negative spring.
(b) the EM current.

The capability of the method's handling with disturbance was investigated as well. In the test, the amplitude of the base excitation was 0.0005 m. Figure 4.18 shows how the isolator reacted to a disturbance. The system was excited at 9.5 Hz and the EM current was set to 1.0 A so that the low dynamic stiffness ensured a small vibration. After 3.0 second, a base disturbance was induced such that the PM jumped to a large vibration. With the tuning, the EM current was increased so that the dynamic stiffness was further reduced and the vibration was brought back to

the small level. Figure 4.19 shows the case when the exciting frequency was 14.3 Hz and the EM current was zero in the beginning. When a disturbance occurred, the current was activated and adjusted according to the response level. When the response was below the prescribed threshold, the EM current was turned to zero again.
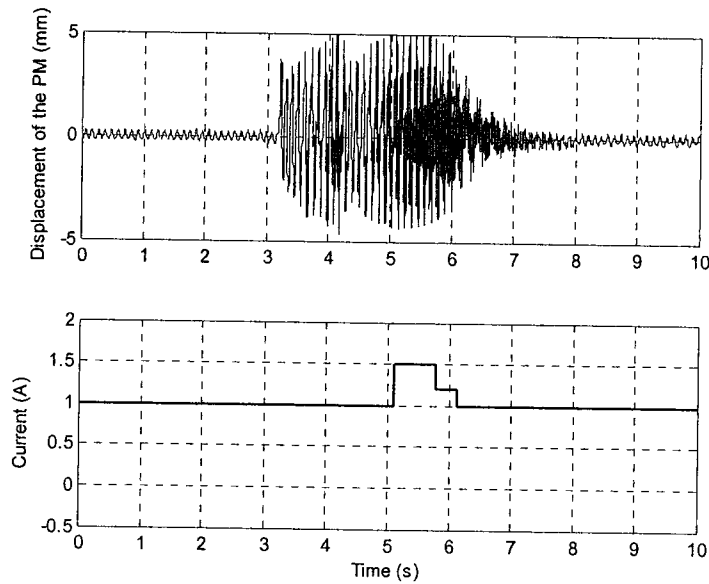
Figure 4.18   Response of the PM when the amplitude of the base excitation is 0.0005 m, the excitation frequency is 9.5 Hz and disturbance acted on the base.
(a) the response of the PM;   (b) the EM current.
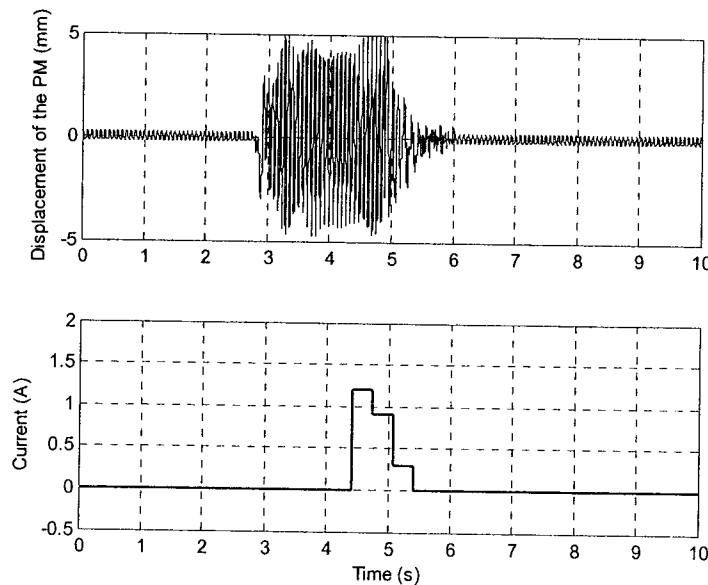
Figure 4.19   Response of the PM when the amplitude of the base excitation is 0.0005 m, the excitation frequency is 14.3 Hz and disturbance acted on the base.
(a) the response of the PM;   (b) the EM current.

Chapter 5.   Conclusion and Future Works

In this part, the tunable vibration isolator has been investigated. This chapter summarizes the overall conclusions of this part and gives recommendations for future work.

5.1 Conclusions

In this part, an electromagnetic isolator, which can be constructed as a passive isolator and a tunable isolator, has been developed. The key characteristic of the electromagnetic isolator is high-static-low-dynamic stiffness (HSLDS), which can support a large static load while has a very low natural frequency. The HSLDS feature is obtained by connecting a mechanical spring, in parallel with a negative spring which is produced by a pair of electromagnets (EM) and a permanent magnet (PM) in attracting configuration.

Due to the high nonlinearity of the magnetic field, the magnetic force model has been established from experimental results directly rather than from the fundamental theory of electromagnetism. The influence on the permeability of the steel core has been analysed and characterised. With an increase of the current in the EMs, the relative permeability in the steel core decreases. The force acting on the PM should be the sum of the force between the PM and the steel cores and the force between the PM and EMs. The traditional method overestimates the force acting on the PM due to neglecting the change of the permeability in the steel cores. In order to correct this overestimation, a novel method to compute the force acting on the PM has been developed. The force acting on the PM is a function of the gap distance between the EM and the PM, and the current in the EM. These two factors also have influences on the stiffness of the PM spring and the EM spring. With an increase of the gap distance between the steel cores, the stiffness of the PM spring increases and the softening property decreases. If the gap distance between the two EMs is fixed, an increase of the current in the EMs decreases the stiffness of the EMs, but increases the softening property. The PM spring has been used to construct the passive isolator and the EM spring has been used to construct the tunable isolator.

Two types of the mechanical springs, which have the same linear stiffness, have been used in this study. The mechanical spring with high nonlinearity constructs a passive isolator alone.

79

The isolator created by combining the high nonlinear mechanical spring and the PM spring demonstrates the HSLDS characteristic, and extends the isolation region comparing to the one using the mechanical spring alone. Combination of the low nonlinear mechanical spring and the PM spring can result in a low dynamic stiffness while the stiffness fluctuation in the neighbourhood of the equilibrium position is acceptable. The distinguished case is that the combination of the low nonlinear mechanical spring and the EM spring is capable of obtaining a quasi-zero-stiffness (QZS). Numerical simulations are used to study the base excitation of the four configurations. The numerical simulation results demonstrate the maximum transmissibility ratio, jump frequencies, and unstable region for each configuration.

A commercial software package, Comsol Multiphysis, is employed to characterize the electromagnetic isolator as well. A 3D models built in AC/DC module is used to study the characteristics of the PM and EMs. And simplified 2D models built in Structure Mechanics module are utilized to examine the performance of the isolator. The study applies a weakly coupled approach of solving a coupled multiphysics application to reduce the computational burden. It has been found that Comsol models correctly represent the magnetic flux densities of the EM and PM, and the force acting on the PM. The results of the experiments and Comsol simulation agree well. It has been shown that Comsol Multiphysics is a powerful program to deal with mechatronics problems. It has also shown that the learning curve for building a Comsol model is relatively steep. It may be ineffective for a beginner to conduct research by using this software.

An apparatus for the proposed tunable isolator has been designed and built. The apparatus is a passive isolator when no current is in the EMs. A decrease of the gap distance decreased the natural frequency of the system. With current in the EMs, the apparatus becomes a tunable isolator. An increase of the current decreases the natural frequency of the system. The measured transmissibility ratios of the isolator for different gap distances and currents in the EMs have been compared. The experiment observations have shown that the isolator system with hardening property has more than one steady state when the base excitation frequency is greater than the jumping frequency. How the disturbance acting on the base triggers a catastrophic change in response has been investigated. On-line tuning method is used to make the isolator always work in the optimum performance.

5.2 Future Works

The analysis presented in this thesis has improved the understanding of the characteristics of a HSLDS isolator. However, some issues remain open and are thought to be worth of further study:

(1) The EMs used in this study have high nonlinearities. The magnetic force cannot be easily and accurately modelled by using the fundamental theory of electromagnetism. The complex magnetic force model established in this thesis prevents from analytical studying the characteristics of the HSLDS isolator. Therefore, well-designed commercial electromagnets should be used in future work and thus the equation of motion of the mass supported by the springs should have a simple form. This will make it possible to analytically investigate the nonlinear behaviour of the system. And then simple formulas for the prediction of the jump frequency and the bifurcation point can be established.

(2) Due to the limitation of the 32-bit computer operating system, only 1/180 physical model has been used in the Comsol simulation and weakly coupled method has been employed to solve the multiphysics problems. In future research, the Comsol model should be run on an advanced computer system. At least a quarter of the physical model should be used and the fully coupled method should be employed to solve the multiphysics problems. In addition, Comsol multiphysics can also be used as a design tool if it is used together with Matlab. The optimization design with Comsol multiphysics can be used to find the better solution of the isolator. Additional efforts should be spent on this point.

(3) The apparatus also has large margins for improvement. A low nonlinear mechanical spring should also be used. The numerical analysis states that a low nonlinear mechanical spring can be helpful to improve the performance of the isolator. Further experiments could be carried out on this issue. In addition, the weight of the apparatus should be reduced so that the apparatus can be tested when subjected to higher base excitation frequency and larger base excitation amplitude.

Part II

A Fuzzy-Neural Network Based Active Control Isolator

Chapter 6.   Adaptive FNN Controller

As pointed out in Chapter one, active vibration isolators offer superior performance through a feedback system. As most isolators are nonlinear and their parameters are not precisely known, an effective control algorithm is desirable for them. In Part two, an adaptive fuzzy-neural network (FNN) controller proposed in [31, 32] is applied to active vibration isolators. The study intends to investigate the applicability of the algorithm and compare it with some conventional control methods. In addition, the study will reconfigure the electromagnetic isolator such that it can act as an active isolator. This part of the thesis is organized as follows. In Chapter 6, a brief review on fuzzy neural networks is presented and the FNN controller is introduced. In Chapter 7, a numerical simulation is conducted to compare the FNN controller with three other controllers. In Chapter 8, the conclusions are drawn and future works are recommended.

6.1 Literature Review

Many physical systems are non-linear in nature. Although non-linear models intend to closely represent the underlying properties of the systems, such models still contain different kinds of uncertainties. The causes of uncertainties can be attributed to unmodelled dynamics, unknown external disturbance, and poor knowledge of parameter values, etc. [47].

The control of uncertain nonlinear systems has stirred a great deal of interest to researchers. During the past decade, the research on how to deal with different kinds of uncertainties has achieved tremendous successes in both theory and application [48]. In the early stage of the research, the adaptive control methods via feedback linearization [49-51] were applied to a relatively simple class of nonlinear systems that the uncertain nonlinear functions appear on the same equation as the control input in the state space model. If the uncertainty of the system is bounded, a deterministic robust control method can be used [52, 53]. Since these techniques require some prior knowledge about the uncertain nonlinearities, such as known functional descriptions [47]. This may impose a limitation in an industrial control environment where such prior knowledge is not available. Therefore, it is impractical to drive these systems to desired responses by using these adaptive controllers.

Recently, it has been proved that neural networks are universal approximators [54, 55]. With increased size and complexity, a neural network can approximate any nonlinearity with arbitrary precision [56]. Therefore, many investigations have been conducted by using neural networks to approximate the unknown nonlinearities and then design the controllers [56]. A single neural network can define different nonlinearities; therefore, it is possible that two completely different nonlinear systems can be controlled by one controller.

Wang [57] proved that fuzzy systems with product inference, centroid defuzzification, and a Gaussian membership function are capable of approximating any real continuous function on a compact set to arbitrary accuracy. Thus, fuzzy logical systems can also be used in a similar setting with neural networks [48].

Fuzzy systems and neural works are complementary technologies to design an effective controller for uncertain nonlinear system. Fuzzy logic techniques most often use linguistic information from experts; neural networks extract information from systems. Recently, the synergy of the two paradigms has given rise to a rapidly emerging field--fuzzy neural networks (FNN) which are intended to combine the advantages of both the fuzzy logic and the neural networks. Results have shown that FNN could offer a viable approach for system modelling [58]. Buckley and Hayashi [59] argued that FNNs are not universal approximators. Feuring et al. [60] examine the capacity of FNNs and conclude that the FNNs can approximate fuzzy continuous real functions on a compact domain to any degree of accuracy.

However, the use of fuzzy systems, neural networks and FNNs to approximate uncertainties has a substantial drawback, that is, when the number of rule bases in the fuzzy logic system or neural nodes in the neural network increases, the number of parameters to be tuned online increases significantly. This will lead to an unacceptably long learning time [58, 61]. That has raised some researchers looking for overcoming the drawback. [48] demonstrates a novel approach to reduce the number of parameters needed to be adapted online to $2n$, where n is the dimension of the state in the design system.

In this thesis, a novel approach is introduced to drive the response of a class of uncertain nonlinear second order one dimensional systems to a desired state under an unknown bounded external excitation. The adaptive FNN controller designed in this thesis contains only one

parameter adapt law to estimate the norm of the ideal weighting vector. This is feasible in practice due to the significant decrease of the burdensome computation of the algorithm.

6.2 Background

6.2.1 Fuzzy systems

A fuzzy system, as shown in Figure 6.1, is a static nonlinear mapping between its inputs and outputs, which are real number [62]. It is noted that a fuzzy system has four principal elements: fuzzification interface, fuzzy rule base, fuzzy inference engine, and defuzzification interface. The fuzzy system works in the following way:

1. The fuzzification interface converts the crisp inputs to fuzzy sets (fuzzy inputs). Singlenton fuzzification and nonsinglenton fuzzification are two possible choices.

2. The fuzzy inference engine uses the fuzzy rules in the rule base to obtain fuzzy conclusions (fuzzy outputs). Lee [63] presented the definition of the set theoretic operations of union, intersection and complement for fuzzy sets via their membership functions. And in [63], he pointed out that the min and product compositional operators are the most frequently used in fuzzy logic control systems.

3. The defuzzification interface translates the fuzzy conclusions into the crisp outputs. There are at least three possible choices of this mapping: maximum defuzzification, center-average defuzzification and modified center-average defuzzification.
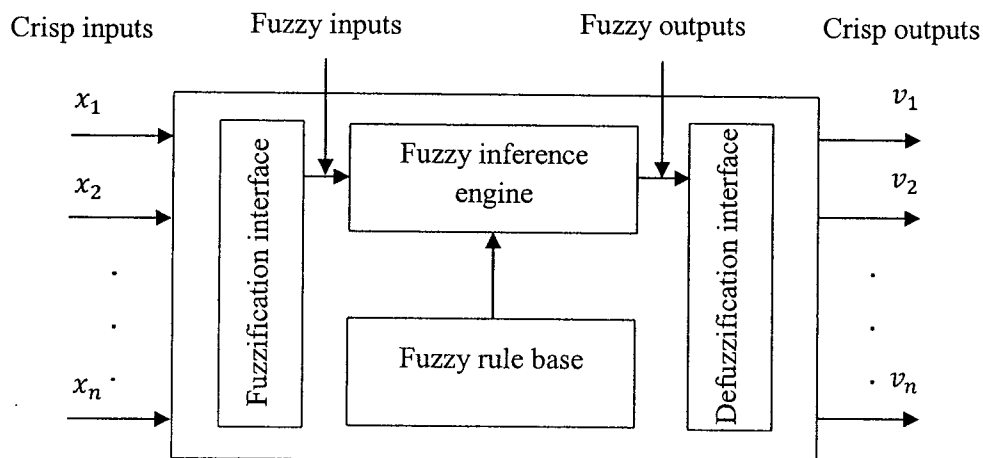
Figure 6.1   Basic configuration of fuzzy systems.

If a fuzzy rule base in the case of an n-input-single-output fuzzy system has a collection of the following fuzzy rules:

$$R_i: \text{IF } x_1 \text{ is } F_1^i \text{ and } \dots \text{ and } x_j \text{ is } F_j^i \text{ and} \dots \text{ and } x_n \text{ is } F_n^i; \text{ Then } v \text{ is } B^i \quad (i=1,2,\dots,M)$$

where $x = [x_1, \dots, x_n]^T \in R^n$, and $v \in R$ are the input and output of the fuzzy system, respectively, F_j^i and B^i are fuzzy sets in R. By adopting the singleton fuzzification, center-average defuzzification, product inference and Gaussian membership functions, the output of the fuzzy system can be written as [57]

$$v(x) = \frac{\sum_{i=1}^{M}\left(p_i \prod_{j=1}^{n} \mu_{F_j^i}(x_j)\right)}{\sum_{i=1}^{M}\left(\prod_{j=1}^{n} \mu_{F_j^i}(x_j)\right)} \tag{6.1}$$

where M is the number of fuzzy rules in the fuzzy rule base, p_i is the point at which membership function achieves its maximum value and $\mu_{F_j^i}(x_j)$ is Gaussian membership function which is given by:

$$\mu_{F_j^i}(x_j) = e^{-\frac{(x_j - c_i)^2}{2\sigma_i^2}}$$

where c_i and σ_i are the centre and width of the ith fuzzy set F^i, respectively.

Assume

$$\emptyset_i(x) = \frac{\prod_{j=1}^{n} \mu_{F_j^i}(x_j)}{\sum_{i=1}^{M}\left(\prod_{j=1}^{n} \mu_{F_j^i}(x_j)\right)} \tag{6.2}$$

$$\Phi = [\emptyset_1(x), \emptyset_2(x), \dots, \emptyset_M(x)]^T \tag{6.3}$$

$$P = [p_1, p_2, \dots, p_M]^T \tag{6.4}$$

then equation (6.1) can be rewritten as

$$v(x) = P^T \Phi \tag{6.5}$$

The fuzzy system (6.5) has been used as basic building blocks of adaptive fuzzy controllers [64]. First of all, it is proved by Wang [57] that the fuzzy system (6.5) is universal approximator.

Second, linguistic information from human experts can be directly incorporated into the controllers.

6.2.2 Artificial neural networks

Artificial neural networks (ANN) are by far one of the most successful approaches for realizing human intelligence in machines. ANNs have been used to solve a variety of problems in signal processing, pattern recognition, control system, system identification, and etc.. Traditional approaches have been employed to solve these problems with certain restrictions. However, none of them are flexible enough to perform well beyond the constraints [66].

Like other types of networks, an artificial network consists of a set of connected nodes that are known as artificial neurons. Figure 6.2 demonstrates the graphical presentation of a single neuron, which consists of a linear combiner followed by an activation function [66].
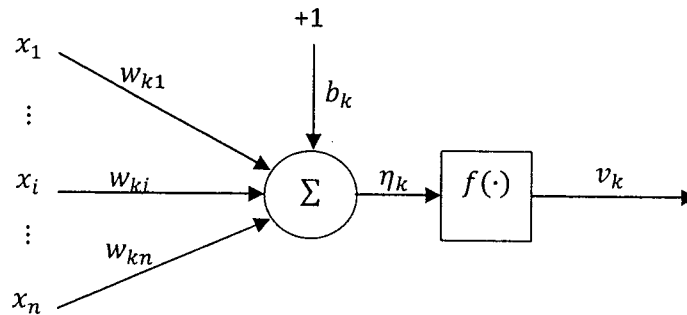
Figure 6.2 The structure of a single neuron.

The mathematical outcome of a single neuron can be written as:

$$v_k = f(\sum_{i=1}^{n} w_{ki} x_i + b_k) \tag{6.6}$$

where, w_{ki} is the connection weight, b_k is a threshold parameter, and $f(\cdot)$ is a function that provides the activation for the neuron. The connection weight can either be positive or negative, which groups the connection types into two categories: excitatory connections and inhibitory connections [65]. Excitatory connections increase a neuron's activation while inhibitory connections decrease a neuron's activation.

Based on how the neurons communicate with others by weighted uni-directional connections, ANNs can be grouped into two categories [65]:

87

- Feed-forward networks, in which only allows information to flow among neurons in one direction. The feed-forward networks are memory-less because the response to an input is independent of the previous network state. In addition, with a given input, only one set of output values are produced instead of a sequence of values. In other words, feed-forward networks are static.

- Recurrent (or feedback) networks, in which information flow is in either direction and/or recursive. The recurrent networks always calculate the neuron outputs whenever a new input pattern is presented. The neuron output is possibly fed back into itself as an input. Compared to feed-forward networks, recurrent networks are a dynamic system.

Artificial neurons in an ANN can be grouped into different layers according to their tasks. A layer that receives input signal from the environment is called an input layer and a layer that transmits signals to the environment is called output layer. Any layer that lies between the input and output layers are referred as hidden layers that do not have direct contact with environment.

Artificial neural networks (ANNs), inspired in biological neural networks, are massively parallel computing systems consisting of an extremely large number of simple highly inter-connected processors (neurons), illustrated in Figure 6.3. A very important feature of ANNs is the learning ability, in which ANNs can update network architecture and connection weights to efficiently perform a specific task by being trained with available examples. The iterative process of updating weights can improve the performance of the network. Thus, ANNs can be trained with known examples of a problem, and then are able to handle unknown cases of the problem. This feature makes ANNs very appealing in applications where the object is not very clear but where training data is readily available [65].
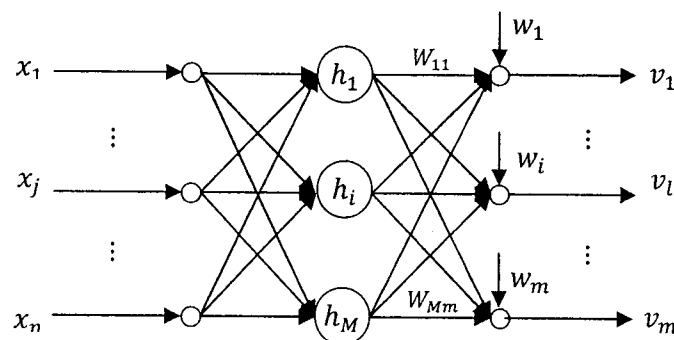
Figure 6.3   The structure of a neuron network.

ANNs research has experienced three periods of extensive activity and many types of ANNs have been developed in the past decades [65]. The most important class ANNs for real world problem solving includes: multilayer perceptron, radial basis function networks and Konhonen self-organizing map networks. Detailed descriptions on ANNs can be found in [67, 68].

6.2.3 Fuzzy neural networks

Both fuzzy systems and artificial neural networks can be used to solve a problem if there does not exist a mathematical model for a given system. Fuzzy systems are capable of handling uncertain and imprecise information while artificial neural networks are capable of learning from examples. Fuzzy neural networks (FNN) intend to combine the advantages of both fuzzy systems and artificial neural networks. FNN retain the basic properties and architecture of neural networks and simply "fuzzify" some of their elements [58]. Researchers have cast their interest on the fuzzy neural networks, and several different types of fuzzy neural networks have been proposed [69].
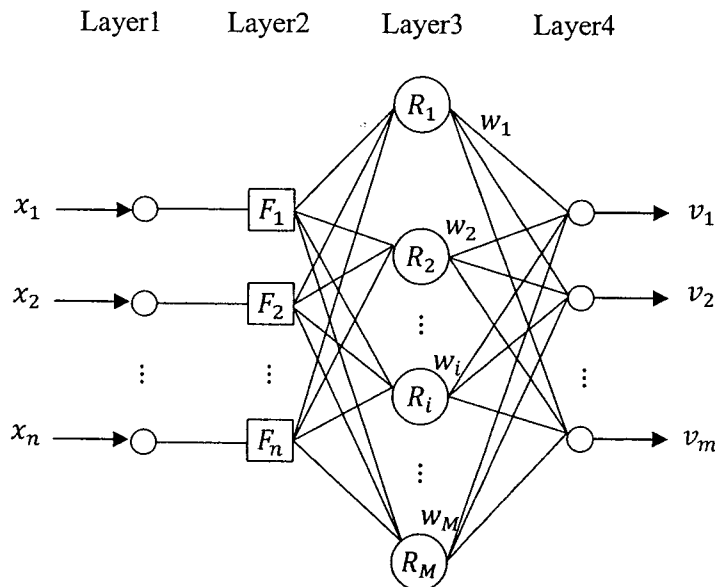
Figure 6.4   The structure of a FNN

The basic configuration of the FNN system consists of one input-layer, one output-layer and at least one hidden-layer. Figure 6.4 shows a structure of FNN [58]. Layer one is the input layer, which converts the input vector into next layer directly. Layer two is the fuzzification layer. Layer three is the fuzzy rule layer. A node in this layer represents a fuzzy rule. The number of

nodes in this layer is equal to the number of fuzzy rules. Layer four is the output layer where each node acts as a defuzzifier and computes the output value. The output of the FNN system with singleton fuzzification, product inference and center average defuzzification can be written as

$$v_l(x) = \frac{\sum_{i=1}^{M}(w_{il} \prod_{j=1}^{n} \mu_{F_j^i}(x_j))}{\sum_{i=1}^{M}(\prod_{j=1}^{n} \mu_{F_j^i}(x_j))}, l = 1,2, \dots, m \qquad (6.7)$$

where w_{il} are the weighting values to connect layer three and layer four, $\mu_{F_j^i}(x_j)$ is fuzzy basis function.

Assume

$$\emptyset_i(x) = \frac{\prod_{j=1}^{n} \mu_{F_j^i}(x_j)}{\sum_{i=1}^{M}(\prod_{j=1}^{n} \mu_{F_j^i}(x_j))} \qquad (6.8)$$

$$\Phi = [\emptyset_1(x), \emptyset_2(x), \dots, \emptyset_M(x)]^T \qquad (6.9)$$

$$W_l = [w_{1l}, w_{2l}, \dots, w_{Ml}]^T \qquad (6.10)$$

then the equation (6.7) can be rewritten as

$$v_l(x) = W_l^T \Phi \qquad (6.11)$$

Feuring et al. [60] pointed out that the FNN system (6.11) is capable of uniformly approximating any well-defined nonlinear function over a compact set to an arbitrary degree of accuracy.

6.3 Adaptive FNN Control Design

An adaptive FNN controller proposed in [31, 32] is presented in this Section. Consider a general class of one degree-of-freedom uncertain non-linear systems described by the following differential equations:

$$\begin{cases} \dot{x}_1 = x_2 \\ \dot{x}_2 = f(x) + g(x)u(t) + d(t) \end{cases} \qquad (6.12)$$

where $x = [x_1, x_2]^T \in R^2$ is the state vector, $u(t) \in R$ is the control input, $d(t) \in R$ is an unknown external disturbance, which satisfies $|d(t)| \leq \bar{d}$ with $\bar{d}$ being a constant. $f(x)$ and $g(x)$ are unknown nonlinear smooth functions with $f(0) = 0$. The following assumptions complete the description of system (6.12).

Assumption 1: The sign of $g(x)$ is known, and there exist constants b_m and b_M such that

$$0 < b_m \leq |g(x)| \leq b_M$$

Without loss of generality, it is further assumed that $g(x) \geq b_m$. It should be noted that b_m and b_M are needed only for stability analysis and will not be needed for designing the proposed controller. Therefore, b_m and b_M can be unknown constants.

Assumption 2: The reference signal $x_r(t)$ and its time derivatives up to the *2th* order are continuous and bounded.

$$\|[x_r, \dot{x}_r, \ddot{x}_r]^T\| \leq \bar{x}_r$$

The objective of designing an adaptive FNN controller for system (6.12) (under Assumptions 1 and 2) is twofold:

(1) The closed loop system is semi-globally uniformly ultimately bounded.

(2) The tracking error can be reduced both in the transient and asymptotic period by an explicit choice of the design parameters.

As indicated in [60], for a given $\varepsilon > 0$, any continuous function $f(x)$ defined on a compact set $\Omega_x \subset R^n$ can be written as:

$$f(x) = W^T \Phi(x) + \delta(x), |\delta(x)| \leq \varepsilon \tag{6.13}$$

where $x \in \Omega_x \subset R^n$ is the input vector with n being the FNNs input dimension, $W = [w_1, w_2, \cdots, w_M]^T$ is the weighted vector, and $\Phi(x) = [\emptyset_1(x), \emptyset_2(x), \cdots, \emptyset_N(x)]^T$ is the fuzzy basis function vector with $\emptyset_i(x)$ being Gaussian function, and $\delta(x)$ is the approximate error.

A constant θ is defined as follows:

$$\theta = \max\{\frac{1}{b_m} \|w_i\|^2 : i = 1,2, \ldots, M\} \tag{6.14}$$

The following auxiliary variables are introduced:

$$z_1 = x_1 - x_r \quad \text{(tracking error)} \tag{6.15}$$

$$z_2 = x_2 - \alpha_1 \tag{6.16}$$

The virtual control signal in equation (6.16) and the real control signal are constructed as:

$$\alpha_1 = -k_1(x_1 - x_r) + \dot{x}_r = -k_1 z_1 + \dot{x}_r \tag{6.17}$$

$$u(t) = -\left(k_2 + \frac{1}{2}\right)z_2 - \frac{1}{2a^2}\hat{\theta} z_2 \Phi^T(x)\Phi(x) \tag{6.18}$$

and the adaptive law can be defined as:

$$\dot{\hat{\theta}} = \frac{r}{2a^2}z_2^2 \Phi^T(x)\Phi(x) - \sigma\hat{\theta} \tag{6.19}$$

In the adaptive control law (6.18) and the parameter estimate law (6.19), k_1, k_2, a, r and σ are positive design parameters. In theory, the tracking error can be arbitrary small with an appropriate σ when reducing a and increasing r at the same time.

In order to design the control law and the parameter update law by using Lyapunov based methods, a Lyapunov function should be constructed. When trying to minimize the derivative of the Lyapunov function, both the control law (6.18) and the parameter estimate law (6.19) can be obtained. Appendix A demonstrates this derivation.

The following results assure that the control law (6.18) can stabilize the system (6.12) and proper selection of the design parameters can improve the system performance.

Theorem. With the assumptions 1 and 2, the responses of the closed loop system (6.12) and the controller defined in (6.18) are semi-globally uniformly ultimately bounded, and the following statements hold to be true:

(1) The asymptotic tracking error is given by

$$\|z_1\|^2_{r.m.s.,[t_0,\infty]} \leq \frac{1}{2a_0 k_1}\left(a^2 + \frac{\varepsilon^2}{b_m} + \frac{b_m \sigma}{r}\theta^2\right) \tag{6.20}$$

92

for any $t_0 \geq 0$.

(2) The transient tracking error is given by

$$\|z_1\|_{r.m.s.,[0,T]}^2 \leq \frac{b_m}{2k_1 r}\theta(0)^2 + \frac{d_0}{a_0{}^2 k_1 T} + \frac{1}{2a_0 k_1}\left(a^2 + \frac{\varepsilon^2}{b_m} + \rho^2\overline{d}^2 + \frac{b_m\sigma}{r}\theta^2\right) \quad (6.21)$$

where $d_0 = \frac{1}{2}\left(a^2 + \frac{\varepsilon^2}{b_m} + \frac{b_m\sigma}{r}\theta^2\right)$ and $a_0 = min\ (2k_1, 2k_2 b_m, \sigma)$

The proofs of the theorem are presented in Appendix A.

In order to reduce the tracking error (transient and asymptotic) either the design parameters k_1 and k_2 can be increased or the design parameter a can be decreased. However, these design parameters are used in the control laws such that improving the closed-loop performance may be done at the price of an increase in the control signal amplitude.

Chapter 7. Active Isolator

The aim of the chapter is to propose an active isolator. In this chapter, an active electromagnetic isolator is introduced. Numerical simulations are employed to compare the adaptive FNN controller with the three other controllers: Proportional-Plus-Derivative, Backstepping, and Adaptive Backstepping.

7.1 Active Electromagnetic Isolator

Recently, active-control base isolation systems have become more commonly applied to vibration control. A typical active-control base isolation system, as illustrated in Figure 1.2, is comprised of a passive isolator and an active controller. The physical characteristics of the passive device provide a passive resistance to vibration. The restoring force generated by the active controller gives an active resistance to vibration. Using a proper algorithm, the external disturbance exerted on the structure through the passive base isolation devices can be further reduced by the active controller. Such the hybrid scheme of combining a passive base isolation system with an active vibration control system attracts the interest of researchers from both structural and control engineering [70].

The tunable electromagnetic isolator can be easily reconfigured to obtain an active isolator. Figure 3.14 and Figure 7.1 illustrates the principles of the tunable isolator and the active isolator, respectively. The difference between the tunable isolator and the active isolator lies in the way of generating the electromagnetic forces F_{pf1} and F_{pf2}. For the tunbale isolator shown in Figure 3.14, the polarities of the electromagnets are such that the interacting forces F_{pf1} and F_{pf2} are opposing each other. For the active isolator shown in Figure 7.1, the polarities of the electromagnets are such that the interacting forces F_{pf1} and F_{pf2} are acting in the same direction. Apparently, when the electromagnets are not energized, the system becomes a passive isolator with the negative PM spring. To find the actuating force, assume that the two electromagnets of the active isolator have the same electrical characteristics and operate under the same conditions. When the PM is in the middle of the gap and the current to the electromagnets is zero, the net magnetic force on the PM is zero. When the electromagnets are energized and the PM moves to

the right of its equilibrium position by z , according to equation (2.22), the interaction force F_{pf1} and F_{pf2} given by:

$$F_{pf1} = sign(i)(1 - e^{-b_3|i|}) \frac{b_1}{(d_1+b_2)^4}$$

$$F_{pf2} = sign(i)(1 - e^{-b_3|i|}) \frac{b_1}{(d_2+b_2)^4}$$

where i is the EM current. Thus, the control force that is the electromagnetic force acting on the PM can be calculated by:

$$f_c = F_{pf1} + F_{pf2} \tag{7.1}$$
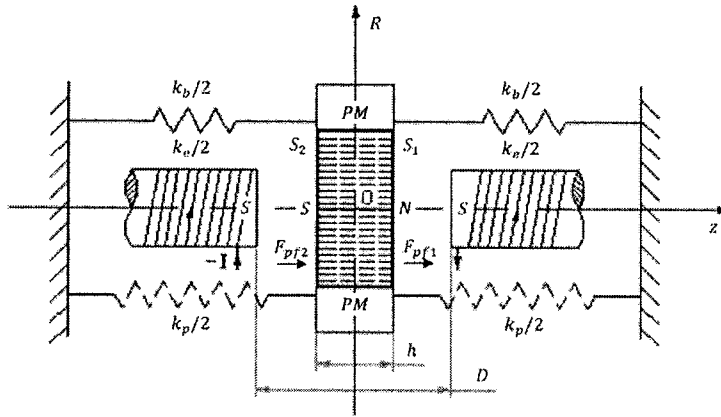
Figure 7.1   An electromagnetic actuator.

For the slight motion of the PM about the equilibrium position, the electromagnetic force acting on the PM can be approximated to the one when the PM is at the equilibrium position, namely, $d_1 = d_2 = (D - h)/2$. Thus, the equation (7.1) can be rewritten as:

$$f_c = sign(i)(1 - e^{-b_3|i|}) \frac{2b_1}{(0.5(D-h)+b_2)^4} \tag{7.2}$$

With the gap distance $D = 0.0680$ m, Figure 7.2 plots the EM current i as a function of the control force f_c. Through the curve fitting method, the EM current i can be determined by the control force f_c through equation (7.3).

$$i = 7.86 \times 10^{-2} f_c + 1.87 \times 10^{-4} f_c^3 \tag{7.3}$$

95
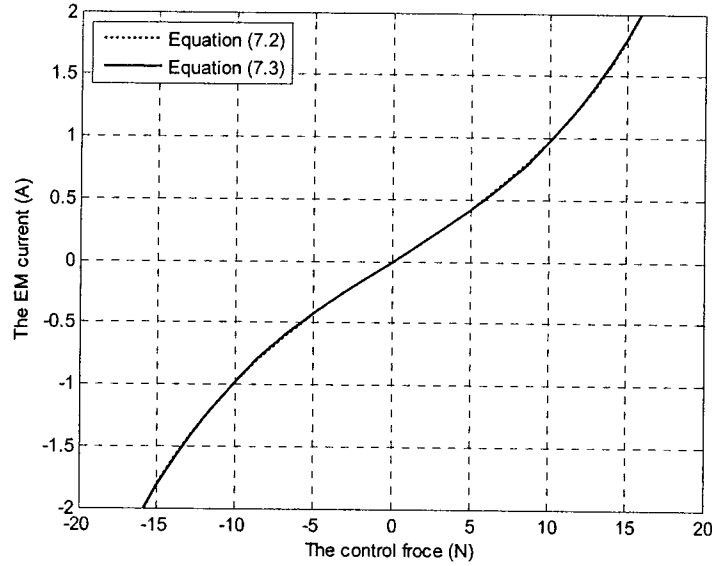
Figure 7.2   The EM current vs. the control force.

The active isolator shown in Figure 1.2 can be described by the following differential equation

$$m\ddot{z} + c\dot{z} + f_s(z) = -m\ddot{y} + f_c(t) \tag{7.4}$$

where z is the mass displacement relative to the moving base, m is the mass, c is the viscous damping coefficient, y is the base motion, $f_c(t)$ is the force generated by the active controller, and $f_s(z)$ describes a non-linear restoring force of the passive isolation spring. In this study, Equation (7.5) is made up to define the restoring force. The mathematical description of the restoring force is not considered a priori available for the control designer. In practice, the restoring function can be approximately obtained by an off-line identification procedure [47].

$$f_s(z) = 30z - 5.2 \times 10^5 z^3 + 6.8 \times 10^9 z^5 - 3.3 \times 10^{13} z^7 + 6.8 \times 10^{16} z^9 \tag{7.5}$$

Figure 7.3 presents the curve of non-linear restoring force. Figure 7.4 shows a typical base acceleration record (Taft's earthquake) [47] which will be used in this study. The mass m, which is not known for the control designer, is given as $0.10\,Kg$. The damping coefficient c is considered as an unknown parameter but lies in interval $[0 \quad c_{max}]$, where c_{max} is known. The nominal value of the damping coefficient is assumed to be $0.03\,Kg/s$.
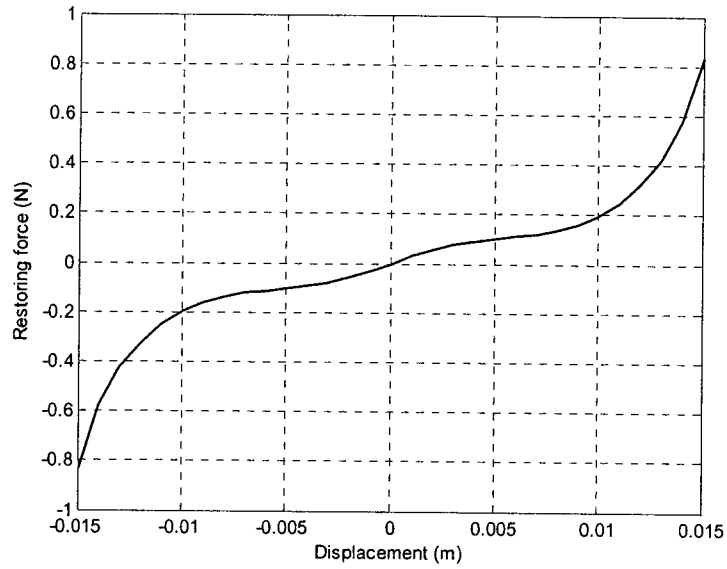
Figure 7.3   Non-linear restoring force versus displacement.
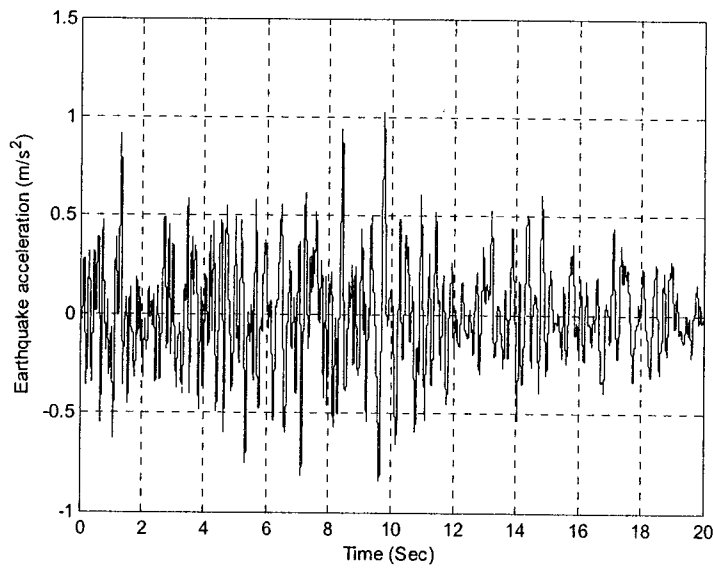
Figure 7.4   Taft's Earthquake Acceleration Signal.

Defining the state variables $(z_1, z_2) = (z, \dot{z})$, the system (7.4) can be rewritten as:

$$\begin{cases} \dot{z}_1 = z_2 \\ \dot{z}_2 = f(z_1, z_2) + u(t) - \ddot{y} \end{cases} \tag{7.6}$$

97

where $f(z_1, z_2) = -\frac{c}{m}z_2 - \frac{F_s(z_1)}{m}$, and $u(t) = \frac{f_c(t)}{m}$. With the initial condition $[z_1(0)\ z_2(0)] = [0\ 0]$, figure 7.5 shows the response of the open-loop system (7.6) that subjects to the Taft's earthquake signal.
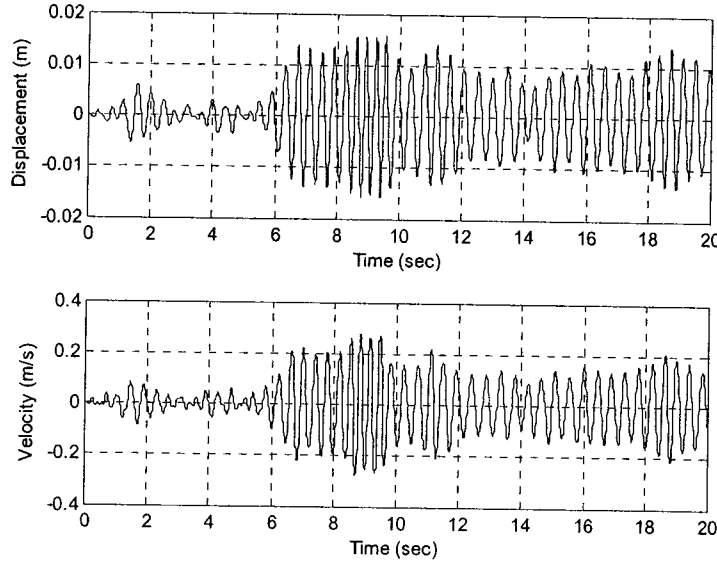
Figure 7.5   Open-loop response of system (7.6). (a), displacement; (b), velocity.

The Root-Mean-Square of the tracking error in the open loop is

$$\|z_1^{unc}\|_{r.m.s.,[0,T]} = 6.7564 \times 10^{-3}$$

where $z_1^{unc} = z_1$ is tracking error variable in open-loop because the reference signal $x_r = 0$. The tracking error variable in closed-loop is defined as: $z_1^{con} = z_1$.

In what follows, a computer simulation is conducted to investigate the effectiveness of the adaptive FNN controller in application to the system of (7.4). For the purpose of comparison, the three conventional controllers are also implemented. To quantify the performance, three numerical measures [47] are used:

(1) The Root-Mean-Square (r.m.s) value of a quantity q for a duration of T is defined as

$$\|q\|_{r.m.s.,[0,T]} \triangleq \sqrt{\frac{1}{T}\int_0^T q^2 dt} \qquad (7.7)$$

For example, the r.m.s value of the tracking error in the closed-loop system is:

98

$$\|z_1^{con}\|_{r.m.s.,[0,T]} \triangleq \sqrt{\frac{1}{T}\int_0^T (z_1^{con})^2 dt} \qquad (7.8)$$

The r.m.s value of the tracking error in the open-loop system is calculated by:

$$\|z_1^{unc}\|_{r.m.s.,[0,T]} \triangleq \sqrt{\frac{1}{T}\int_0^T (z_1^{unc})^2 dt} \qquad (7.9)$$

The r.m.s value of the control signal is calculated by:

$$\|u\|_{r.m.s.,[0,T]} \triangleq \sqrt{\frac{1}{T}\int_0^T u^2 dt} \qquad (7.10)$$

And, the r.m.s value of the base acceleration signal is calculated by:

$$\|\ddot{y}\|_{r.m.s.,[0,T]} \triangleq \sqrt{\frac{1}{T}\int_0^T \ddot{y}^2 dt} \qquad (7.11)$$

(2) $S_{r.m.s.,[0,T]}$ is a relative measure of the strength of the control action, which is defined by:

$$S_{r.m.s.,[0,T]} = \frac{\|u\|_{r.m.s.,[0,T]}}{\|\ddot{y}\|_{r.m.s.,[0,T]}} \qquad (7.12)$$

(3) $P_{r.m.s.,[0,T]}$ is a relative measure of the performance, which is computed by:

$$P_{r.m.s.,[0,T]} = \frac{\|z_1^{con}\|_{r.m.s.,[0,T]}}{\|z_1^{unc}\|_{r.m.s.,[0,T]}} \qquad (7.13)$$

7.2 Proportional-Plus-Derivative (PD) Control

First a PD control is examined. By linearizing equation (7.4), a second-order linear system is obtained as follows:

$$\ddot{z} + c/m\dot{z} + k_0/mz = u(t) - \ddot{y}(t) \qquad (7.14)$$

where $k_0 = 30 \ N/m$. The control action of a PD controller is defined by:

$$u(t) = -K_p(z(t) - x_r(t)) - K_d\dot{z}(t) \qquad (7.15)$$

where K_p is proportional gain, K_d is derivative gain, and x_r is the reference. Since the control objective is to mitigate the displacement response of the base, the reference is zero or $x_r = 0$. Given the maximum overshoot in the unit-step response is 15% and the settling time (at 2%) is 0.4 s, the K_p and K_d values are found to be 74.227 and 19.700, respectively. The PD controlled is

applied directly to the system (7.4). Figure 7.5 shows the response of the system. The quantitative measures of the control performance are given in Table 7.1.
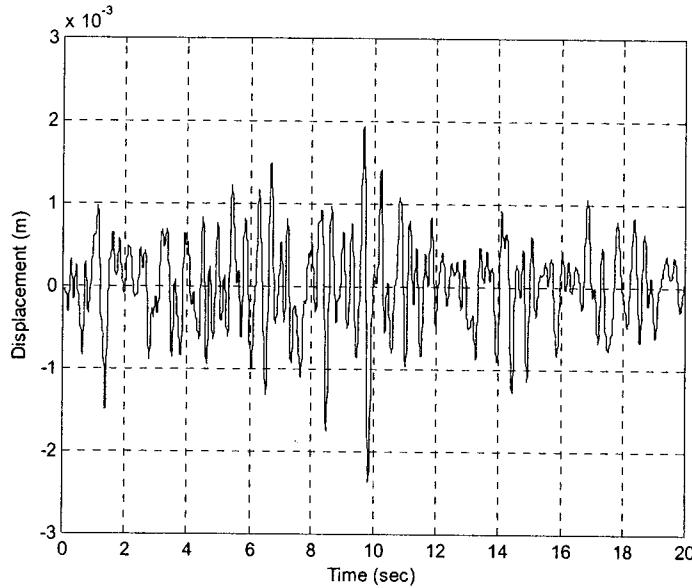
Figure 7.6   Response of the closed-loop system with the PD control.

7.3   Backstepping Controller

If the system is known, a backstepping controller can be used. Following the design procedure of the backstepping technique, it is easy to prove that if

$$u(t) = -(1 + k_1 k_2)z_1 - \left(k_1 + k_2 - \frac{c}{m}\right)z_2 + \frac{f_s(z_1)}{m} \tag{7.16}$$

the system (7.6) is stable. Comparing the two controllers (7.15) and (7.16), the proportional gain and the derivative gain of the PD controller are related to the constants k_1 and k_2 by

$$K_p = 1 + k_1 k_2 \tag{7.17}$$

$$K_d = k_1 + k_2 - \frac{c}{m} \tag{7.18}$$

Thus, k_1 and k_2 are chosen such that $K_p = 74.227$ and $K_d = 19.700$. Figure 7.7 shows the response of the closed-loop system. The quantitative measures of the control performance are given in Table 7.1.

100
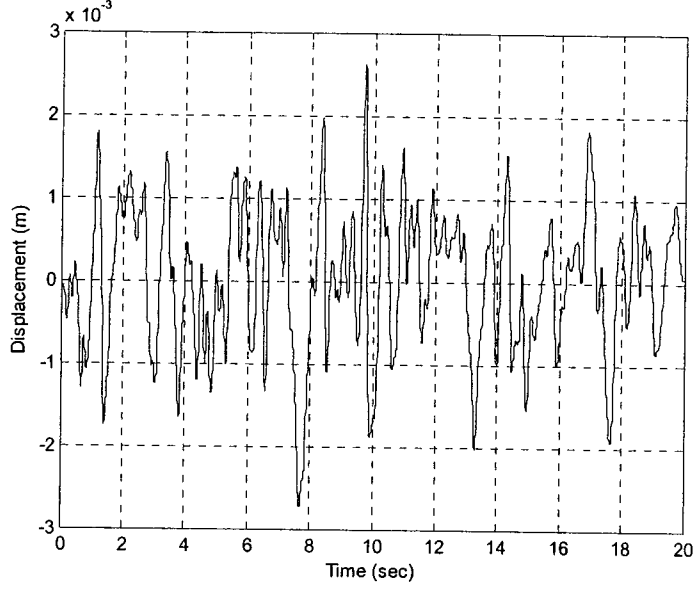
Figure 7.7   Response of the system with the backstepping controller.

7.4   Adaptive Backstepping Controller

If the system parameters are unknown, an adaptive backstepping controller can be used. In [47], an adaptive backstepping controller was presented. To understand the difference between this controller and the adaptive FNN backstepping controller, the design procedure presented in [47] is briefly presented below. Rearrangment of equation (7.6) yields

$$\begin{cases} \dot{z}_1 = z_2 \\ \dot{z}_2 = -\frac{c}{m}z_2 - \frac{f_s(z_1)}{m} - \ddot{y}(t) + u(t) \end{cases} \tag{7.19}$$

Assume that the system parameters $c, m,$ and a mathematical description of the restoring force $f_s(z_1)$ are unknown to the control designer. It is possible to approximate the restoring force by an $(2n + 1)$-order least-squares regression polynomial:

$$f_s(z_1) \triangleq \delta_1\left(\frac{z_1}{d}\right) + \delta_2\left(\frac{z_1}{d}\right)^3 + \cdots + \delta_n(\frac{z_1}{d})^{2n+1} + R_e(z_1) \tag{7.20}$$

where d is a known constant with the dimension of a displacement, δ_i is coefficient of the polynomial and $R_e(z_1)$ is a residual function. The coefficient δ_i and the function $R_e(z_1)$ are

101

unknown to the controller designer, but must be bounded in the form $|R_e(z_1)| \leq \bar{R}_e$, where $\bar{R}_e$ is a known positve constant. Substitution equation (7.20) into equation (7.19) yields

$$\begin{cases} \dot{z}_1 = z_2 \\ \dot{z}_2 = \Phi(z_1, z_2)^T \Theta + R(z_1) - \ddot{y}(t) + u(t) \end{cases} \tag{7.21}$$

with $\Phi(z_1, z_2) = -\left(\frac{z_2}{v}, \frac{z_1}{d}, \frac{z_1^3}{d^3}, \cdots, \frac{z_1^{2n+1}}{d^{2n+1}}\right)^T$, $\Theta = \left(\frac{cv}{m}, \frac{\delta_1}{m}, \frac{\delta_2}{m}, \cdots, \frac{\delta_n}{m}\right)^T$, $R(z_1) = \frac{R_e(z_1)}{m}$ where v is a known constant which has a the dimension of a velocity and is introduced to have dimensionless variables in Φ and Θ. From Figue 7.5, these values are chosen to be $d = 0.020\ m$ and $v = 0.40\ m/s$.

In practice, the restoring force defined in equation (7.5) is unknown to the control designer. In this study, a fifth-order least-squares regression polynomial is used to approximate the restoring force:

$$\Psi(z) = 0.3\left(\frac{z}{d}\right) - 0.8\left(\frac{z}{d}\right)^3 + 2.0\left(\frac{z}{d}\right)^5 \tag{7.22}$$

Figure 7.8 compares the restoring force and its regresion polynomial. The bound $\bar{R}_e$ of $R_e(z_1)$ can be found to be

$$\bar{R}_e = max|f_s(z_1) - \Psi(z_1)| = 0.4724$$
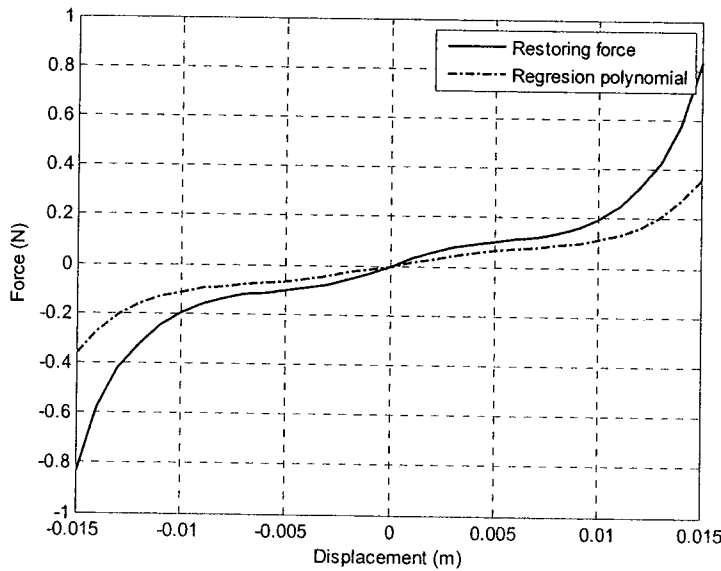
Figure 7.8 Nonlinear restoring force.

102

The adaptive control law and parameter estimate law in [47] can be written as

$$u(t) = -(1 + k_1 k_2)z_1 - (k_1 + k_2)z_2 - \Phi(z_1, z_2)^T \hat{\theta}$$
$$-sg(z_2)cf(|rz_2|)r + (1 + k_1 k_2)x_r$$
$$+(k_1 + k_2)\dot{x}_r + \ddot{x}_r \tag{7.23}$$

$$\dot{\hat{\theta}} = \Gamma\Phi(z_1, z_2)z_2 - \Gamma\sigma_\Theta(\|\hat{\theta}\|)\hat{\theta} \tag{7.24}$$

$$\hat{\theta}(0) = \hat{\theta}_0 \tag{7.25}$$

Figure 7.4 shows that the excitation is bounded in the form $|\ddot{y}(t)| \leq 1.2$. Then $r = A + \frac{\bar{R}_e}{m} = 5.9240$. The nominal values of model (7.21) can be assumed as $c^{(nom)} = 0.03$ and $\Theta_\delta{}^{(nom)} = (0.3 \quad -0.8 \quad 2.0)^T$. By adding a 100% of uncertainty to $c^{(nom)}$ and $\Theta_\delta{}^{(nom)}$, respectively, the following statements are obtained:

$$0 \leq c \leq c_{max} = 2c^{(nom)} = 0.06$$

$$\|\Theta_\delta\| \leq M_\delta = 2\|\Theta^{(nom)}\| = 4.3498$$

with these values, the bound M, which is required to design the controller [47], can be computed through:

$$M = \sqrt{\left(\frac{c_{max}v}{m}\right)^2 + M_\delta{}^2} = 4.3564$$

For the parameter adaptive law, the following initial parameter vector $\hat{\theta}_0$, which is defined in equation (7.25), has been chosen

$$\hat{\theta}_0 = \left(\frac{c_{max}v}{m}, \Theta^{(nom)T}\right)^T$$

The constants k_1 and k_2 are chosen such that $K_p = 1 + k_1 k_2 = 74.227$ and $K_d = k_1 + k_2 = 19.700$. After some numerical experiments, the following design parameters are chosen: $\varepsilon_1 = 0.001$, $\varepsilon_2 = 0.1$, $\bar{\sigma} = 1$ and $\Gamma = I_5$. Figure 7.9 shows the system response. Figure 7.10 illustrates the time adaptation of the estimate parameters. The quantitative measures of the control performance are given in Table 7.1.

Figure 7.9   Response (dotted line) with the adaptive backstepping controller and the response (solid line) with the adaptive FNN controller.
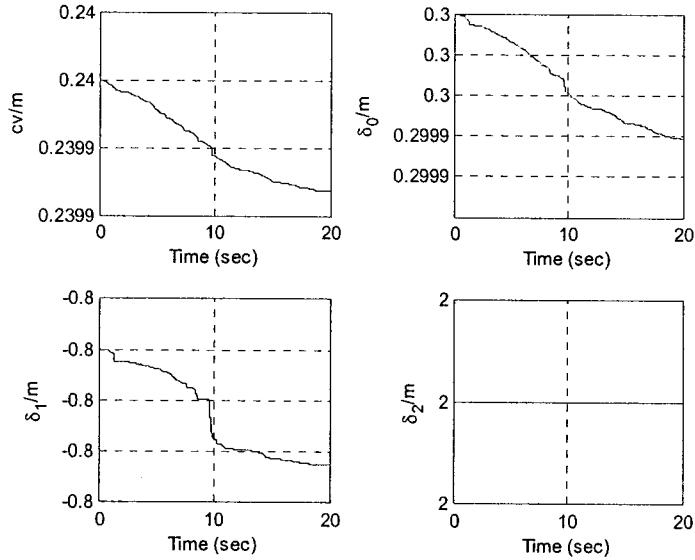
Figure 7.10   The parameter estimation history.

7.5   Adaptive FNN Controller

The controller defined by (6.18) and (6.19) can be rewritten as:

$$u(t) = -\left(k_1 k_2 + \tfrac{1}{2}k_1\right)z_1 - \left(\tfrac{1}{2} + k_2\right)z_2 - \tfrac{1}{2a^2}\hat{\theta}z_2\Phi^T(z)\Phi(z) \qquad (7.26)$$

The constants k_1 and k_2 are chosen such that $K_p = k_1 k_2 + \frac{1}{2}k_1 = 74.227$ and $K_d = \frac{1}{2} + k_2 = 19.700$. The response of the closed-loop system with the PD controller indicates that the displacement is in the range [-0.0030 0.0030] m and the velocity is in the range [-0.050 0.050] m/s. To build the FNN approximator without any linguistic rules, define five fuzzy sets over the range [-0.0030, 0.0030] for the displacement variable z_1 and five fuzzy sets over the range [-0.050, 0.050] for the velocity variable z_2. The membership functions are chosen as following:

$$\mu_{F_1^1}(z_1) = e^{-\frac{(z_1+0.0030)^2}{0.00001}}, \quad \mu_{F_1^2}(z_1) = e^{-\frac{(z_1+0.0015)^2}{0.00001}}, \quad \mu_{F_1^3}(z_1) = e^{-\frac{(z_1+0.0000)^2}{0.00001}},$$

$$\mu_{F_1^4}(z_1) = e^{-\frac{(z_1-0.0015)^2}{0.00001}}, \quad \mu_{F_1^5}(z_1) = e^{-\frac{(z_1-0.0030)^2}{0.00001}},$$

$$\mu_{F_2^1}(z_2) = e^{-\frac{(z_2+0.050)^2}{0.0001}}, \quad \mu_{F_2^2}(z_2) = e^{-\frac{(z_2+0.025)^2}{0.0001}}, \quad \mu_{F_2^3}(z_2) = e^{-\frac{(z_2+0.000)^2}{0.0001}},$$

$$\mu_{F_j^4}(x_j) = e^{-\frac{(z_2-0.025)^2}{0.0001}}, \quad \mu_{F_j^5}(x_j) = e^{-\frac{(z_2-0.050)^2}{0.0001}}.$$

According to equation (6.2),

$$\emptyset_1(z) = \frac{e^{-\frac{(z_1+0.0030)^2}{0.00001}-\frac{(z_2+0.050)^2}{0.0001}}}{\sum_{i=1}^{5}(\prod_{j=1}^{2}\mu_{F_j^i}(z_j))}$$

$$\emptyset_2(z) = \frac{e^{-\frac{(z_1+0.0015)^2}{0.00001}-\frac{(z_2+0.025)^2}{0.0001}}}{\sum_{i=1}^{5}(\prod_{j=1}^{2}\mu_{F_j^i}(z_j))}$$

$$\emptyset_3(z) = \frac{e^{-\frac{(z_1+0.0000)^2}{0.00001}-\frac{(z_2+0.000)^2}{0.0001}}}{\sum_{i=1}^{5}(\prod_{j=1}^{2}\mu_{F_j^i}(z_j))}$$

$$\emptyset_4(z) = \frac{e^{-\frac{(z_1-0.0015)^2}{0.00001}-\frac{(z_2-0.025)^2}{0.0001}}}{\sum_{i=1}^{5}(\prod_{j=1}^{2}\mu_{F_j^i}(z_j))}$$

$$\emptyset_5(z) = \frac{e^{-\frac{(z_1-0.0030)^2}{0.00001}-\frac{(z_2-0.050)^2}{0.0001}}}{\sum_{i=1}^{5}(\prod_{j=1}^{2}\mu_{F_j^i}(z_j))}$$

The equations (6.18), (6.20) and (6.21) indicate that the effectiveness of the controller depends on the values of the design parameters. After several trials, the other design parameters

are chosen as: $a = 0.002, r = 30$ and $\sigma = 0.01$. The initial conditions for the parameter estimation is selected $\hat{\theta}_0 = 0$. Figure 7.9 shows the response of the system with disturbance while the reference signal is zero, and Figure 7.11 illustrates the adaptation of the estimate parameter. The quantitative measures of the control performance are given in Table 7.1.
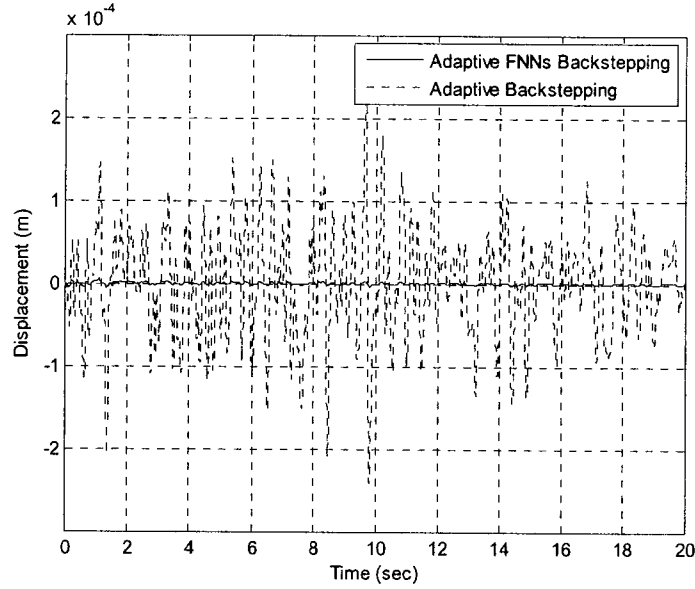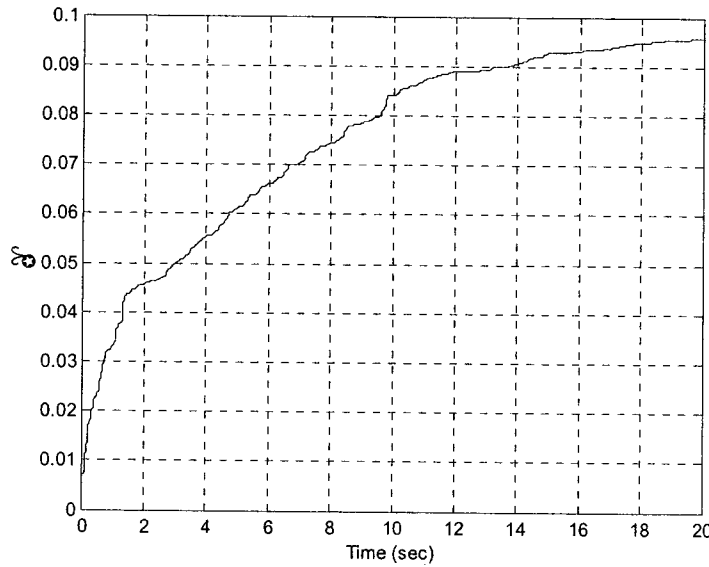

Figure 7.11   The parameter estimation history.

Table 7.1 summarizes the compared data results for the simulation in the above four cases. By using the same proportional gain and derivative gain, the adaptive FNN controller can obtain the best performance among the four techniques. Compared to adaptive backstepping controller and backstepping controller, the adaptive FNN controller improved the closed-loop behaviour without increasing the control signal amplitude.

Table 7.1   Comparison results for simulations in Chapter 7.

Controller	$\|z_1^{con}\|_{r.m.s.,[0,T]}$	$S_{r.m.s.,[0,T]}$	$P_{r.m.s.,[0,T]}$
PD	5.4112×10^{-4}	7.5740×10^{-1}	8.0100×10^{-2}
Backstepping	8.6452×10^{-4}	1.0349×10^{0}	1.2800×10^{-1}
Adaptive Backstepping	6.4374×10^{-5}	1.0030×10^{0}	9.5000×10^{-3}
Adaptive FNN Backstepping	1.3522×10^{-6}	1.0005×10^{0}	2.0014×10^{-4}

106

Chapter 8.   Conclusions and Future Works

This part has applied an adaptive fuzzy-neural networks backstepping controller to active control of a nonlinear isolator. This chapter summarizes the overall conclusions of this part and gives recommendations for future work.

8.1   Conclusions

The controller can handle the system that possesses a wide class of uncertainties with no prior knowledge of the bounding functions. FNNs are used to approximate uncertain functions and the backstepping technique is employed to construct the controller. The controller ensures that the response of the controlled systems are semi-globally uniformly ultimately bounded and the tracking error can be made arbitrarily small by an appropriate selection of design parameters. The main feature of the FNN controller is that no matter how many artificial neurons or fuzzy rules are used, the number of the online adaptive parameters is not more than the order of the original system. The controller is compared with the three other controllers: PD, backstepping, and adaptive backstepping. The results show that the adaptive FNN backstepping controller outperforms the other three controllers in terms of the vibration suppression and requires a control effort similar to those of the three controllers.

8.2   Future Works

The study presented in this thesis is only a preliminary step towards adaptive control using fuzzy-neural networks for an active isolator. Much future work remains.

(1) In order to be consistent with Part I, the base excitation and other disturbances should be measured as displacement signals. The displacement transmissibility ratio can still be an index of the isolation performance;

(2) How the design parameters affect the isolator performance should be investigated. This can be a guide to choose the values of these parameters;

(3) The indirect method used in this part approximates the uncertainties by using FNN. The controller always has a linear part that may overshadow the advantage of the FNN

mechanism. The direct method uses FNN to approximate the desired but unknown control input signal, consequently, to construct the available virtual control signal. Thus, the direct method is thought to be worth of further study;

(4) The nonlinearity of the mechanical spring has effects on the performance of the passive isolator. There is an obvious extension to investigate the effects of the nonlinearity of the beam to the active isolator;

(5) An experiment study on the active isolator should be undertaken to verify all the numerical simulation results.

Reference

[1] Inman, D.J., *Engineering Vibration,* 2nd edition, Prentice-Hall, New Jersey, 2001.

[2] Norton, M.P. and Karczub, D.G., *Fundamentals of Noise and Vibration Analysis for Engineers,* 2nd edition, Cambridge University, 2003.

[3] Kovacica, I., Brennanb, M.J. and Waters, T.P., A study of a nonlinear vibration isolator with a quasi-zero stiffness characteristic, *Journal of Sound and Vibration,* 315:700-711, 2007.

[4] Mead, D.J., *Passive Vibration Control,* John Wiley & Sons, Chichester, 1999.

[5] Sjöberg, M., *On Dynamic Properties of Rubber Isolators,* Doctoral thesis, Kungl Tekniska Högskolan, Department of Vehicle Engineering, 2003.

[6] Richards, C.M. and Singh, R., Characterization of Rubber Isolator Nonlinearities in the Nonlinearities in the Context of Single- and Multi-Degree-of-Freedom Experimental Systems, *Journal of Sound and Vibration,* 247:807-834, 2001.

[7] Derby, T.F. and Calcaterra, P.C., Response and optimization of an isolator with relaxation type damping, *Shock and Vibration Bulletin,* 40:203–216, 1970.

[8] Brennan, M.J., Carrella, A., Waters, T.P. and Lopes, V., On the dynamic behaviour of a mass supported by a parallel combination of a spring and an elastically connected damper, *Journal of Sound and Vibration,* 309:823-837, 2008.

[9] Rivin, E.I., *Passive Vibration Isolation,* ASME, New York, 2001.

[10] Carrella, A., Brennan, M.J. and Waters, T.P., Static analysis of a passive vibration isolator with quasi-zero-stiffness characteristic, *Journal of Sound and Vibration,* 301:678-689, 2007.

[11] Carrella, A., Brennan, M.J., Waters, T.P. and Shin, K., On the design of a high-static–low-dynamic stiffness isolator using linear mechanical springs and magnets, *Journal of Sound and Vibration,* 315:712-720, 2008.

[12] Yan, B., *Active Vibration Isolation with a Distributed Parameter Isolator,* PHD Thesis, ISVR, University of Southampton, 2007.

[13] Hansen, C.H. and Snyder, S.D., *Active Control of Noise and Vibration,* 2nd Edition, E&FN Spon, London, 1997.

[14] Serrand, M. and Elliott, S.J., Multichannel Feedback Control for the Isolation of Base-Excited Vibration, *Journal of Sound and Vibration*, 234:681-704, 2000.

[15] Sciulli, D., Isolation Design for a Flexible System, *Journal of Sound and Vibration*, 234:681-704, 2000.

[16] Sugahara, R., Masuzawa, M. and Yamaoka, H., Performance of an Active Vibration Isolation System, *IWAA2004, CERN*, Geneva, 2004.

[17] Stöbener, U. and GmbH, H., Active Vibration Isolation for highly Sensitive Measurement Equipment, *Adaptronic Congress*, Göttingen, 2006.

[18] Yoshioka, H. and Murai, N., An Active Microvibration Isolation System, *Proceedings of the 7th International Workshop on Accelerator Alignment, SPring-8*, 2002

[19] Benassi, L. and Elliott, S.J., Active vibration isolation using an inertial actuator with local displacement feedback control, *Journal of Sound and Vibration*, 278:705-724, 2004.

[20] Robertson, W., Wood, R., Cazzolato, B. and Zander, A., Zero-stiffness magnetic springs for active vibration isolation, *Proceedings of International Symposium on Active Noise and Vibration Control*, Australia, 2006.

[21] Hoque, M.E., Takasaki, M., Ishino, Y., Suzuki, H. and Mizuno, T., An Active Micro Vibration Isolator with Zero-Power Controlled Magnetic Suspension Technology, *JSME International Journal Series C*, 49:719-726, 2006.

[22] Mizuno, T., Takasaki, M., Kishita, D., and Hirakawa, K., Vibration isolation system combining zero-power magnetic suspension with springs, *Control Engineering Practice*, 15:187–196, 2007.

[23] Xing, J.T., Xiong, Y.P. and Price, W.G., Passive-active vibration isolation systems to produce zero or infinite dynamic modulus: theoretical and conceptual design strategies, *Journal of Sound and Vibration*, 286:615-636, 2005.

[24] Zhao, C., Zhu, S. and He, Q., Fuzzy-PID Control Method for Two-Stage Vibration Isolation System, *Journal of Theoretical and Applied Mechanics*, 45:171-177, 2007.

[25] Rida, I.M., Active Vibration Isolation System Based on Artificial Neural Network, *Journal of Applied Sciences*, 4:140-143, 2004.

[26] Liu, Y., Waters, T.P. and Brennan, M.J., A comparison of semi-active damping control strategies for vibration isolation of harmonic disturbances, *Journal of Sound and Vibration*, 280:21-39, 2005.

[27] Spencer Jr., B.F., Dyke, S.J., Sain, M.K. and Carlson, J.D., Phenomenological Model of a Magnetorheological Damper, *Journal of Engineering Mechanics*, 123:230-238, 1997.

[28] Liu, K., Liu, J. and Liao, L., Application of a tunable electromagnetic damper in suppression of structural vibration, *the Trans. of the CSME*, 30:41-62, 2006.

[29] Liu, K., Liao, L. and Liu, J., Comparison of two Auto-tuning Methods for a Variable Stiffness Vibration Absorber, *the Trans. of the CSME*, 29:81-96, 2005

[30] Jin, D., Chen, J. and Jun, H., Analysis and Design of Device of Electrorheological/ Magetorheological Fluid with Variable Stiffness, *Proceedings of SPIE*, 3201:204-212, Pittsburgh, 1997.

[31] Wang, M., Chen, B., Liu, K., Liu, X. & Zhang, S., Adaptive fuzzy tracking control of nonlinear time-delay systems with unknown virtual control coefficients, *Information Science*, 178:4326-4340, 2008.

[32] Wang, M., Chen, B., Liu, X. and Shi, P., Adaptive fuzzy tracking control for a class of perturbed strict-feedback nonlinear time-delay systems, *Fuzzy Sets and Systems*, 159:949-967, 2008.

[33] Craik, D.J., *Magnetism: Principles and Applications*, Wiley, Chichester, New York, 1995.

[34] Zedler, T., Nikanorov, A. and Nacke, B., Investigation of relative magnetic permeability as input data for numerical simulation of induction surface hardening, *International Scientific Colloquium, Modelling for Electromagnetic Processing*, Hannover, 2008.

[35] Lin, C. and Jou, H., Force Model Identification for Magnetic Suspension Systems via Magnetic Field Measurement. *IEEE Trans. On Instrumentation and Measurement*, 42:767-771, 1993.

[36] Liu, J. and Liu, K., A Tunable Electromagnetic Vibration Absorber: Characterization and Application, *Journal of Sound and Vibration*, 296:708-724, 2006.

[37] Woodson, H.H. and Melcher, J.R., *Electromechanical Dynamics—part I: Discrete Systems*, Wiley, New York, 1968.

[38] Liu, J., *Design and Implementation of a Tunable Absorber and a Time – Delayed Vibration Absorber*, Msc thesis, lakehead University, 2005.

[39] He, Y., *Non-collocated Control of Vibration of a Three-DOF Structure Using the Electromagnetic Vibration Absorber*, Msc thesis, lakehead University, 2007.

111

[40] Lin, C. and Lin, K., Implementation and Control of the Magnetic Linear Actuation System, *16th IEEE International Conference on Instrumentation and Measurement Technology*, Baltimore, 2000.

[41] Azzouz, Y. and Mouillet, A., How to Characterize Soft Magnetic Materials by Measuring Magnetic Flux Density in a Rotating Field Apparatus, *IEEE Trans. On Magnetics*, 38:1477-1480, 2002.

[42] Biller, H., Moving Meshes for Electromagnets, *2006 Comsol User Conference*, Frankfurt, 2006.

[43] Coyle, M.F. and Keel, C.G., A Combined Stress Experiment Using a Hacksaw, *The International Journal of Modern Engineering*, 2001.

[44] Carrella, A., *Passive Vibration Isolators with High-Static-Low-Dynamic-Stiffness*. PHD Thesis, ISVR, University of Southampton, 2008.

[45] *AC/DC Module User's Guide*, Comsol Multiphysics, 2006.

[46] *AC/DC Module Model Library*, Comsol Multiphysics, 2006.

[47] Manosa, V., Ikhouane, F. and Rodellar, J., Control of Uncertain Non-linear System via Adaptive Backstepping, *Journal of Sound and Vibration*, 280:657-680, 2005.

[48] Yang, Y., Feng, G. and Ren, J., A Combined Backstepping and Small-Gain Approach to Robust Adaptive Fuzzy Control for Strict-Feedback Nonlinear Systems, *IEEE Trans. on Systems, Man, and Cybernetics-Part A: Systems and Humans*, 34:406-420, 2004.

[49] Pomet, J.B. and Praly, L., Adaptive nonlinear regulation: Estimation from the Lyapunov equation, *IEEE Trans. on Automatic Control*, 37:729–740, 1992.

[50] Taylor, D.G., Kokotovic, P.V., Marino, R. and Kanellakopoulos, I., Adaptive regulation of nonlinear systems with unmodeled dynamics, *IEEE Trans on Automatic Control*, 34:405–421, 1989.

[51] Schoenwald, D.A. and Ozguner, U., Robust Stabilization of Nonlinear Systems with Parametric Uncertainty, *IEEE Trans. on Automatic Control*, 39:405–421, 1994.

[52] Barmish, B.R. and Leitmann, G., On ultimate boundedness control of uncertain systems in the absence of matching assumptions, *IEEE Trans. on Automatic Control*, 27:153-158, 1982.

[53] Doyen, L. and Seube, N., Control of Uncertain Systems under Bounded Chattering, *Dynamics and Control*, 8:163-176, 1998.

[54] Hornik, K., Stinchcombe, M., and White, H., Multi-layer feedforward networks are universal approximators. *Neural Networks*, 2:359–366, 1989.

[55] Scarselli, F., and Tsoi, A.C., Universal Approximation Using Feedforward Neural Networks: A Survey of Some Existing Methods and Some New Results, *Neural Networks*, 11:15–37, 1998.

[56] Zhang, Y., Peng, P. and Jiang, Z., "Stable Neural Controller Design for Unknown Nonlinear Systems Using Backstepping," *IEEE Trans. on Neural Networks*, 11:1347-1359, 2000.

[57] Wang, L., Fuzzy Systems Are Universal Approximators, *Fuzzy Systems, IEEE International Conference*, 1992

[58] Yu, S., Yu, X. and Man, Z., A Fuzzy Neural Network Approximator with Fast Terminal Sliding Mode and its Applications, *Fuzzy Sets and Systems*, 148:469-486, 2004.

[59] Buckley, J. and Hayashi, Y., Can Fuzzy Neural Nets Approximate Continuous Fuzzy Functions?, *Fuzzy Sets and Systems*, 61:43-52, 1994.

[60] Feuring, T. and Lippe, W.M., Fuzzy Neural Networks are Universal Approximators, *IFSA World Congress*, Sao Paulo, Brasil, 2:659-662, 1995.

[61] Spooner, J.T. and Passino, K.M., Stable Adaptive Using Fuzzy Systems and Neural Networks, *IEEE Trans. on Fuzzy Systems*, 4:339-359, 1996.

[62] Passino M. and Yurkovich, S., *Fuzzy Control*, Reading, MA: Addison-Wesley, 1998.

[63] Lee, C., Fuzzy Logic in Control Systems: Fuzzy Logic Controller – Part I, *IEEE Trans. on system*, 20:404-418, 1990.

[64] Wang, L., Stable Adaptive Fuzzy Controllers with Application to Inverted Pendulum Tracking, *IEEE Trans. on Fuzzy Systems*, 1:146-155, 1993.

[65] Jain, A.K., Mao, J. and Mohiuddin, K.M. Artificial Neural Networks: A Tutorial, *IEEE Computer*, 29:31-44, 1996.

[66] Shiguemori, E.H., and Chiwiacowsky, L.D., An Inverse Vibration Problem Solved by an Artificial Neural Network, *TEMA Tend. Mat. Apl. Comput.*, 6:163-175, 2005.

[67] Haykin, S., *Neural Networks: A Comprehensive Foundation*, Macmillan, New York, 1993.

[68] Nadler, M. and Smith, E.P., *Pattern Recognition Engineering*, John Wiley & Sons, New York, 1993.

[69] Zhang, J. and Morris, A.J., Fuzzy neural networks for nonlinear systems modelling, *Control Theory and Applications, IEE Proceedings*, 142:551-561, 1995.

[70] Kelly, J., Leitmann, G. and Soldatos, A., Robust Control of Base-isolated Structures under Earthquake Excitation, *Journal of Optimization Theory and Applications*, 53:159-181, 1997.

[71] Krstic, M., Kanellakopoulos, I. and Kokotovic, P., *Nonlinear and adaptive control design*, New York: Wiley, 1995.

[72] Ikhouane, F., Mañosa, V. and Rodellar, J., "Adaptive backstepping control of a class of uncertain nonlinear systems. Application to Bouc-Wen hysteretic oscillators," *Automatica*, 41:225–231, 2005.

Appendix A

Proofs of the main results

Lemma 1.

Let $\hat{\theta}(t)$ to be a continuous function defined in the adaptive law (6.19). If there exists an initial condition $\hat{\theta}(0) \geq 0$, then $\hat{\theta}(t) \geq 0$ where $t \geq 0$

Proof.

From equation (6.19), the following is obtained:

$$\dot{\hat{\theta}} \geq -\sigma\hat{\theta}$$

Multiplying both sides of the above inequity by $e^{\sigma t}$ yields

$$\dot{\hat{\theta}}e^{\sigma t} \geq -\sigma\hat{\theta}e^{\sigma t}$$

$$\dot{\hat{\theta}}e^{\sigma t} + \sigma\hat{\theta}e^{\sigma t} \geq 0$$

$$\frac{d}{dt}\left(\hat{\theta}e^{\sigma t}\right) \geq 0$$

Integrating at both sides of the above inequality, gives

$$\int_0^t \frac{d}{dt}\left(\hat{\theta}e^{\sigma t}\right) \geq 0$$

$$\hat{\theta}(t)e^{\sigma t} - \hat{\theta}(0)e^{\sigma *0} \geq 0$$

$$\hat{\theta}(t)e^{\sigma t} \geq \hat{\theta}(0)$$

Since
$$\hat{\theta}(0) \geq 0 \text{ and } e^{\sigma t} \geq 0,$$

$$\hat{\theta}(t) \geq 0 \text{ for all } t \geq 0$$

which ends the proof of lemma 1.

Lemma 2.

Let A and B be any row vector and column vector, respectively, with appropriate dimension then

$$AB \leq \frac{1}{2\rho^2}|A|^2 + \frac{\rho^2}{2}|B|^2$$

Proof.

Since A is a row vector and B is a column vector, and they have same number of elements, and if $AB \geq 0$ then

$$AB = |AB|$$

If $AB < 0$ then $AB < |AB|$.

On the basis of the property of the vector, we have

$$|AB| \leq |A||B|$$

Since

$$(\frac{|A|}{\rho} - \rho|B|)^2 \geq 0 \qquad \text{where } \rho \text{ is any nonzero real number}$$

$$\frac{|A|^2}{\rho^2} - 2|A||B| + \rho^2|B|^2 \geq 0$$

$$|A||B| \leq \frac{1}{2\rho^2}|A|^2 + \frac{\rho^2}{2}|B|^2$$

Thus

$$AB \leq \frac{1}{2\rho^2}|A|^2 + \frac{\rho^2}{2}|B|^2$$

which ends the proof of lemma 2.

Proof of Theorem 1

Step 1. Consider a Lyapunov's function candidate as:

$$V_1 = \frac{1}{2} z_1^2 \tag{A.1}$$

Differentiating V_1 yields:

$$
\begin{aligned}
\dot{V}_1 &= z_1 \dot{z}_1 \\
&= z_1 (\dot{x}_1 - \dot{y}_r) \\
&= z_1 (x_2 - \alpha_1 - \dot{y}_r + \alpha_1)
\end{aligned}
$$

Using equation (6.16) $z_2 = x_2 - \alpha_1$ and equation (6.17) $\alpha_1 = -k_1 z_1 + \dot{y}_r$, the following is obtained:

$$
\begin{aligned}
\dot{V}_1 &= z_1 (z_2 - k_1 z_1) \\
&= -k_1 z_1^2 + z_1 z_2
\end{aligned}
$$

Step 2. Choose a Lyapunov's function candidate as:

$$V_2 = V_1 + \frac{1}{2} z_2^2 + \frac{b_m}{2r} \tilde{\theta}^2 \tag{A.2}$$

where $\tilde{\theta} = \theta - \hat{\theta}$ is parameter estimation error. Differentiating V_2 yields:

$$\dot{V}_2 = \dot{V}_1 + z_2 \dot{z}_2 + \frac{b_m}{r} \tilde{\theta} \dot{\tilde{\theta}}$$

Equation (6.14) indicates θ is a constant, thus $\dot{\theta} = 0$. Then $\dot{\tilde{\theta}} = -\dot{\hat{\theta}}$ is obtained. Therefore,

$$
\begin{aligned}
\dot{V}_2 &= \dot{V}_1 + z_2 (\dot{x}_2 - \dot{\alpha}_1) - \frac{b_m}{r} \tilde{\theta} \dot{\hat{\theta}} \\
&= -k_1 z_1^2 + z_1 z_2 + z_2 (f(x) + g(x)u(t) + d(t) - \dot{\alpha}_1) - \frac{b_m}{r} \tilde{\theta} \dot{\hat{\theta}} \\
&= -k_1 z_1^2 + z_2 d(t) + z_2 (f(x) + g(x)u(t) - \dot{\alpha}_1 + z_1) - \frac{b_m}{r} \tilde{\theta} \dot{\hat{\theta}}
\end{aligned}
$$

Using Lemma 2, then
$$z_2 d(t) \leq \frac{1}{2\rho^2} z_2^2 + \frac{1}{2} \rho^2 d^2$$

$$\leq \frac{1}{2\rho^2} z_2^2 + \frac{1}{2} \rho^2 \bar{d}^2 \quad \text{where } \rho \text{ is any nonzero real number}$$

Therefore,

$$\dot{V}_2 \leq -k_1 z_1^2 + \frac{1}{2\rho^2} z_2^2 + \frac{1}{2}\rho^2 \overline{d}^2 + z_2(f(x) + g(x)u(t) - \dot{\alpha}_1 + z_1) - \frac{b_m}{r}\tilde{\theta}\dot{\hat{\theta}}$$

$$= -k_1 z_1^2 + \frac{1}{2}\rho^2 \overline{d}^2 + z_2\left(f(x) - \dot{\alpha}_1 + z_1 + \frac{1}{2\rho^2} z_2 + g(x)u(t)\right) - \frac{b_m}{r}\tilde{\theta}\dot{\hat{\theta}}$$

Define $\overline{f}(x) = f(x) - \dot{\alpha}_1 + z_1 + \frac{1}{2\rho^2} z_2$, therefore,

$$\dot{V}_2 \leq -k_1 z_1^2 + \frac{1}{2}\rho^2 \overline{d}^2 + z_2\left(\overline{f}(x) + g(x)u(t)\right) - \frac{b_m}{r}\tilde{\theta}\dot{\hat{\theta}} \tag{A.3}$$

From equation (6.13), any continuous function $\overline{f}(x)$ defined on a compact set $\Omega_x \subset R^n$ can be written as:

$$\overline{f}(x) = W^T\Phi(x) + \delta(x) \quad \text{where } \|\delta(x)\|^2 \leq \varepsilon^2$$

Thus,

$$z_2\overline{f}(x) = z_2\left(W^T\Phi(x) + \delta(x)\right)$$

$$= z_2 \frac{W^T}{\|W\|}\|W\|\Phi(x) + z_2\delta(x)$$

$$= \frac{W^T}{\|W\|} z_2\|W\|\Phi(x) + z_2\delta(x)$$

Using Lemma 2, then $\quad (\frac{W^T}{\|W\|})(z_2\|W\|\Phi(x)) \leq \frac{1}{2}a^2 + \frac{1}{2a^2} z_2^2\|W\|^2\Phi^T(x)\Phi(x)$

$$z_2\delta(x) \leq \frac{1}{2}b_m z_2^2 + \frac{1}{2b_m}\delta^2 \leq \frac{1}{2}b_m z_2^2 + \frac{1}{2b_m}\varepsilon^2$$

Thus, the following inequality is obtained:

$$z_2\overline{f}(x) \leq \frac{1}{2}a^2 + \frac{1}{2a^2} z_2^2\|W\|^2\Phi^T(x)\Phi(x) + \frac{1}{2}b_m z_2^2 + \frac{1}{2b_m}\varepsilon^2$$

$$= \frac{b_m}{2a^2} z_2^2 \frac{\|W\|^2}{b_m}\Phi^T(x)\Phi(x) + \frac{1}{2}a^2 + \frac{1}{2}b_m z_2^2 + \frac{1}{2b_m}\varepsilon^2$$

$$\leq \frac{b_m}{2a^2} z_2^2 \theta\Phi^T(x)\Phi(x) + \frac{1}{2}a^2 + \frac{1}{2}b_m z_2^2 + \frac{1}{2b_m}\varepsilon^2 \tag{A.4}$$

On the basis of the control law (6.18) $z_2 g(x)u(t)$ can be written as:

$$z_2 g(x) u(t) = z_2 g(x) \left(-\left(k_2 + \frac{1}{2} \right) z_2 - \frac{1}{2a^2} \hat{\theta} z_2 \Phi^T(x) \Phi(x) \right)$$

$$= -g(x) \left(\left(k_2 + \frac{1}{2} \right) z_2^2 + \frac{1}{2a^2} \hat{\theta} z_2^2 \Phi^T(x) \Phi(x) \right)$$

According to the Lemma 1, $\hat{\theta}(t) \geq 0$ for all $t \geq 0$ if the initial condition $\hat{\theta}(0) \geq 0$ has been selected. Thus, the following inequity is obtained due to assumption 1:

$$z_2 g(x) u(t) \leq -b_m \left(\left(k_2 + \frac{1}{2} \right) z_2^2 + \frac{1}{2a^2} \hat{\theta} z_2^2 \Phi^T(x) \Phi(x) \right)$$

$$= -\frac{b_m}{2a^2} \hat{\theta} z_2^2 \Phi^T(x) \Phi(x) - \left(k_2 + \frac{1}{2} \right) b_m z_2^2 \qquad (A.5)$$

Substitution of (A.4) and (A.5) into (A.3) yields

$$\dot{V}_2 \leq -k_1 z_1^2 + \frac{1}{2} \rho^2 \bar{d}^2 + \frac{b_m}{2a^2} \hat{\theta} z_2^2 \Phi^T(x) \Phi(x) + \frac{1}{2} a^2 + \frac{1}{2} b_m z_2^2 + \frac{1}{2b_m} \varepsilon^2 -$$

$$\frac{b_m}{2a^2} \hat{\theta} z_2^2 \Phi^T(x) \Phi(x) - \left(k_2 + \frac{1}{2} \right) b_m z_2^2 \;\; - \frac{b_m}{r} \tilde{\theta} \dot{\hat{\theta}}$$

$$= -k_1 z_1^2 - k_2 b_m z_2^2 + \frac{1}{2} \left(a^2 + \frac{\varepsilon^2}{b_m} + \rho^2 \bar{d}^2 \right) + \frac{b_m}{r} \tilde{\theta} \left(\frac{r}{2a^2} z_2^2 \Phi^T(x) \Phi(x) - \dot{\hat{\theta}} \right)$$

$$= -k_1 z_1^2 - k_2 b_m z_2^2 + \frac{1}{2} \left(a^2 + \frac{\varepsilon^2}{b_m} + \rho^2 \bar{d}^2 \right) +$$

$$\frac{b_m}{r} \tilde{\theta} \left(\frac{r}{2a^2} z_2^2 \Phi^T(x) \Phi(x) - \frac{r}{2a^2} z_2^2 \Phi^T(x) \Phi(x) + \sigma \hat{\theta} \right)$$

$$= -k_1 z_1^2 - k_2 b_m z_2^2 + \frac{1}{2} \left(a^2 + \frac{\varepsilon^2}{b_m} + \rho^2 \bar{d}^2 \right) + \frac{b_m \sigma}{r} \tilde{\theta} \hat{\theta}$$

$$= -k_1 z_1^2 - k_2 b_m z_2^2 + \frac{1}{2} \left(a^2 + \frac{\varepsilon^2}{b_m} + \rho^2 \bar{d}^2 \right) + \frac{b_m \sigma}{r} \tilde{\theta} (\theta - \tilde{\theta})$$

$$= -k_1 z_1^2 - k_2 b_m z_2^2 + \frac{1}{2} \left(a^2 + \frac{\varepsilon^2}{b_m} + \rho^2 \bar{d}^2 \right) + \frac{b_m \sigma}{r} (\tilde{\theta} \theta - \tilde{\theta}^2)$$

$$\leq -k_1 z_1^2 - k_2 b_m z_2^2 + \frac{1}{2} \left(a^2 + \frac{\varepsilon^2}{b_m} + \rho^2 \bar{d}^2 \right) + \frac{b_m \sigma}{r} \left(\frac{1}{2} \tilde{\theta}^2 + \frac{1}{2} \theta^2 - \tilde{\theta}^2 \right)$$

$$= -k_1 z_1^2 - k_2 b_m z_2^2 + \frac{1}{2} \left(a^2 + \frac{\varepsilon^2}{b_m} + \rho^2 \bar{d}^2 \right) + \frac{b_m \sigma}{r} \left(\frac{1}{2} \theta^2 - \frac{1}{2} \tilde{\theta}^2 \right)$$

$$= -k_1 z_1^2 - k_2 b_m z_2^2 - \frac{b_m \sigma}{2r} \tilde{\theta}^2 + \frac{1}{2} \left(a^2 + \frac{\varepsilon^2}{b_m} + \rho^2 \bar{d}^2 + \frac{b_m \sigma}{r} \theta^2 \right)$$

Let $d_0 = \frac{1}{2} \left(a^2 + \frac{\varepsilon^2}{b_m} + \rho^2 \bar{d}^2 + \frac{b_m \sigma}{r} \theta^2 \right)$ and $a_0 = min\,(2k_1, 2k_2 b_m, \sigma)$, thus

$$\dot{V}_2 \leq -a_0 V_2 + d_0 \qquad (A.6)$$

119

For the stability analysis of the closed-loop system, choose the Lyapunov candidate function as:

$$V = V_2 \tag{A.7}$$

From (A.6), the time derivation of (A.7) can be expressed as

$$\dot{V} \le -a_0 V + d_0 \tag{A.8}$$

which implies that for $t \ge 0$,

$$V(t) \le \left(V(0) - \frac{d_0}{a_0} \right) e^{-a_0 t} + \frac{d_0}{a_0}$$

$$\le V(0) e^{-a_0 t} + \frac{d_0}{a_0} \tag{A.9}$$

Thus, $\qquad\qquad \lim_{t \to \infty} V(t) \le \frac{d_0}{a_0}$

From the above expression $V(t)$ is shown to be uniformly bounded, which implies that z_1, z_2 and $\tilde{\theta}$ are bounded. Thus, the state variables x_1, x_2, and parameter estimator $\hat{\theta}$ are also bounded. As a consequence the boundedness of the control $u(t)$ is obtained.

From inequality (A.8),

$$\dot{V} \le -a_0 \left(\frac{1}{2} z_1^2 + \frac{1}{2} z_2^2 + \frac{b_m}{2r} \tilde{\theta}^2 \right) + \frac{1}{2} \left(a^2 + \frac{\varepsilon^2}{b_m} + \rho^2 \bar{d}^2 + \frac{b_m \sigma}{r} \theta^2 \right)$$

$$\le -a_0 k_1 z_1^2 + \frac{1}{2} \left(a^2 + \frac{\varepsilon^2}{b_m} + \rho^2 \bar{d}^2 + \frac{b_m \sigma}{r} \theta^2 \right) \tag{A.10}$$

Rearrangement the inequality (A.10) yields,

$$z_1^2 \le -\frac{\dot{V}}{a_0 k_1} + \frac{1}{2a_0 k_1} \left(a^2 + \frac{\varepsilon^2}{b_m} + \rho^2 \bar{d}^2 + \frac{b_m \sigma}{r} \theta^2 \right)$$

Integrating at both sides of the preceding inequality, and dividing by T gives

$$\frac{1}{T} \int_{t_0}^{t_0+T} z_1^2 \, dt \le -\frac{1}{a_0 k_1} \left[\frac{V(t_0+T)-V(t_0)}{T} \right] + \frac{1}{2a_0 k_1} \left(a^2 + \frac{\varepsilon^2}{b_m} + \rho^2 \bar{d}^2 + \frac{b_m \sigma}{r} \theta^2 \right) \tag{A.11}$$

Since V is uniformly bounded, then $\lim_{T \to \infty} \left[\frac{V(t_0+T)-V(t_0)}{T} \right] = 0$, hence taking limits at both sides yields

$$\lim_{T\to\infty} \frac{1}{T}\int_{t_0}^{t_0+T} z_1^2\, dt \le \frac{1}{2a_0 k_1}\left(a^2 + \frac{\varepsilon^2}{b_m} + \rho^2 \bar{d}^{-2} + \frac{b_m \sigma}{r}\theta^2\right)$$

Because ρ is any real nonzero number, select ρ such that $\rho^2 \ll 1$, then $\rho^2 \bar{d}^{-2} \approx 0$.

Thus,
$$\lim_{T\to\infty} \frac{1}{T}\int_{t_0}^{t_0+T} z_1^2\, dt \le \frac{1}{2a_0 k_1}\left(a^2 + \frac{\varepsilon^2}{b_m} + \frac{b_m \sigma}{r}\theta^2\right)$$

which ends the proof of statement (a) [47].

Substitution of $t_0 = 0$ into (A.11) yields

$$\frac{1}{T}\int_0^T z_1^2\, dt \le -\frac{1}{a_0 k_1}\left[\frac{V(T)-V(0)}{T}\right] + \frac{1}{2a_0 k_1}\left(a^2 + \frac{\varepsilon^2}{b_m} + \rho^2 \bar{d}^{-2} + \frac{b_m \sigma}{r}\theta^2\right)$$

$$\le \frac{1}{a_0 k_1 T}|V(T) - V(0)| + \frac{1}{2a_0 k_1}\left(a^2 + \frac{\varepsilon^2}{b_m} + \rho^2 \bar{d}^{-2} + \frac{b_m \sigma}{r}\theta^2\right) \tag{A.12}$$

Substitution of (A.9) into (A.12) yields

$$\frac{1}{T}\int_0^T z_1^2\, dt \le \frac{1}{a_0 k_1 T}\left|V(0)e^{-a_0 t} + \frac{d_0}{a_0} - V(0)\right| + \frac{1}{2a_0 k_1}\left(a^2 + \frac{\varepsilon^2}{b_m} + \rho^2 \bar{d}^{-2} + \frac{b_m \sigma}{r}\theta^2\right)$$

$$\le \frac{1}{a_0 k_1 T}\left|(1 - e^{-a_0 t})V(0)\right| + \frac{d_0}{a_0^2 k_1 T} + \frac{1}{2a_0 k_1}\left(a^2 + \frac{\varepsilon^2}{b_m} + \rho^2 \bar{d}^{-2} + \frac{b_m \sigma}{r}\theta^2\right)$$

Since $0 \le (1 - e^{-a_0 t})/T \le a_0$ [47],

$$\frac{1}{T}\int_0^T z_1^2\, dt \le \frac{1}{k_1}|V(0)| + \frac{d_0}{a_0^2 k_1 T} + \frac{1}{2a_0 k_1}\left(a^2 + \frac{\varepsilon^2}{b_m} + \rho^2 \bar{d}^{-2} + \frac{b_m \sigma}{r}\theta^2\right) \tag{A.13}$$

From (A.2) and (A.7),

$$V = \frac{1}{2}z_1^2 + \frac{1}{2}z_2^2 + \frac{b_m}{2r}\tilde{\theta}^2 \tag{A.14}$$

By appropriately initializing the reference trajectory $y_r(0)$ using a similar method in [71, 72], yields $z_1(0) = 0$ and $z_2(0) = 0$. Thus,

$$V(0) = \frac{b_m}{2r}\tilde{\theta}(0)^2$$

As, $\tilde{\theta} = \theta - \hat{\theta}$ and $\hat{\theta}(0) = 0$,

$$V(0) = \frac{b_m}{2r}\theta(0)^2 \tag{A.15}$$

Substitution (A.15) into (A.13) yields

$$\frac{1}{T}\int_0^T z_1^2 \, dt \leq \frac{b_m}{2k_1 r}\theta(0)^2 + \frac{d_0}{a_0{}^2 k_1 T} + \frac{1}{2a_0 k_1}\left(a^2 + \frac{\varepsilon^2}{b_m} + \rho^2 \bar{d}^2 + \frac{b_m \sigma}{r}\theta^2\right)$$

which ends the proof of statement (b) [47,72].